SOUND ABSORPTION BASED ON ACOUSTIC METASURFACES

SIBO HUANG

PhD

The Hong Kong Polytechnic University

This programme is jointly offered by The Hong Kong Polytechnic University and Tongji University

2022

The Hong Kong Polytechnic University

Department of Mechanical Engineering

Tongji University

School of Physics Science and Engineering

Sound Absorption Based on Acoustic Metasurfaces

Sibo Huang

A thesis submitted in partial fulfilment of the requirements

for the degree of Doctor of Philosophy

January 2022

CERTIFICATE OF ORIGINALITY

I hereby declare that this thesis is my own work and that, to the best of my knowledge and belief, it reproduces no material previously published or written, nor material that has been accepted for the award of any other degree or diploma, except where due acknowledgement has been made in the text.

____(Signed)

____________Sibo HUANG_______________(Name of student)

ABSTRACT

High-efficiency and broadband sound absorption based on ultra-thin structures is of great interest in physics and remarkable application values in engineering communities, but it remains challenging for conventional sound absorbers. Conventional sound absorbers including porous/fibre materials and perforated-panel absorbers, generally require thick structures whose sizes are on the same order of magnitude with their longest working acoustic wavelengths, which inevitably brings a barrier in settling low-frequency noise for practical applications with restricted space.

Since the 2010s, acoustic metasurfaces, which exhibit unprecedented acoustic properties by modulating their sub-wavelength geometries, have shown fascinating abilities to manipulate acoustic waves. This thesis aims to realize highly efficient and ultra-thin sound absorbers based on acoustic metasurfaces taking advantage of their compact structures and superb capacity of wave modulation. Starting by pursuing perfect narrow-band sound absorption with deep subwavelength thickness, this thesis firstly investigates a structure composed of a curled channel and an embedded neck, where the former element supports a large phase delay within a thin structure and the latter element provides outstanding adjustability of the structure. Subsequently, to further improve the adjustability, the effect of the embedded neck is strengthened by extending the length and the curled channel is changed to a straight cavity for reducing the complexity of the structure. However, limited by the dispersive nature of resonances, the above designs generally feature narrow-band working performances, leading to a major obstacle in the implementations suffering from broadband noise.

To solve broadband noise, this thesis further focuses on investigating high-efficiency broadband sound absorbers based on coupled acoustic metasurfaces. In the

field of metasurface-based broadband absorbers, one commonly-used and straightforward technique employed in previous studies is to arrange multiple narrow-band units with quasi-perfect or perfect sound absorption and to assemble a wide sound-absorbing band. In contrast, this thesis presents a counter-intuitive but more efficient concept of design that is based on a series of coherently coupled “imperfect components”. Although the individual imperfect components can only realize inferior sound absorption performance, by suitably tuning the coherent coupling among them, a broadband high-efficiency absorption can be achieved thanks to their mutual interactions. Subsequently, the general acoustic responses of sound-absorbing materials are investigated, which reveals two guidelines, the over-damped condition and the reduced excessive response, for constructing broadband sound absorbers approaching the optimal thickness restricted by the causality constraint. Following the two guidelines, a coupled sound-absorbing metasurface is presented and successfully approaches the minimal thickness.

Furthermore, inspired by the design concepts and the impedance-modulation techniques presented in constructing the metasurface-based sound absorbers above, this thesis investigates acoustic devices related to noise control engineering and impedance engineering, including the devices capable of sound attenuation in flow ducts, asymmetric absorption, extreme sound confinement/absorption, and strong emission enhancement of sound sources.

PUBLICATIONS ARISING FROM THE THESIS

Journal papers as the first or the co-first (*) author

1. **S. Huang**, S. Li, X. Wang, D. Mao, Micro-perforated absorbers with incompletely partitioned cavities, Applied Acoustics, 126 (2017) 114-119.
2. **S. Huang***, X. Fang,* X. Wang, B. Assouar, Q. Cheng, Y. Li, Acoustic perfect absorbers via spiral metasurfaces with embedded apertures, Applied Physics Letters, 113 (2018) 233501.
3. **S. Huang**, X. Fang, X. Wang, B. Assouar, Q. Cheng, Y. Li, Acoustic perfect absorbers via Helmholtz resonators with embedded apertures, The Journal of the Acoustical Society of America, 145 (2019) 254-262.
4. **S. Huang***, Z. Zhou*, D. Li, T. Liu, X. Wang, J. Zhu, Y. Li, Compact broadband acoustic sink with coherently coupled weak resonances, Science Bulletin, 65 (2020) 373-379.
5. **S. Huang*,** T. Liu*, Z. Zhou, X. Wang, J. Zhu, Y. Li, Extreme Sound confinement from quasibound states in the continuum, Physical Review Applied, 14 (2020) 021001.
6. **S. Huang***, E. Zhou*, Z. Huang, P. Lei, Z. Zhou, Y. Li, Broadband sound attenuation by metaliner under grazing flow, Applied Physics Letters, 118 (2021) 063504.
7. Z. Zhou*, **S. Huang***, D. Li, J. Zhu, Y. Li, Broadband impedance modulation via non-local acoustic metamaterials, National Science Review, nwab171(2021)
8. L. Huang*, Y.K. Chiang*, **S. Huang***, C. Shen*, F. Deng, Y. Cheng, B. Jia, Y. Li, D.A. Powell, A.E. Miroshnichenko, Sound trapping in an open resonator, Nature Communications, 12 (2021) 4819.

9. D. Li*, **S. Huang***, Y. Cheng, Y. Li, Compact asymmetric sound absorber at the exceptional point, Science China-Physics Mechanics & Astronomy, 64 (2021) 244303.

10. D. Kong*, **S. Huang***, D. Li, C. Cai, Z. Zhou, B. Liu, G. Cao, X. Chen, Y. Li, S. Liu, Low-frequency multi-order acoustic absorber based on spiral metasurface, The Journal of the Acoustical Society of America, 150 (2021) 12-18.

Journal papers as the contributing author

1. D. Li, **S. Huang**, F. Mo, X. Wang, Y. Li, Low-frequency broadband absorbers based on coupling micro-perforated panel and space-curling chamber, Chinese Science Bulletin-Chinese, 65 (2020) 1420-1427.

2. S. Xie, X. Fang, P. Li, **S. Huang**, Y. Peng, Y. Shen, Y. Li, X. Zhu, Tunable Double-Band Perfect Absorbers via Acoustic Metasurfaces with Nesting Helical Tracks, Chinese Physics Letters, 37 (2020) 054301.

ACKNOWLEDGEMENTS

I would like to express my sincere gratitude to my chief supervisor Prof. Zhongqing Su for his trust, support, and help for my Ph.D. study and research. And I would also like to thank my previous chief supervisor Prof. Jie Zhu for providing me this wonderful opportunity to study at PolyU and his encouragement and help for my study and research. With the invaluable guidance and continuous care of Prof. Zhongqing Su and Prof. Jie Zhu, I experienced an extremely fruitful and enjoyable journey during the one and a half years of study at PolyU. Meanwhile, my deep appreciation is dedicated to Prof. Yong Li, my supervisor at Tongji University, for his kind encouragement and insightful suggestions for my research. I really feel fortunate to be a student of such caring, patient, and knowledgeable supervisors.

I wish to thank Dr. Tuo Liu for his in-depth suggestions on my research and the great help in the preparation of my articles. I really learned a lot of theoretical knowledge and research skills from the frequent discussions with Dr. Tuo Liu. I would also like to thank the guidance and help from Dr. Xu Wang, Prof. Dongxin Mao, Dr. Yabin Jin, Prof. Tong Hao at Tongji University. They taught me many valuable suggestions on my research. I am grateful for the insightful suggestions from Prof. Shuang Zhang at Hong Kong University, which helps to improve considerably the quality of my research. I appreciate the fruitful discussions with Dr. Lujun Huang from UNSW and many valuable suggestions from him.

I want to thank all the members from Prof. Zhu's group, Dr. Zhongming Gu, Dr. Shanjun Liang Dr. He Gao, Dr. Yafeng Chen, Mr. Shuowei An, Ms. Haiyan Fan, Mr.

Yi Zheng, Mr. Lei Fan and Ms. Jiamin Guo for the help they offered and the enjoyable time we had together.

I also want to thank all the members from Prof. Li’s group, Mr. Xinsheng Fang, Mr. Shuhuan Xie, Mr. Dongting Li, Mr. Zhilin Zhou, Ms. Yi Chen, Ms. Panpan Chen, Ms. Hua Ding, Ms. Junmei Cao, Mr. Nengyin Wang, Mr. Bin Jia, Ms. Chengcheng Zhou, Mr. Hongyu Ma, Mr. Pei Qian and Ms. Shanshan Liu for their help on research and pleasant time we shared.

Last but not least, I would like to thank my parents and family members for their selfless support and encouragement throughout my study. Special thanks to my beloved girlfriend Qingyao, for bringing me so much joy and taking care of my cat, little Paper, during the three months of quarantine life. Being with you reminds me of a word from Tagore's Stray Bird: “*You smiled and talked to me of nothing and I felt that for this I had been waiting long.*”.

TABLE OF CONTENTS

LIST OF FIGURES

1. Chapter 1: Introduction

1.1 Conventional materials and structures for sound absorption

Sound absorbers present an effective approach to adjust acoustic environments and therefore find extensive applications in noise control engineering and impedance engineering [1]. Conventional sound absorbers, such as traditional porous materials, can handle noise in medium to high frequencies effectively. However, they generally demand structural thicknesses on the same order of magnitude with their longest working acoustic wavelengths for high-efficiency performance [2, 3], which leads to bulky structures when dealing with low-frequency acoustic waves and consequently hinders the practical implementations with restricted space [Fig. 1.1]. Using resonant structures can enhance the absorption performance within a certain frequency band at relatively low frequencies. Among conventional resonant sound absorbers, micro-perforated panel (MPP) absorbers are one the most efficient as well as typical designs [4, 5], which can remarkably balance the low-frequency and broadband absorption performances. However, in many practical applications suffering from significantly low-frequency and especially broadband noise, there is considerable improvement demanded in their thickness and working frequency bandwidths.

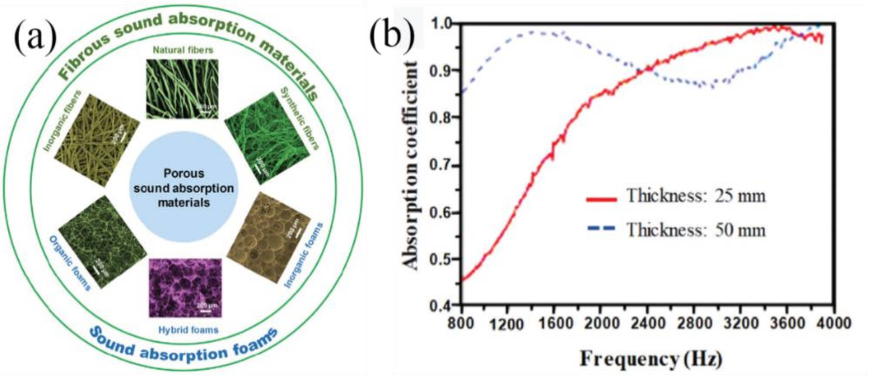

Figure 1.1 Conventional porous materials. (a) Porous materials for sound absorption. (b) Absorption curves of a porous material with different thicknesses (reprinted from [3]).

Since the 1990s, there have been numerous studies focusing on how to enhance the sound-absorbing performances of MPP absorbers at low frequencies, where solutions are provided by using irregular-shaped cavities [6] (see Fig. 1.2), employing honeycomb structures [7], completely partitioning the air cavities with subwavelength intervals [8], and incompletely partitioning the backed cavities [9] (see Fig. 1.3), etc. However, these conventional strategies generally can only enhance the absorption performance of the MPP absorbers in the low frequency ranges to a relatively limited extent, and the thickness of these structures encounters difficulty to reach a deep subwavelength level (such as less than 1/20th of the wavelength of acoustic waves). To reduce the thickness and to enhance the absorption performances of sound absorbers, this thesis will utilize the advantages of acoustic metasurfaces to construct deep subwavelength and broadband sound absorbers.

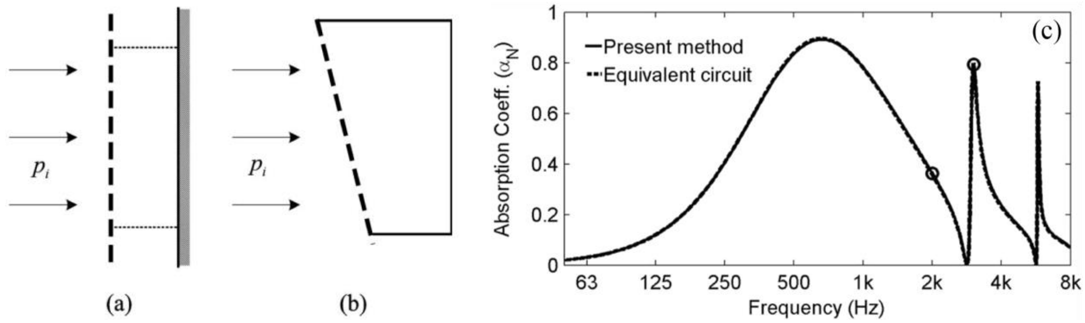

Figure 1.2 Schematics of MPP absorbers with regular (a) and irregular-shaped (b) cavities. (c) Absorption curve of the MPP absorber having an irregular-shaped cavity (reprinted from [6]).

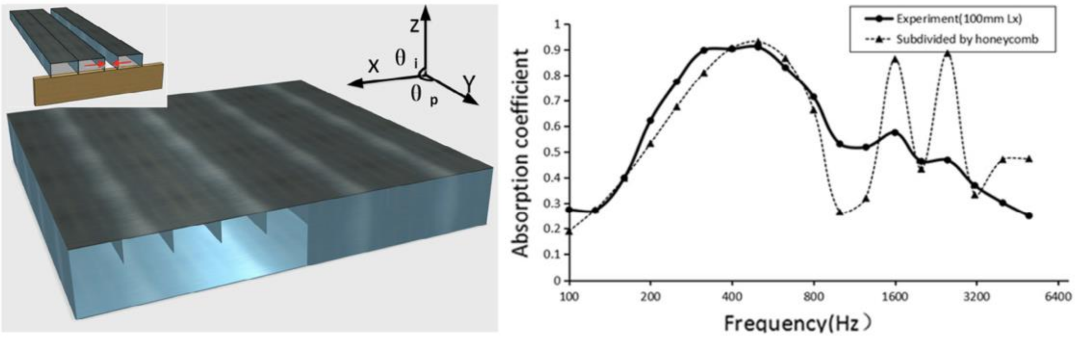

Figure 1.3 Schematic of MPP absorbers with incompletely partitioned cavities (reprinted from [9]）.

1.2 Acoustic metasurfaces

Since the 2010s, acoustic metasurfaces, which can provide significant local phase or amplitude modulations or efficient sound absorption via adjusting their sub-wavelength structures, have demonstrated their powerful capabilities of sound-wave manipulations [10, 11]. To name some, acoustic metasurfaces have demonstrated deep sub-wavelength focusing [12, 13], negative refraction [14-16], efficient wavefront modulation [17, 18] and asymmetric sound transmission/reflection [19-24] theoretically and experimentally. Regarding the field of sound absorption, the feature of compact structures enables acoustic metasurfaces to be desired candidates for realizing ultra-thin sound absorbers [25], where the metasurface-based acoustic absorbers are also called absorbing acoustic metasurfaces [26-29].

Although metasurface-based sound absorbers exhibit ultra-thin thickness, which leaves many possibilities to pursue further improvement. For instance, tunable perfect absorption and broadband sound absorption with ultrathin structures have been still remaining challenging.

1.3 Organization of the thesis

In this thesis, the existing problems and challenges of the conventional sound absorbers and the absorbing acoustic metasurfaces motivated this research. Specifically, the main goal of this thesis is to achieve high-efficiency broadband absorption based on compact acoustic metasurfaces.

This thesis contains five chapters: The first chapter (the present chapter) is the introduction of the conventional sound absorbers and acoustic metasurfaces; The fifth chapter demonstrates the conclusions and the future work; The three main chapters (Chapters 2-4) demonstrate how this thesis presents research from tunable narrow-band sound absorbers to broadband absorbers and further to the inspired high-performance acoustic devices. The organization of Chapters 2-4 is as follows:

Chapter 2 firstly investigates theoretically and validates experimentally the narrowband perfect absorption in a low-frequency range based on spiral metasurfaces. Subsequently, an embedded neck is introduced to enhance the adjustability of the spiral metasurfaces. Finally, by presenting a further improved design, neck embedded Helmholtz resonators (NEHRs), this thesis realizes highly tunable perfect absorption with a constant shape, which paves a way for developing broadband absorbers with multiple coupled units.

Chapter 3 firstly investigates the physical mechanism of nonlocal coupling among ultrathin imperfect components and establishes a systematic model for theoretically designing coupled sound-absorbing metasurfaces. Subsequently, this thesis demonstrates that a structure composed of multiple neck-embedded Helmholtz resonators (NEHRs) exhibiting imperfect sound absorption can quasi-perfectly absorb broadband sound waves. Although the individual imperfect NEHR manifests insufficient absorption, by adjusting the coherent nonlocal coupling among the NEHRs, their collective effect achieves considerably enhanced sound absorption within a wide frequency band via a remarkably reduced thickness. Finally, to demonstrate the design concept, three coupled metasurfaces are presented based on a series of imperfect units. The first design exhibits an averaged absorption coefficient of 0.95 from 297 to 475 Hz with a structure of 5 cm in thickness, and the second design offers an averaged absorption of 0.957 from 870 Hz to 3224 Hz based on a metasurface of 3.9 cm. For the last design, broadband quasi-perfect absorption is achieved with structure of 100 mm thick that approaches the causality-governed minimal thickness, manifesting an averaged sound absorption coefficient of 0.93 within the range of 320-6400 Hz.

Chapter 4 further investigates several acoustic devices capable of broadband sound attenuation, asymmetric absorption, extreme sound confinement, and strong emission enhancement of sound sources. These high-performance acoustic devices are inspired by the concepts and techniques of absorbing acoustic metasurfaces investigated in Chapters 2-3, which would extend the impact and enhance the significance of the metasurface-based sound absorbers.

2. Chapter 2: Perfect Sound Absorption Based on Acoustic Metasurfaces

2.1 Background of acoustic metasurface-based perfect absorbers

Acoustic metasurfaces usually consist of resonant units featuring highly enhanced local energy intensity inside, which have proved to be outstanding candidates for high absorption efficiency [28, 29]. In the previous studies of metasurface-based sound absorbers, one effective design achieving perfect absorption and deep subwavelength thickness is to utilize a decorated membrane [26, 27] (see Fig. 2.1). Nevertheless, this design demands uniform and strictly tuned tensions of the membranes, resulting in possible fabrication challenges as well as durability issues in engineering implementations.

Introducing coiling-up space with labyrinthine configuration [28-35] is another efficient and feasible approach. Since acoustic waves are scalar waves, the effective propagating path of acoustic waves can be greatly elongated within a comparably short distance in coiling-up space and therefore highly efficient acoustic absorption can be achieved with an ultrathin thickness.

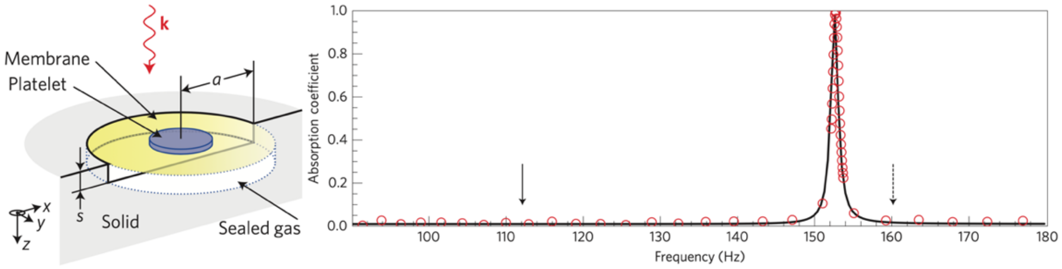

Figure 2.1 Schematic of membrane-based acoustic absorbers (left). The absorption curve (reprinted from [27]).

In previous studies, ultra-thin and high-efficiency absorbers composed of coiled channels were theoretically proposed and experimentally verified [28-30] (see Figs. 2.2-2.3). In these designs, the resonance is majorly determined by the phase delay (reactance) inside the structure, and hence these designs strictly require a quarter wavelength of channel for total absorption (shown later). However, for labyrinthine structures, the tuning of the channel's length is not very efficient, which hinders the realization of tunable acoustic absorbers. Besides, it can be noticed that the curled-channel metasurfaces generally have a narrow working frequency band. As will be demonstrated in Chapter 3, to construct a broadband absorber, an effective technique to couple multiple component metasurfaces, and basically a component with superior tunability in acoustic properties can lead to a more efficient broadband sound absorber. Therefore, this thesis firstly focuses on how to achieve highly tunable sound absorption based on acoustic metasurfaces.

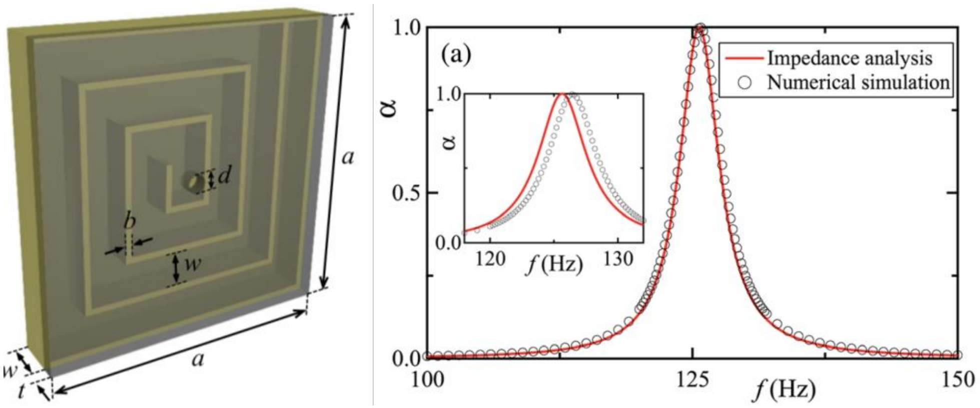

Figure 2.2 An acoustic absorber with a coiling-up channel and its absorption curve (reprinted from [28]).

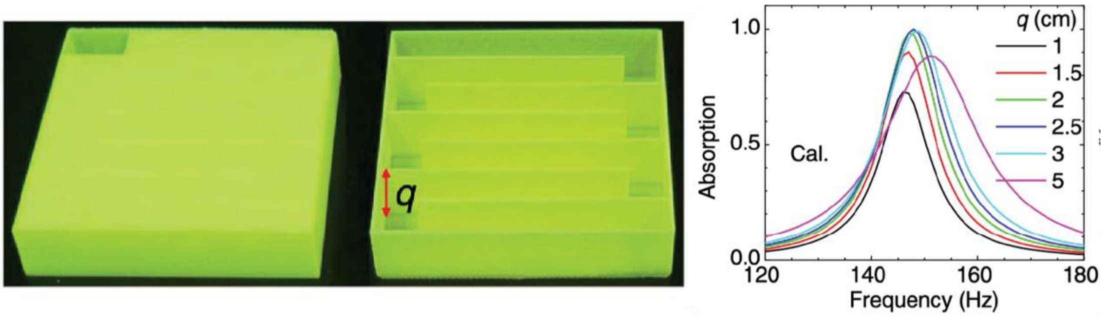

Figure 2.3 An acoustic absorber with another coiling-up channel and its absorption curves with variation of thickness (reprinted from [30]).

2.2 Tunable perfect sound absorption based on spiral metasurfaces

Acoustic absorption is usually realized by the dissipation of sound energy from thermal and viscous losses within sound-absorbing materials and structures. To evaluate the sound-absorbing capability of a sound absorber, it is widely employed as well as highly feasible to calculate the absorption coefficient (α) based on the normal surface impedance of the absorber under normal incidence, Z, since there is a direct connection between the surface impedance (Z) and α, which reads,

$$\alpha = 1 - \left| \frac{Z - \rho_0 c_0}{Z + \rho_0 c_0} \right|^2 , \qquad \textbf{(2.1)}$$

where ρ_0 and c_0 represent the static air density and the air sound speed, respectively. Equation (2.1) shows that a total absorption strictly demands "impedance matching condition" of air and the sound absorber, i.e., $\mathrm{Re}(Z) = \rho_0 c_0$ and $\mathrm{Im}(Z) = 0$. For sound-absorbing structures, the acoustic resistance, $\mathrm{Re}(Z)$, is relevant to the thermal-viscous losses near the air-structure interfaces. To describe the effect of thermal-viscous losses and calculate the acoustic resistance, the "narrow region acoustics" theory can be applied [36, 37].

In the conditions of $\lambda \gg d_{\mathrm{v}}, d_{\mathrm{h}}$ and $\lambda \gg H$, the propagation of acoustic waves in rectangular and cylindrical tunnels can be theoretically analyzed with considering the thermal-viscous losses. Here, λ is the wavelength and $d_{\mathrm{v}} = \sqrt{2\eta/(\rho_0 \omega)}$, $d_{\mathrm{h}} = 2K/(\rho_0 \omega C_{\mathrm{p}})$ represent the thicknesses of the thermal boundary layer and the viscous boundary layer, H represent the hydraulic diameter of the cross-section of the tunnels, ω is the angular frequency, η indicate the dynamic viscosity of air, C_{p} indicate the heat capacity at constant pressure, and K indicate the fluid thermal conductivity. According to previous studies [36, 37], the k_{v} and k_{h} can be introduced as the viscous and the thermal wave numbers, which reads

$$k_{\mathrm{v}}^{\ 2} = -\mathrm{j}\omega\frac{\rho_0}{\eta}, \tag{2.2}$$

$$k_{\mathrm{h}}^{\ 2} = -\mathrm{j}\omega\frac{\rho_0 C_{\mathrm{p}}}{K}. \tag{2.3}$$

Then, for a cylinder aperture or neck with a diameter of d_{a}, the impact of viscous and thermal fields read

$$\Psi_{\mathrm{va}} = -\frac{J_2(k_{\mathrm{v}}d_{\mathrm{a}}\ /\ 2)}{J_0(k_{\mathrm{v}}d_{\mathrm{a}}\ /\ 2)}, \tag{2.4}$$

$$\Psi_{\mathrm{ha}} = -\frac{J_2(k_{\mathrm{h}}d_{\mathrm{a}}\ /\ 2)}{J_0(k_{\mathrm{h}}d_{\mathrm{a}}\ /\ 2)}, \tag{2.5}$$

where J_n is the Bessel function. It is noted for the published paper [38], Eqs. (2.4)-(2.5) omitted a negative sign “-“. And for a rectangular tube with side lengths of w and h, the function of viscous and thermal fields read

$$\Psi_{\mathrm{vc}} = k_{\mathrm{v}}^2\sum_{m=0}^{\infty}\left[\begin{array}{l}\left(\alpha_{m\mathrm{v}}m'\right)^{-2}\left(1-\dfrac{\tan\left(\alpha_{m\mathrm{v}}w\ /\ 2\right)}{\alpha_{m\mathrm{v}}w\ /\ 2}\right)\\ +\left(\beta_{m\mathrm{v}}m'\right)^{-2}\left(1-\dfrac{\tan\left(\beta_{m\mathrm{v}}h\ /\ 2\right)}{\beta_{m\mathrm{v}}h\ /\ 2}\right)\end{array}\right], \tag{2.6}$$

$$\Psi_{\mathrm{hc}} = k_{\mathrm{h}}^2\sum_{m=0}^{\infty}\left[\begin{array}{l}\left(\alpha_{m\mathrm{h}}m'\right)^{-2}\left(1-\dfrac{\tan\left(\alpha_{m\mathrm{h}}w\ /\ 2\right)}{\alpha_{m\mathrm{h}}w\ /\ 2}\right)\\ +\left(\beta_{m\mathrm{h}}m'\right)^{-2}\left(1-\dfrac{\tan\left(\beta_{m\mathrm{h}}h\ /\ 2\right)}{\beta_{m\mathrm{h}}h\ /\ 2}\right)\end{array}\right], \tag{2.7}$$

where $m' = (m + 1/2)\pi$, $\alpha_{m\mathrm{v}} = \sqrt{k_{\mathrm{v}}^2 - (2m'/w)^2}$, $\beta_{m\mathrm{v}} = \sqrt{k_{\mathrm{v}}^2 - (2m'/h)^2}$, $\alpha_{m\mathrm{h}} = \sqrt{k_{\mathrm{h}}^2 - (2m'/w)^2}$, $\beta_{m\mathrm{h}} = \sqrt{k_h^2 - (2m'/h)^2}$. It is noted for the published paper [38], $\alpha_{m\mathrm{v}}$, $\beta_{m\mathrm{v}}$, $\alpha_{m\mathrm{h}}$, $\beta_{m\mathrm{h}}$ have typos missing the square symbols. Equations (2.6)-(2.7) can achieve good accuracy by calculating the first 100 terms ($m = 0, 1, 2, \ldots, 100$). Based on the results above, the complex wave number and the complex air density reads

$$k_{\mathrm{ca(c)}}^2 = k_0^2\left(\frac{\gamma-(\gamma-1)\Psi_{\mathrm{ha(c)}}}{\Psi_{\mathrm{va(c)}}}\right), \tag{2.8}$$

$$\rho_{\mathrm{ca(c)}} = \frac{\rho_0}{\Psi_{\mathrm{va(c)}}}, \tag{2.9}$$

where γ is the ratio of specific heats of air. In this thesis, it is set that $\eta = 1.81 \times 10^{-5}$, $C_{\mathrm{p}} = 1005$, $K = 0.026$, and $\gamma = 1.4$, referring to the experimental environment. With the analysis of thermal-viscous effect in sound-absorbing structures above, the surface acoustic impedance of a straight or curled channel (Z_{curl}) reads

$$Z_{\mathrm{curl}} = -\mathrm{j}\rho_{\mathrm{curl}} c_{\mathrm{curl}} \cot(k_{\mathrm{curl}} L) A \,/\, s_0, \tag{2.10}$$

where ρ_{curl}, c_{curl}, and k_{curl} represent the effective air density, sound speed and wave number inside the curled cavity considering the thermal-viscous losses. $A = \pi a^2$ is the front surface area of the overall structure, and $s_0 = w \times h$ denotes the cross-section of the curled cavity [Fig. 2.4]. From Eq. (2.10), it can be noticed that the impedance matching requires that $k_{\mathrm{curl}} L$ must be at least close to $\pi/2$, which demands the curled cavity to have a length (L) at least approaching a quarter wavelength of the sound wave totally absorbed. As discussed in the former section, this requirement will hinder the adjustability of the curled-space metasurfaces in practical applications.

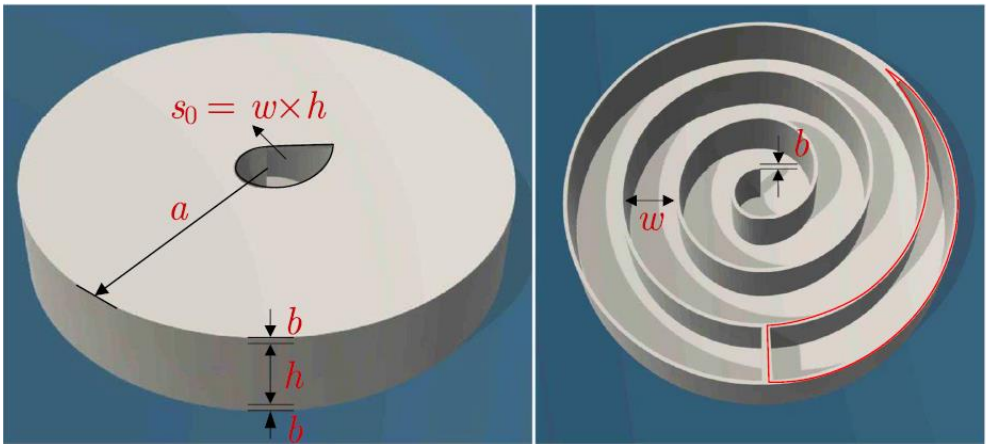

Figure 2.4 Schematic illustration of an acoustic absorber with a spirally curled channel (reprinted from [30]).

To pursue superior adjustability of absorption performance, firstly, an embedded neck is introduced to a spiral metasurface by appending the embedded neck to the front opening of the curled cavity [Fig. 2.5]. Consequently, the overall impedance of the curled metasurface having an embedded neck is the summation of the curled channel's and the neck's (Z_a) acoustic impedance, i.e., $Z = Z_{curl} + Z_a$. As long as Z_a can be largely modulated, the whole metasurface will become highly tunable, which is the main motivation for presenting the concept of embedded necks.

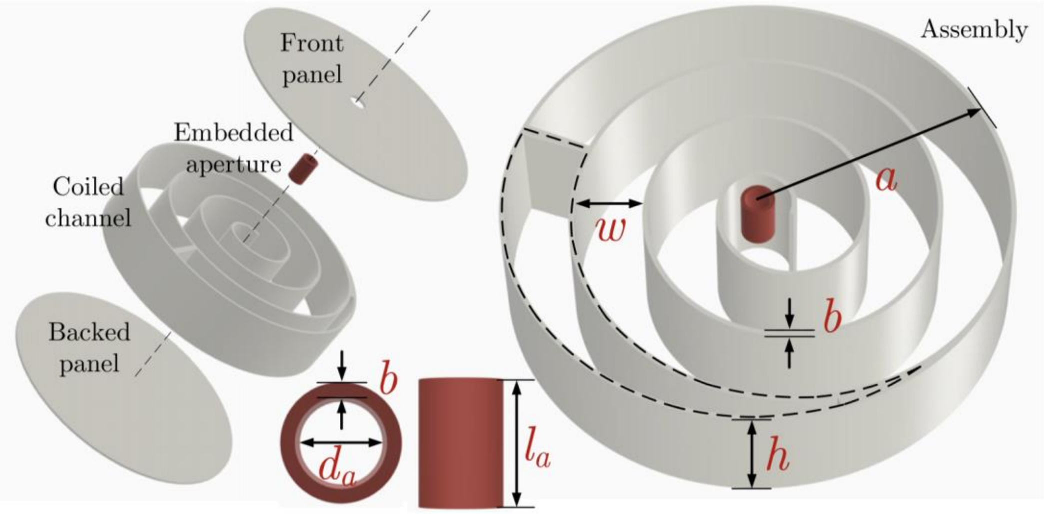

Figure 2.5 A spiral metasurface consisting of a curled cavity and an embedded neck [38].

For an aperture or neck, from Crandall's theory [39], the acoustic impedance of an infinite long aperture/neck/tube for a unit length is expressed as

$$Z_{\mathrm{a}0} = -\mathrm{j}\rho_0 \omega J_0(\kappa d_{\mathrm{a}} / 2) / J_2(\kappa d_{\mathrm{a}} / 2), \tag{2.11}$$

where $\kappa^2 = -\mathrm{j}\rho_0\omega/\eta$. However, in this formula, the thermal losses are neglected, which is suitable for a relatively short neck but will have deviations for a long and embedded neck. Therefore, the acoustic impedance of a relatively long neck is analyzed here. As illustrated in Fig. 2.6, the acoustic pressure is $p(z) = pe^{-\mathrm{j}k_{\mathrm{ca}}z}$ and the velocity is $v(z) = ve^{-\mathrm{j}k_{\mathrm{ca}}z}$ along the z-axis. By treating the neck as a lumped acoustic element, the acoustic impedance of the neck reads $Z_{\mathrm{a}0} = [p(z + l_{\mathrm{a}}) - p(z)] / v_z(z + l_{\mathrm{a}} / 2) = 2\mathrm{j}Z_{\mathrm{c}} \sin(k_{\mathrm{c}} l_{\mathrm{a}} / 2)$, where $Z_{\mathrm{c}} = \rho_{\mathrm{c}} c_{\mathrm{c}}$ is the effective characteristic air acoustic impedance inside the neck. By connecting Eqs. (2.8)-(2.9), the acoustic impedance of a neck, involving both the effects of the viscous and thermal losses, are expressed as (Note that in the paper [40], Eq. (2.12) has a typo with a needless negative sign "-".)

$$Z_{\mathrm{a}} = \frac{A}{S_{\mathrm{a}}}\left[\rho_0 c_0 \frac{2\mathrm{j}\sin(\frac{k_{\mathrm{ca}} l_{\mathrm{a}}}{2})}{\sqrt{(\gamma-(\gamma-1)\Psi_{\mathrm{ha}})\Psi_{\mathrm{va}}}}\right]. \tag{2.12}$$

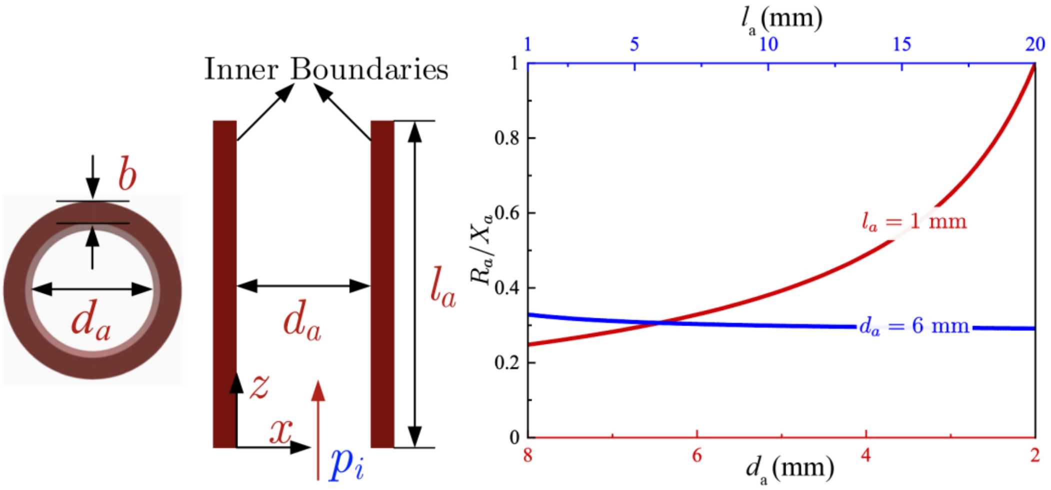

Figure 2.6 Adjustability of a long neck.

Left picture: schematic of a cylinder tube with a diameter d_a and a length l [40]. Right diagram: R_a/X_a of the embedded neck by varying the diameter (red line) and the length (blue line). $d_a = 6$ mm and $l_a = 1$ mm (reprinted from [38]). Note that in reference [38], the top and bottom abscissa labels are wrongly reversed.

In addition, when a neck radiates to outside fields, end correction of the acoustic impedance needs to be taken into consideration. Specifically, when a neck is mounted at an infinitely large panel and radiates into free space, the higher order propagating waves make the effective length of the neck elongated by $\delta_0 = [8/(3\pi)]d_{\mathrm{a}}$ when both the upper and lower sides of end corrections are considered [39, 41]. However, when one side of a neck radiates into a small cavity and the other side radiates into a relatively large space (considered approximating free space), such as the circumstance in this thesis, a further end correction should be made, which reads, $\delta_\Omega = [1 + (1 - 1.25\varepsilon)]\delta_0/2$, $\varepsilon = d_\mathrm{a} / \min(s, w)$. In addition, the friction losses of acoustic waves along the panel near the neck's top and bottom openings bring about the additional part of $2\sqrt{2\rho_0\omega\eta}$ [41]. Consequently, the acoustic impedance of an embedded neck for a neck-embedded metasurface reads

$$Z_\mathrm{a} = \frac{A}{S_\mathrm{a}}\left[\rho_0 c_0 \frac{2\mathrm{j}\sin(\frac{k_\mathrm{ca} l_\mathrm{a}}{2})}{\sqrt{(\gamma - (\gamma - 1)\Psi_\mathrm{ha})\Psi_\mathrm{va}}} + 2\sqrt{2\omega\rho_0\eta} + \mathrm{j}\omega\rho_0\delta_\Omega\right]. \qquad \textbf{(2.13)}$$

Combining Eq. (2.10), the overall surface acoustic impedance of the neck-embedded spiral metasurface is $Z = Z_\mathrm{curl} + Z_\mathrm{a}$.

In the following, this thesis will show how to modulate the embedded neck and the curled channel to realize tunable absorption performances. Figure 2.6 illustrates that the changing of the neck's diameter can efficiently adjust the ratio of the acoustic resistance and reactance. And the changing of neck's length will ideally tune the values of acoustic impedance with only the small influence on the ratio between resistance and reactance. Thus, only if the length of the neck could be largely tuned, one goal with specific values of acoustic resistance and acoustic reactance can be offered by the neck through modulating both the diameter and the length.

Figure 2.7 manifests the "impedance matching diagram" at 137.5 Hz, where the dashed lines represent the matching of acoustic resistance and the solid lines show the matching of reactance. With such a method, the intersections of the solid lines and the dashed lines can identify complete absorption. Based on this diagram, it can be observed that the neck-embedded spiral metasurface can theoretically realize a perfect absorption with a greatly tunable length, rather than a relatively fixed length approaching a quarter wavelength.

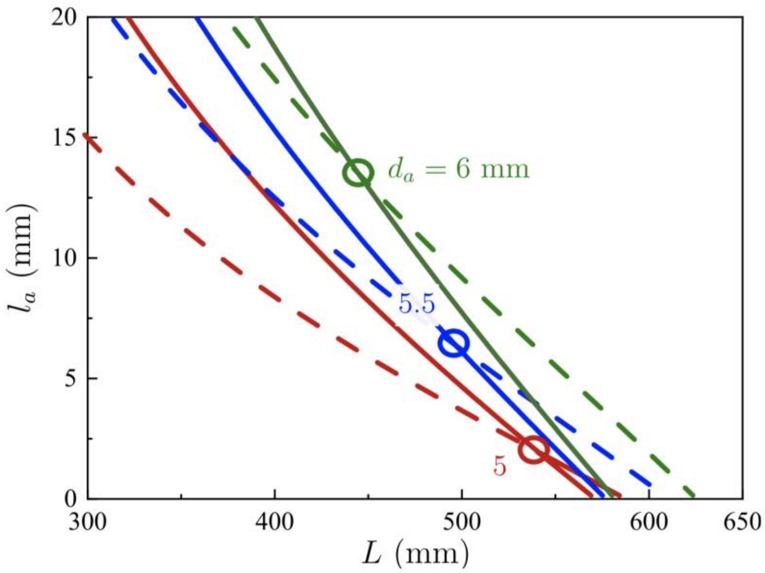

Figure 2.7 Impedance matching diagram.

The dashed lines and the solid lines represent the matching conditions of acoustic resistance and reactance, respectively. The different colors denote the structures with different neck diameters. The analyzed frequency is 137.5 Hz [38].

To verify the theoretical results above, experimental samples are fabricated and tested in an impedance tube. The test samples are produced by the 3D printing based on laser stereolithography (140 μm) using photosensitive resin, presenting precision of 0.1 mm in fabrication. The absorption coefficients are measured employing the impedance tube equipment (according to ASTM C384-04(2011)). Here, the cylinder impedance tube has a diameter of 10 cm.

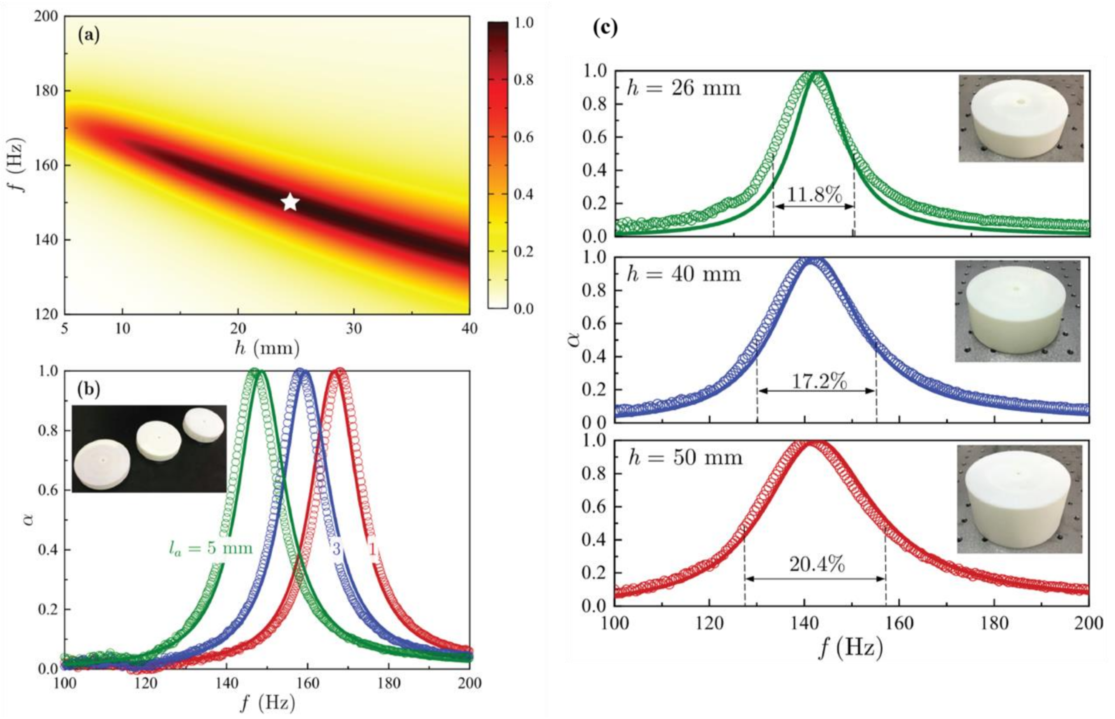

Figure 2.8 Tunable perfect absorption performances with neck-embedded spiral metasurfaces.

(a) The sound absorption diagram as functions of the height of the neck-embedded metasurface and the frequency. The other parameters of the neck-embedded metasurface are L = 470 mm, w =13 mm, l_a = 5 mm, and d_a = 6 mm. (b) The tunable perfect absorption performances with adjustable resonant frequencies. The solid lines and dots represent the theoretically calculated and experimentally measured results, respectively. (c) The tunable perfect absorption performances with adjustable absorption bandwidths. The absorption coefficients of the presented neck-embedded metasurfaces (shown in the inset pictures) with increasingly thicker curled channels. Perfect absorption peaks are at f_r = 141 Hz (in olive), 141.25 Hz (in blue), and 141 Hz (in red) having absorption bandwidths of 11.8%, 17.2%, and 20.4%, respectively. The solid lines and dots represent the theoretically calculated and experimentally measured results, respectively (represented from [38]).

Next, six experimental samples are fabricated and tested, designed by fixing the constant length of a curled channel and just modulating the length and the diameter of an embedded neck and the height of the curled channel. It is manifested that perfect absorption at tunable frequencies and perfection with tunable bandwidths can be realized theoretically and experimentally [Fig. 2.8], which proves that the concept of adding an embedded neck provides significant improvement of adjustability in absorption performances. Figure 2.8(c) shows that for total absorption at a certain frequency, a wider absorption band requires a thicker structure, which provides an important insight into the construction of broadband absorbers.

In summary, this section investigated theoretically and experimentally neck-embedded spiral metasurfaces consisting of curled cavities and embedded necks. The neck-embedded spiral metasurfaces can not only totally absorb acoustic energy at low frequencies via a deep sub-wavelength thickness of around 1/100th of the working wavelength, but also achieve a superior capability of acoustic impedance manipulation and therefore realize tunable absorption performances. However, there are two challenges unsolved. For one thing, the configuration of neck-embedded spiral metasurfaces is still quite complicated, which may give rise to obstructions in practical applications. For another thing, despite the improved adjustability in acoustic impedance, the tunable absorption performances are achieved, more or less, by changing the shapes of the whole metasurfaces, which motivates the pursuit of superior impedance modulation without changing the shapes of sound absorbers.

2.3 Tunable perfect sound absorption based on neck-embedded Helmholtz resonators

As the last section shows, the effective propagation length can be enlarged in a structure with greatly reduced thickness by curling up the channels, which consequently allows low-frequency total absorption based on structures having ultra-thin thicknesses [28, 30, 33, 38, 42]. Here, this section will demonstrate that increasing the acoustic mass of a Helmholtz resonator can be another effective method to create a great delay of phase inside a much thinner structure [Fig. 2.9]. In fact, the concept of introducing embedded neck has been employed in a number of previous studies to enhance the low-frequency transmission loss [43-47], sound absorption [48, 49], and the control of reflected waves [50], but the improved impedance modulation realized by embedded necks has been rarely explored. Here, by systematically investigating the neck-embedded Helmholtz resonators (NEHRs), it is revealed theoretically and experimentally that the NEHRs can realize considerably tunable perfect absorption performances even under the constraint of a fixed shape, proving the greatly improved capability of impedance modulation compared with traditional Helmholtz resonators (HRs).

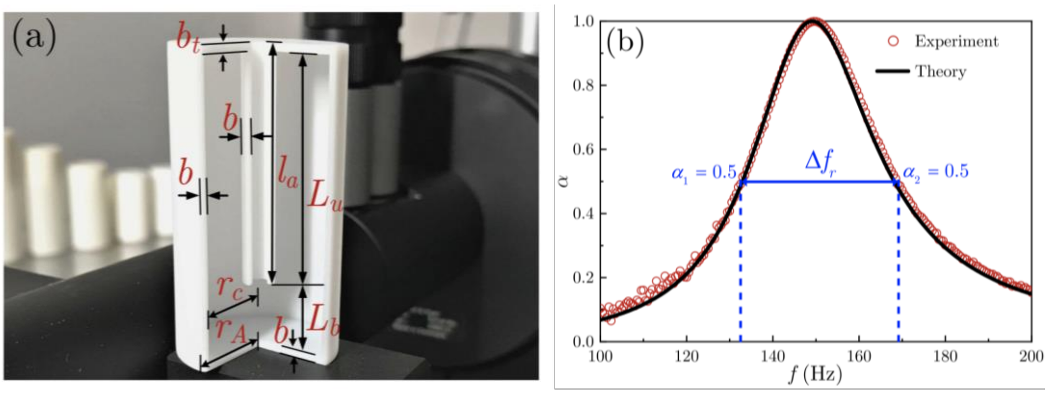

Figure 2.9 A neck-embedded Helmholtz resonator (NEHR) and the absorption performance. The NEHR is with d_A = 29 mm, d_c = 26.6 mm, L = 50 mm, d_a = 3.5 mm, l_a = 40 mm, and b_t = b = 1 mm (represented from [40]).

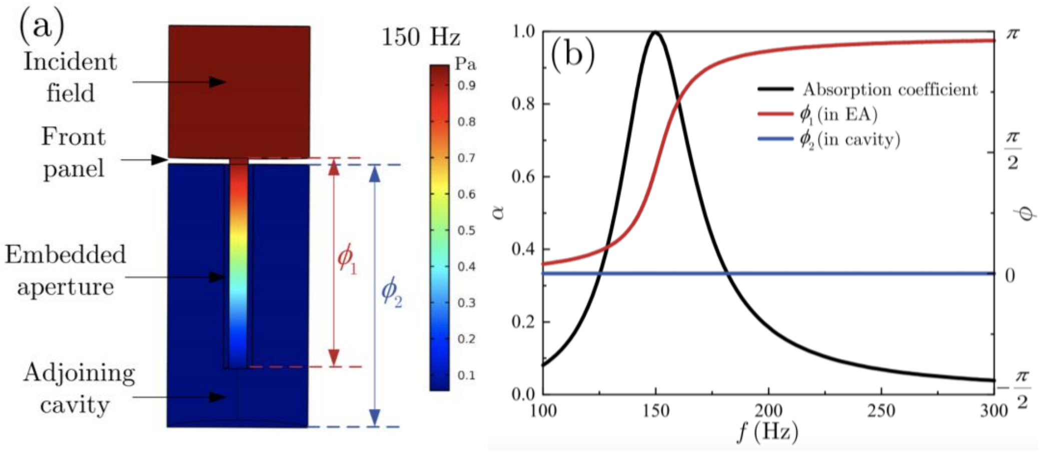

Figure 2.10 Phase delay inside a neck-embedded Helmholtz resonator.

(a) Sound pressure distribution of a NEHR (center slice view). The NEHR is the same as the structure in Fig. 2.9. (b) Absorption coefficients (corresponding to the left ordinate) and phase delay (corresponding to the right ordinate) of the NEHR. The phase delay of the embedded neck is calculated from its top opening to the bottom terminal, and the phase delay of the backed cavity is from its bottom boundary to its top boundary (represented from [40]).

As shown in Fig. 2.9, the presented NEHR can realize total absorption via an ultra-thin structure of 1/46th of the operating wavelength at 149.75 Hz, and meanwhile, the structure is considered simpler as well as easier to fabricate. The experimental structures are produced by the 3D printing and the measurements of sound absorption coefficients are conducted using an impedance tube having a diameter of 29 mm. To uncover the phase delays inside the NEHR, simulations based on COMSOL Multiphysics were performed. Figure 2.10(a) illustrates the sound pressure’s distribution by analyzing a NEHR the same as the structure in Fig. 2.9. As discussed above, it is essential to realizing a large phase change via a structure having thin thickness for constructing ultra-thin perfect absorbers. For this NEHR, it can be observed that the large phase delay is realized along with the wave propagation inside the embedded neck rather than the adjoining cavity. As shown in Fig. 2.10(b), acoustic waves in the embedded neck have a large phase change within a relatively small length, which is also different from the results that relatively slow phase delay occurs along a curled long channel. In addition to the realization of an ultra-thin perfect absorber, more importantly, the proposed NEHR can offer extraordinary performance on impedance modulation that facilitates highly tunable absorption performances.

In addition, a normal Helmholtz resonator that doesn't embed the neck (inset of Fig. 2.11) is presented to make a comparison to the NEHR exhibiting a similar absorption performance. As shown in Fig. 2.11, the thickness of the NEHR is remarkably reduced thanks to the embedded neck. Also, the concept of embedding necks is also capable of greatly decreasing the weight of the structure. More importantly, the neck-embedded Helmholtz resonators can achieve greatly tunable absorption performance. Before demonstrating this, the theoretical model for NEHRs is fristly presented.

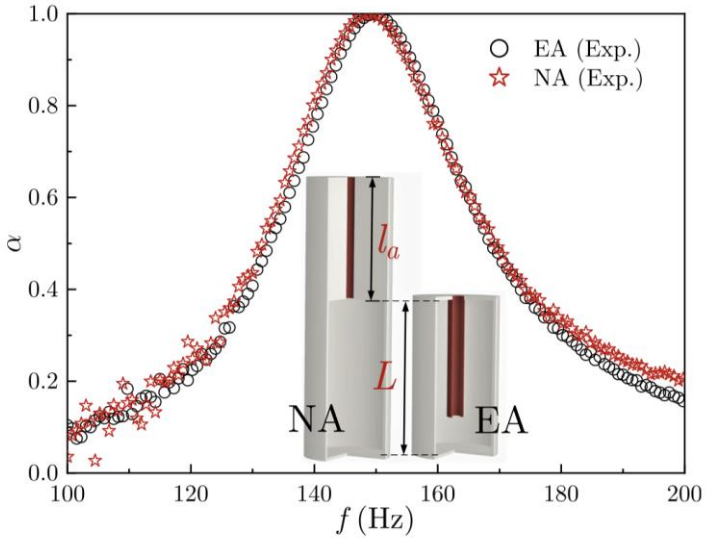

Figure 2.11 The absorption coefficients of a NEHR and a traditional Helmholtz resonator (HR). The NEHR is the same as the structure in Fig. 2.9 [40].

The impedance model for a long neck considering the effects of both thermal and viscous losses has been demonstrated in Eq. (2.13), which is also applicable for

NEHRs. Nevertheless, the embedded neck results in an irregular shape of the cavity (see Fig. 2.9(a)), which demands revisions for calculating the acoustic impedance of the irregular-shaped cavity. This thesis presents three different revised formulas for this issue. Firstly, when the operating wavelength of the NEHR is much longer than the structural thickness, the irregular-shaped cavity can be ideally treated using the acoustic lumped parameter model, where its acoustic impedance reads,

$$Z_{\mathrm{V}} = -\mathrm{j}\frac{A\rho_{\mathrm{cc}}c_{\mathrm{cc}}^{2}}{\omega V}. \tag{2.14}$$

where V indicates the cavity's volume, ρ_{cc} and c_{cc} represent the effective air density and the effective sound speed inside the irregular-shaped cavity considering the thermal-viscous losses but neglecting the effect of the embedded necks. A is the area of the surface of the NEHR.

When the thickness of the NEHR is increased to a larger level, such as larger than 1/20th of the operating wavelength, it may lead to better accuracy by introducing a geometric-based revision factor τ_{Ω}, and then the acoustic impedance of the cavity reads

$$Z_{\mathrm{cavity}} = -\mathrm{j}\frac{A\rho_{\mathrm{cc}}c_{\mathrm{cc}}\tau_{\Omega}}{S_{\mathrm{c}}}\cot(k_{\mathrm{cc}}L) \tag{2.15}$$

where $\tau_{\Omega} = S_{\mathrm{c}}L/[S_{\mathrm{c}}L - S_{\mathrm{a}}'(l_{\mathrm{a}} - b)]$, L is the cavity's innder length, S_{c} is the cavity's inner cross-sectional area, $S_{\mathrm{a}}' = \pi[(d_{\mathrm{a}}/2) + b]^2$ is the cross-section of the embedded neck including the wall. Thus, the overall surface impedance of the NEHR is able to be obtained by $Z = Z_{\mathrm{cavity(V)}} + Z_{\mathrm{a}}$.

The main advantage of the two theoretical models above is the reduced complexity in calculations. However, they are both the approximate models for certain circumstances. In the cases that the embedded neck is relatively long and the thickness of the cavity is not very thin, to ensure the accuracy of the cavity's acoustic impedance, it will be with the better accuracy to use the theoretical model employing the transfer-matrix method (TMM). The TMM-based model of acoustic impedance will be introduced in Chapter 3. In this section, the analyzed NEHRs are all with deep subwavelength thicknesses, so that Eq. (2.14) is employed for designing the experimental samples.

Guided by the theoretical model of NEHRs presented above, a series of NEHRs with a fixed external shape is designed for demonstrating the superior impedance modulation and highly tunable perfect absorption performances. It should be noticed that for the previously mentioned curled-space metasurfaces [28-30] and the traditional Helmholtz resonators, the largely tunable perfect absorption is extremely challenging to realize under a fixed external shape. Here, four NEHRs with the same external shape are presented [Fig. 2.12(a)], which theoretically and experimentally confirms the tunable perfect absorption with different peak frequencies and absorption bandwidths [Fig. 2.11(b)]. Notice that the four samples are just the proof-of-concept designs, and actually the total absorption at arbitrary frequencies among the frequency-band intervals among the four peaks can be also easily realized under a constant external shape.

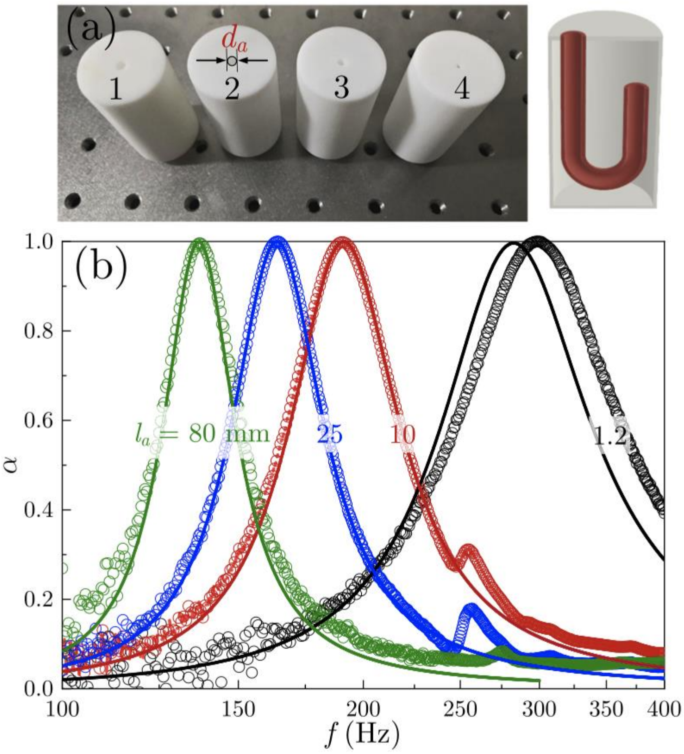

Figure 2.12 Tunable perfect absorption performances with NEHRs.

(a) Picture of the fabricated structures. The geometric parameters are given in Table 2.1.

(b) The absorption coefficients of the four NEHRs. The solid lines indicate the theoretical results and the dots are the experimental results [40].

Table 2.1 Geometrical parameters of the experimental structures in Fig. 2.12.

No.	l_a (mm)	d_a (mm)
1	80	4.4
2	25	3.1
3	10	2.4
4	1.2	1.6

In summary, this section systematically investigated the neck-embedded Helmholtz resonators (NEHRs). The highly tunable perfect-absorption performances of the NEHRs with an unchanged external shape are demonstrated theoretically and experimentally. The NEHRs are able to modulate the acoustic impedance more freely and powerfully, which will facilitate the development of ultra-thin and high-efficiency metasurface-based sound absorbers operating in broadband frequency ranges [25, 51-55].

3. Chapter 3: Broadband Sound Absorption Based on Coupled Acoustic Metasurfaces

3.1 Background of coupled acoustic metasurfaces for broadband absorption

Owing to the interesting underlying physics of broadband absorption and the tremendous relevant application in impedance and noise-control engineering, the realization of broadband sound absorption with structures having deep sub-wavelength thicknesses has received extensive and continuing attention. In previous studies, a straightforward technique widely employed is to employ a series of resonators capable of high-efficiency absorption and then piece together their relatively narrow absorption bands to a broad absorbing band. For instance, through coupling six curled channels that individually provide six perfect absorption performances with narrow absorption bands, a broadened sound-absorbing can be achieved [Fig. 3.1]. The central frequencies of the individual absorption bands are at 109, 118, 128, 144, 157, and 171 Hz, respectively, resulting in an efficient absorption band from 105-177 Hz [30]. Besides, it is found that the absorption curve suffers from many absorption dips among the frequency range of the near two absorption peaks. These absorption dips result from the antiresonances caused by the interaction of two resonant modes, which can be greatly alleviated by adding a layer of porous materials near the front surface of the coupled metasurfaces [56-59], while the added porous materials may hinder the application for some extreme environments with high humidity and low temperature. Besides, it is also interesting to find a new physical mechanism to suppress the antiresonance-induced absorption dips.

In addition to coupling several Fabry-Pérot (FP) channels, another effective method for broadband absorption is to employ Helmholtz resonators with gradient dimensions that individually provide highly efficient absorption at designed frequencies. As shown in Fig. 3.2, more fluent absorption can be realized by this design, whereas the different dimensions of the Helmholtz resonators bring about the unused space and make the whole structure thicker [60].

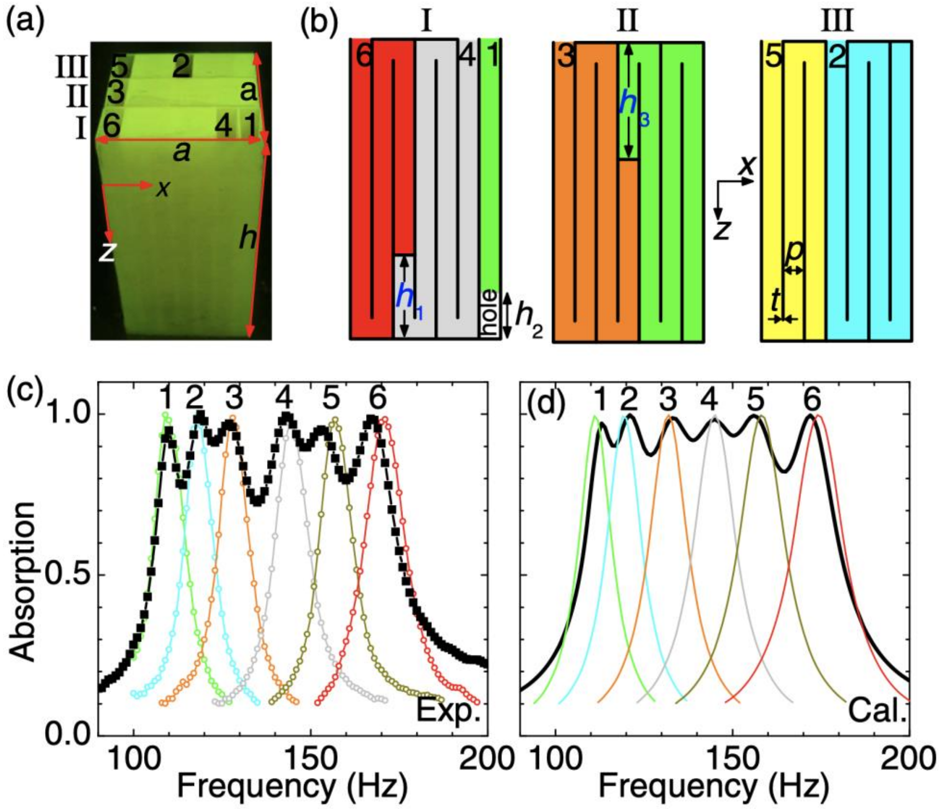

Figure 3.1 Broadband sound absorption based curled channels with perfect absorption. (a) Photograph of the coupled acoustic metasurfaces consisting of six curled Fabry-Pérot (FP) channels. (b) Schematic of the detailed arrangement of the six channels (indicated with different colors). (c)-(d) The experimental and theoretical results [30].

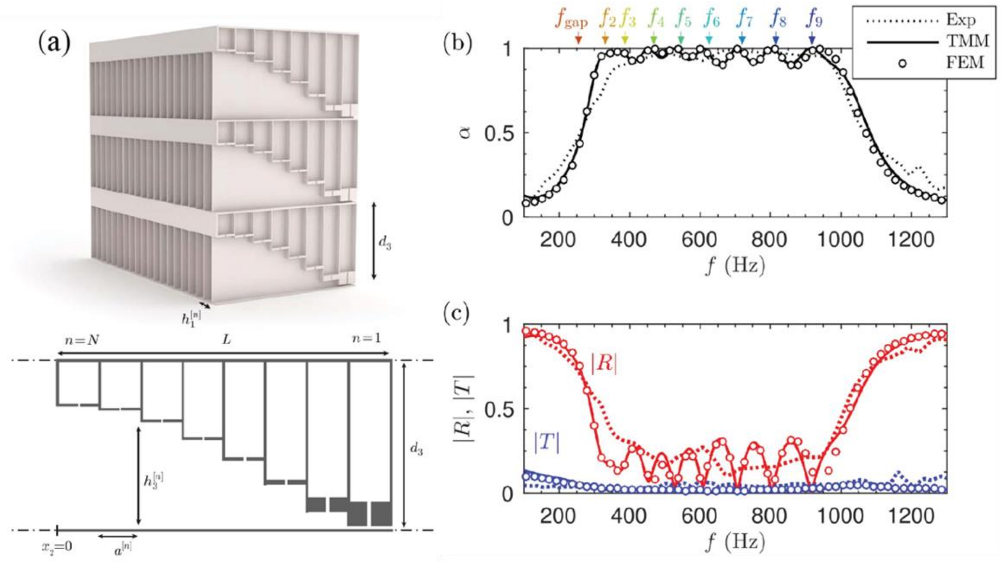

Figure 3.2 Broadband sound absorption based gradient HRs.

(a) Schematic of the detailed arrangement of the “rainbow-trapping” sound-absorbing structure with gradient Helmholtz resonators. (b)-(c) The absorption, refection and transmission properties (represented from [60]).

Furthermore, as will be demonstrated later, in the designs that require the individual resonators having high absorption at the certain frequencies [30, 56, 60-64], the requirement of total absorption actually attaches a rather strict constraint on each resonator, which gives rise to an additional restriction on the modulation of coherent coupling among the resonators and also brings about a barrier in realizing thinner structures. In this thesis, a counter-intuitive but more efficient way is presented: utilizing the strong nonlocal coupling among imperfect resonators exhibiting inferior absorption to construct a compact broadband sound absorber against significant absorption dips. In the following, this thesis will firstly demonstrate the theoretical model for the coupled metasurfaces and then manifest the design concept of broadband absorption via imperfect components.

3.2 Theoretical model of the coupled acoustic components

To analyze the coherent coupling effect of multiple acoustic components, a two-dimensional model is presented. The acoustic 2D coupled acoustic metasurface is considered periodic in the *x*-direction. And without loss of generality, its unit cell (length *A*) consists of two air cavities (see Fig. 3.3). Here, all the structural boundaries are considered to be acoustically rigid, which can be ideally satisfied in practical structures if their building materials have much larger characteristic acoustic impedance than air. In the domains with z > 0, the sound pressure $p(\mathrm{x}, \mathrm{z})$ satisfies $\nabla^2 p + k_0{}^2 p = 0$, and in the cavity No. 1(2), the acoustic pressure $p_{\mathrm{c1(2)}}\ (x, z)$ follows $\nabla^2 p_{\mathrm{c1(2)}} + k_{\mathrm{c1(2)}}{}^2 p_{\mathrm{c1(2)}} = 0$, where $k_{\mathrm{c1(2)}}$ represents the effective acoustic wave number. Then, the following expressions of sound pressures can be obtained,

$$p(x,z) = \sum_{i=-N}^{N} \mathrm{C}_i \exp(-\mathrm{j}k_{zi}z) + D_i \exp(\mathrm{j}k_{zi}z)\ \exp(-\mathrm{j}k_{xi}x), \qquad \textbf{(3.1)}$$

$$p_{\mathrm{c1}}(x,z) = \sum_{\Lambda=0}^{N_{\mathrm{s}}} \left[E_\Lambda e^{\mathrm{j}\sqrt{k_{\mathrm{c1}}^2 - k_\Lambda^2}z} + F_\Lambda e^{-\mathrm{j}\sqrt{k_{\mathrm{c1}}^2 - k_\Lambda^2}z} \right] \cos(k_\Lambda(x - a_1)), \qquad \textbf{(3.2)}$$

$$\begin{aligned} p_{\mathrm{c2}}(x,z) = \sum_{\Lambda=0}^{N_{\mathrm{s}}} &\left[G_\Lambda e^{\mathrm{j}\sqrt{k_{\mathrm{c1}}^2 - k_\Lambda^2}z} + H_\Lambda e^{-\mathrm{j}\sqrt{k_{\mathrm{c1}}^2 - k_\Lambda^2}z} \right] \\ &\times \cos(k_\Lambda(x - (a_1 + w_1 + a_2))), \end{aligned} \qquad \textbf{(3.3)}$$

where $k_{xi} = i2\pi/A$, and $k_{xi}{}^2 + k_{zi}{}^2 = k^2$, $k_\Lambda = \Lambda\pi/w$, C_i and D_i indicate the complex amplitudes of the sound of incidence and reflection respectively, E_Λ and F_Λ are the sound waves' complex amplitudes inside the cavity No. 1, G_Λ and H_Λ represent the complex amplitudes inside the cavity No. 2, with, $\Lambda = 0, 1, 2, 3, \cdots, N_{\mathrm{s}}$ and $i = 0, \pm1, \pm2, \cdots, \pm N$. Note that for the hard-boundary condition in impedance-tube experiments, the term $\exp(-\mathrm{j}k_{xi}x)$ should be replaced by $\cos(k_{xi}x)$. Here the periodic boundary condition is assumed in the theoretical analysis so that it may apply to a wider range of potential applications that the absorbers are arranged periodically. In addition, considering the condition of acoustic continuity at the surface boundary ($z = 0$), it gives

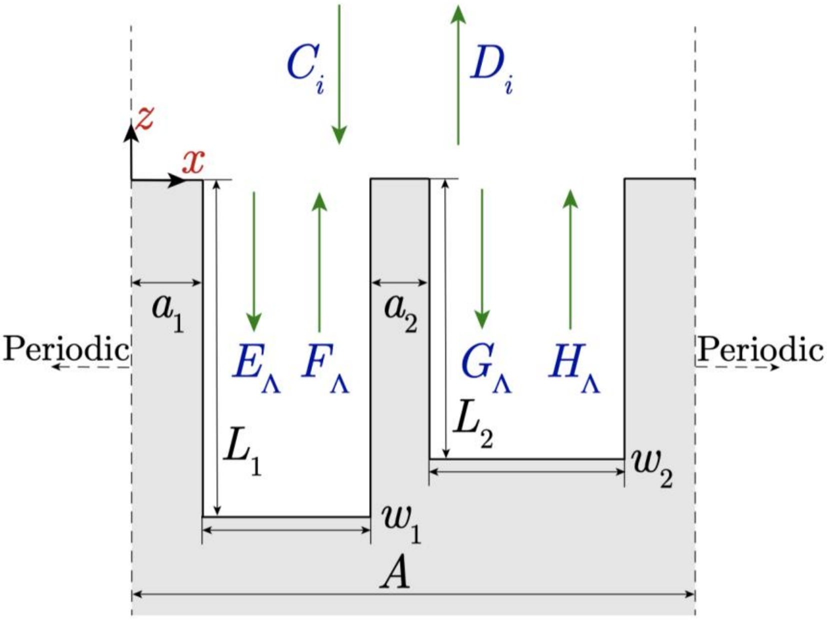

Figure 3.3 A two-dimensional analytical model of coupling components. The investigated structure is periodically arranged in the *x*-direction with this cell [25].

$$p(x,z)=\left\{\begin{array}{c} p_{\mathrm{c1}}(x,z)\ \ \text{for}\ \ a_1 < x < a_1 + w_1 \\ p_{\mathrm{c2}}(x,z)\ \text{for}\ \ a_1 + w_1 + a_2 < x < a_1 + w_1 + a_2 + w_2 \end{array}\right\}, \tag{3.4}$$

$$\rho_0^{-1}\frac{\partial p}{\partial z} = \left\{\begin{array}{c} \rho_{\mathrm{c1}}^{-1}\dfrac{\partial p_{\mathrm{c1}}}{\partial z}\ \ \text{for}\ \ a_1 < x < a_1 + w_1 \\ \rho_{\mathrm{c2}}^{-1}\dfrac{\partial p_{\mathrm{c2}}}{\partial z}\ \text{for}\ \ a_1 + w_1 + a_2 < x < a_1 + w_1 + a_2 + w_2 \\ 0\ \ \ \text{for the rest} \end{array}\right\}, \tag{3.5}$$

where ρ_{c1} and ρ_{c2} are the complex air density in the cavities No.1 (the left cavity) and No.2 (the right cavity) respectively. Note that Eq. (3.5) indicates the continuity of particle velocity of air, and actually employing the continuity of particle volume velocity can also obtain the same results. According to previous studies [40, 65], it can be satisfied both inside the cavities (where $\lambda \gg w$) and above the overall structure ($\lambda \geq 2A$) that the fundamental wave mode dominates in the frequency band of interest (. In such case, applying a hard-boundary condition or a periodic boundary condition will not bring out significant difference. In addition, due to the rigid ends of the two cavities, it can be deduced that $F_\Lambda = E_\Lambda \mathrm{e}^{-\mathrm{j}2k\Lambda L1}$ and $H_\Lambda = G_\Lambda \mathrm{e}^{-\mathrm{j}2k\Lambda L2}$ at the coupled metasurface's surface (z = 0). After integrating Eqs. (3.4)-(3.5) over A, it obtains

$$C_0 + D_0 = E_0 \;\; 1 + \mathrm{e}^{-\mathrm{j}2k_{\mathrm{c}1}L_1} \;\; , \quad \textbf{(3.6)}$$

$$C_0 + D_0 = G_0 \;\; 1 + \mathrm{e}^{-\mathrm{j}2k_{\mathrm{c}2}L_2} \;\; , \quad \textbf{(3.7)}$$

$$\begin{aligned} A\rho_0^{-1}k_0(C_0 - D_0) &= w_1\rho_{\mathrm{c}1}^{-1}k_{\mathrm{c}1}E_0 \;\; 1 - \mathrm{e}^{-\mathrm{j}2k_{\mathrm{c}1}L_1} \\ &+ w_2\rho_{\mathrm{c}2}^{-1}k_{\mathrm{c}2}G_0 \;\; 1 - \mathrm{e}^{-\mathrm{j}2k_{\mathrm{c}2}L_2} \;\; . \end{aligned} \quad \textbf{(3.8)}$$

Then, the reflection factor (R_F) as well as the surface acoustic impedance of the coupled metasurfaces (Z) are given by

$$R_\mathrm{F} = \left|\frac{D_0}{C_0}\right|^2 = \left|\frac{Z - \rho_0 c_0}{Z + \rho_0 c_0}\right|^2 . \quad \textbf{(3.9)}$$

Moreover, the surface impedance of cavities No.1 (Z_1) and No. 2 (Z_2) can be respectively written as

$$Z_1' = -\mathrm{j}\rho_{\mathrm{c}1}c_{\mathrm{c}1}\cot(k_{\mathrm{c}1}L_1) = \rho_{\mathrm{c}1}c_{\mathrm{c}1}\frac{1 + \mathrm{e}^{-\mathrm{j}2k_{\mathrm{c}1}L_1}}{1 - \mathrm{e}^{-\mathrm{j}2k_{\mathrm{c}1}L_1}}, \quad \textbf{(3.10)}$$

$$Z_2' = -\mathrm{j}\rho_{\mathrm{c}2}c_{\mathrm{c}2}\cot(k_{\mathrm{c}2}L_2) = \rho_{\mathrm{c}2}c_{\mathrm{c}2}\frac{1 + \mathrm{e}^{-\mathrm{j}2k_{\mathrm{c}2}L_2}}{1 - \mathrm{e}^{-\mathrm{j}2k_{\mathrm{c}2}L_2}}. \quad \textbf{(3.11)}$$

Then, dividing Eq. (3.8) by the term "C_0 +D_0" and combining the result with Eqs. (3.6)-(3.7) and Eqs. (3.10)-(3.11) will give

$$A\rho_0^{-1}k_0\frac{C_0 - D_0}{C_0 + D_0} = \omega(w_1 / Z_1' + w_2 / Z_2'). \quad \textbf{(3.12)}$$

By combining Eq. (3.12) and (3.9), it obtains

$$Z = \frac{AZ_1'Z_2'}{w_2 Z_1' + w_1 Z_2'}. \quad \textbf{(3.13)}$$

For a coupled metasurface, the acoustic impedance of the component absorbers could be expressed regarding the surface area of the whole coupled system. Considering that wave impinges on the surface of the overall system and all the component absorbers are inoperative (replaced by hard walls) except for the certain one component absorber, and then the acoustic impedance of this individual component absorber is defined. Then, now the acoustic impedance of cavities No.1 and No.2 regarding the whole coupled metasurface are $Z_1 = -\mathrm{j}A\rho_{c1}c_{c1}\cot(k_{c1}L_1)/w_1$ and $Z_2 = -\mathrm{j}A\rho_{c2}c_{c2}\cot(k_{c2}L_2)/w_2$, respectively. Accordingly, Eq. (3.13) can be rewritten as $1/Z = 1/Z_1 + 1/Z_2$. In a similar way, the acoustic impedance of a coupled metasurface consisting of multiple components can be obtained, which reads

$$Z = 1 \,/\, \sum_{n=1}^{N} {Z_{(n)}}^{-1}. \tag{3.14}$$

Based on Eq. (3.14), the coherent coupling effect of multiple acoustic components can be theoretically calculated.

3.3 Broadband sound absorption based on imperfect component metasurfaces

This section will theoretically investigate and experimentally verify the broadband sound absorption via imperfect component metasurfaces. Distinct from the commonly-used technique in previous studies, the absorbing metasurfaces are now achieved based on the coupling of imperfect components. Despite the fact that every component metasurface presents inferior absorption solely, by modulating their coherent coupling, these components can offer a collective highly efficient acoustic absorption in a broad frequency band, which brings about a new pathway for developing highly efficient as well as broadband sound absorbers.

To begin with, the vital impact of coherent coupling in controlling the absorption property of the whole coupled metasurface is demonstrated. For simplicity and better illustration of the physical picture, this thesis firstly investigates two contrastive metasurfaces that are composed of 4 perfect sound absorbers [Fig. 3.4(a)] as well as 4 imperfect sound absorbers [Fig. 3.4(d)], respectively. The complex frequency plane [60, 66, 67] is employed to manifest qualitatively their distinct coupling characteristics. In a hypothetical system without any thermal-viscous losses, a pair of “zero” and “pole” will exhibit a symmetrical distribution on the two sides of the real frequency axis. Here, the imaginary wavenumber (k_i) is introduced to the intrinsic wavenumber of the metasurface (k_e), which gives $k' = k_e + jk_i$. Note that generally the imaginary wavenumber is introduced in the form of $k' = k_e - jk_i$, so the locations of the zeros and poles in this section are reversed compared to this. By taking the thermal-viscous losses of the system into consideration, the "zero" as well as the "pole" will move towards the upward direction of the vertical axis (imaginary frequency). Hence, when the zero is at the abscissa axis (real frequency), intrinsic losses (thermal-viscous losses) successfully balance the radiation losses, leading to perfect absorption. From Fig. 3.4(b), it is found that P1 realizes total absorption at 144 Hz. Following the concept of constructing broadband absorption based on perfect components [Fig. 3.4(a)], the results from the complex frequency plane uncover that although every component structure (P1–P4) shows a "zero" exactly at the axis of real frequency (indicating perfect absorption), the sound absorption of the whole coupled structure is unsatisfactory. In fact, the quasi-perfection domain, defined as the area inside the contour line in black ($\alpha = 0.9$), is broad on the whole plane, but the widest part of the domain does not locate at the real frequency axis. Figs. 3.4(a)-(c) demonstrate that the perfectly sound-absorbing components cannot straightforwardly guarantee a desired coupled metasurface resulting from the coherent coupling among the components.

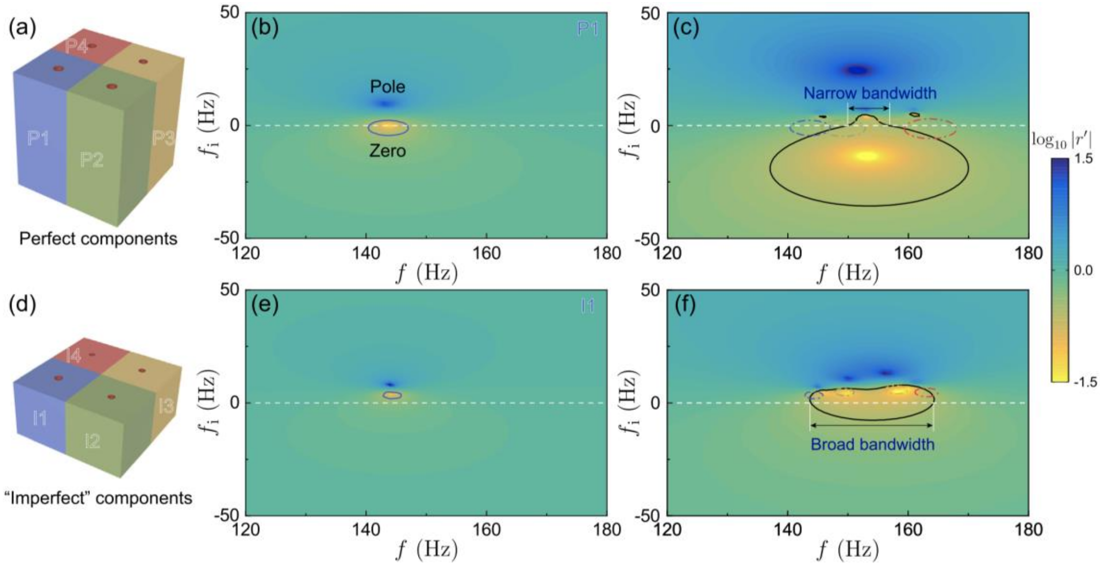

Figure 3.4 Demonstrations of coupled metasurfaces consisting of perfect components and imperfect components.

(a) The coupled structure composed of four perfect absorbers (P1–P4). (b) The perfect component P1 based on a complex frequency plane. The perfect absorption of P1is witnessed by the “zero” located at the abscissa axis（real frequency, the white line of f_i = 0). The solid line marks a contour line with α = 0.9. (c) The coupled structure with four perfect components is illustrated with a complex frequency plane. The areas inside the contour lines represent the “quasi-perfection domain”. (d) The coupled structure composed of four imperfect absorbers (I1–I4). (e) The perfect component I1 based on a complex frequency plane. (f) The coupled structure with four imperfect components is illustrated with a complex frequency plane [25].

Based on the vital role of coherent coupling in constructing broadband sound absorbers, this thesis presents a new design methodology by exerting the coherent coupling to an unprecedented level and leaving away the components’ individual sound-absorbing abilities. In other words, the design concept is with the goal of utilizing the coherent coupling dominantly to realize a highly efficient and broadband sound-absorbing metasurface. For simplicity, 4 imperfect components (I1–I4) exhibiting similar resonance frequencies compared with the four perfect components are provided, where each of them shows poor individual absorption performance [Fig. 3.4(d)]. For instance, the zero of one imperfect component (I1) locates above the real frequency axis, indicating an imperfect absorption peak caused by excessive acoustic resistance [Fig. 3.4(e)]. Nevertheless, by tailoring the coherent coupling, the real frequency axis rightly crosses the widest domain with quasi-perfect sound absorption so that the coupled metasurfaces realizes excellent absorption from 144 to 164 Hz [Fig. 3.4(f)]. Figure 3.4 proves the feasibility of achieving superior broadband sound absorption based on imperfect components compared with perfect components.

The above offers a general concept of high-efficiency broadband sound absorption based on imperfect components, where the components are considered general resonators. In the following, the specific designs are presented.

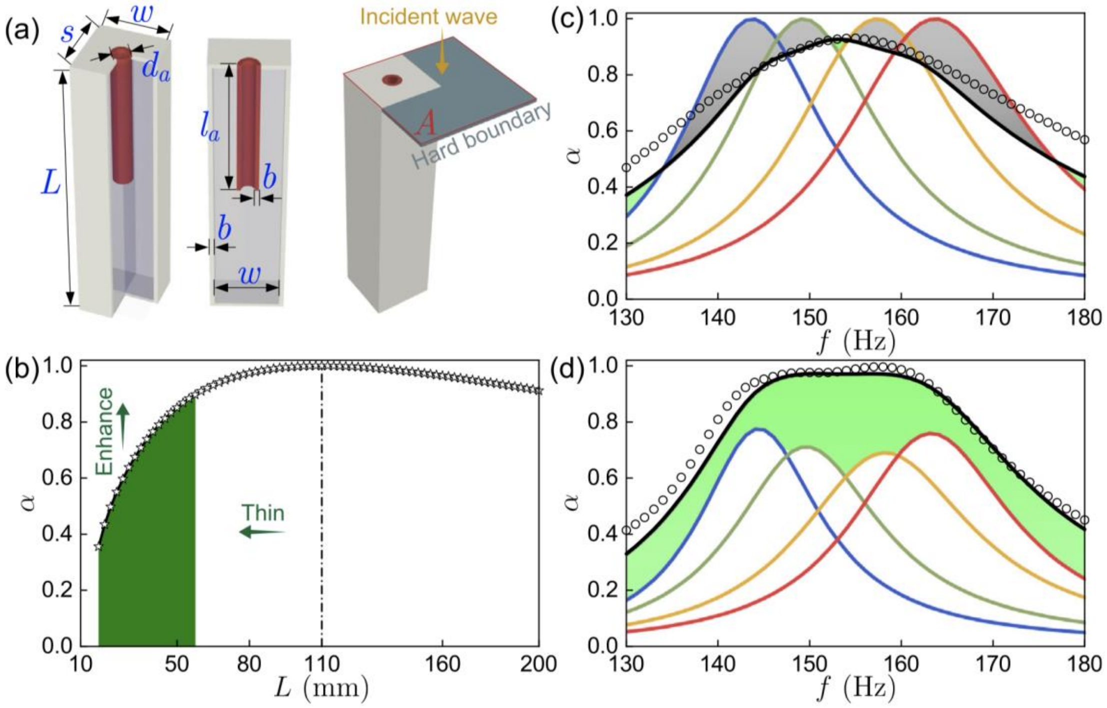

Figure 3.5 Coupled metasurfaces having perfect sound absorbers and imperfect sound absorbers.

(a) Neck-embedded Helmholtz resonator (NEHR). (b) Absorption coefficients of a NEHR with the variation of thickness (L). The resonant frequency is fixed (144 Hz). The green area marks the imperfect components whose absorption peaks are imperfect but thicknesses are compressed. Modulating the coherent coupling is able to improve the absorption performance of a coupled metasurface based on imperfect absorbers.

Absorption performances of the coupled sound absorbers with perfect (c) as well as imperfect (d) absorbers. [25].

Firstly, the neck-embedded Helmholtz resonators (NEHRs) investigated in Chapter are now employed as the fundamental component [Fig. 3.5(a)]. The NEHRs can offer efficient modulation of the impedance by modulating the embedded necks and meanwhile ensuring the same thickness of the components [40]. Hence, the assembly of multiple NEHRs achieves a compact structure. For the structure will be presented in the following, the NEHRs have a rather thin thickness compared to the operating wavelength, so that the theoretical model according to Eq. (2.15)is employed [40], which reads [25]

$$Z=\frac{A}{S_{\mathrm{a}}}\left[\begin{array}{l}\rho_0 c_0 \dfrac{2\mathrm{j}\sin(\frac{k_{\mathrm{ca}} l_{\mathrm{a}}}{2})}{\sqrt{(\gamma-(\gamma-1)\Psi_{\mathrm{ha}})\Psi_{\mathrm{va}}}} \\ +2\sqrt{2\omega\rho_0\eta}+j\omega\rho_0\delta_\Omega-\dfrac{\mathrm{j}S_{\mathrm{a}}\rho_{\mathrm{cc}}c_{\mathrm{cc}}\tau_\Omega}{S_{\mathrm{c}}}\cot(k_{\mathrm{cc}}L)\end{array}\right], \tag{3.15}$$

where A is the surface area of the whole coupled metasurface, S_a and S_c indicate the cross-sections of the neck and the adjoining cavity. Ψ_{ha} and Ψ_{va} refer to the thermal and viscous effect inside the embedded neck (See Eqs. (2.4)-(2.5)), respectively. The definitions of δ_Ω and τ_Ω refer to Eqs. (2.13) and (2.15). Note that in reference [25], Eq. (3.15) has a typo with a needless negative sign “-” ahead of the first term on the right side of this equation, and a factor “2” is omitted for the second term on the right side of this equation.

In the next, the relationship between the thickness of a NEHR and the absorption coefficient is analyzed to demonstrate how the coupled metasurfaces composed of imperfect sound absorber can have enhanced sound absorption via thinner structures. As shown in Fig. 3.5(b), absorption coefficients for a NEHR are illustrated with the increase of thickness but maintaining a resonant frequency of 144 Hz. For perfect absorption, a NEHR should have a thickness of around 110 mm due to the strict requirements of acoustic impedance. However, with the decreases of *L*, it is found that a lower absorption leading to an imperfect NEHR. Nevertheless, the imperfect NEHR possesses an extraordinary advantage, a largely reduced thickness.

Then, it is demonstrated that by adjusting the coherent coupling among the imperfect NEHRs, the coupled metasurface can provide a largely broadened working frequency band with considerably improved absorption efficiency as well as reduced thickness. For combining 4 perfect NEHRs, it presents moderate absorption efficiency and bandwidth [Fig. 3.5(c)]. Here, the curves of sound absorption (colored lines) of the individual perfect components are also presented. The marked domain in green (grey) represents that enhancement (reduction) in terms of absorption coefficient of the coupled metasurface compared to individual components, which can evidently manifest the enhanced (depressed) absorption resulting from the coherent coupling. It is found from Fig. 3.5(c) that the acoustic absorption of the coupled metasurfaces could be significantly depressed when the coherent coupling is not well-tuned.

On the contrary, for the coupled metasurface based on 4 imperfect NEHRs, despite that the individual NEHRs have imperfect absorption peaks, the acoustic absorption performance of the whole coupled metasurface is remarkably improved, leading to a quasi-perfect sound absorber in a wide frequency band [Fig. 3.5(d)]. In addition, the metasurface via imperfect NEHRs can have a thinner structure (50 mm) than that of the metasurface with perfect NEHRs (112 mm). Actually, the method of coupling imperfect components enables the coherent coupling to control the absorption performance of the whole coupled metasurface, which overcomes the strict restrictions of acoustic impedance for the individual components.

The coupled metasurfaces presented above are the prototypes, where employing just 4 NEHRs is to provide a better illustration of the underlying working mechanism. In fact, adopting more components is able to support the stronger coherent coupling and realize better sound absorption within a wider frequency bandwidth. In what follows, by modulating the coherent coupling among 25 NEHRs with a unanimous thickness, more broadband sound absorption is achieved [Fig. 3.6(a)].

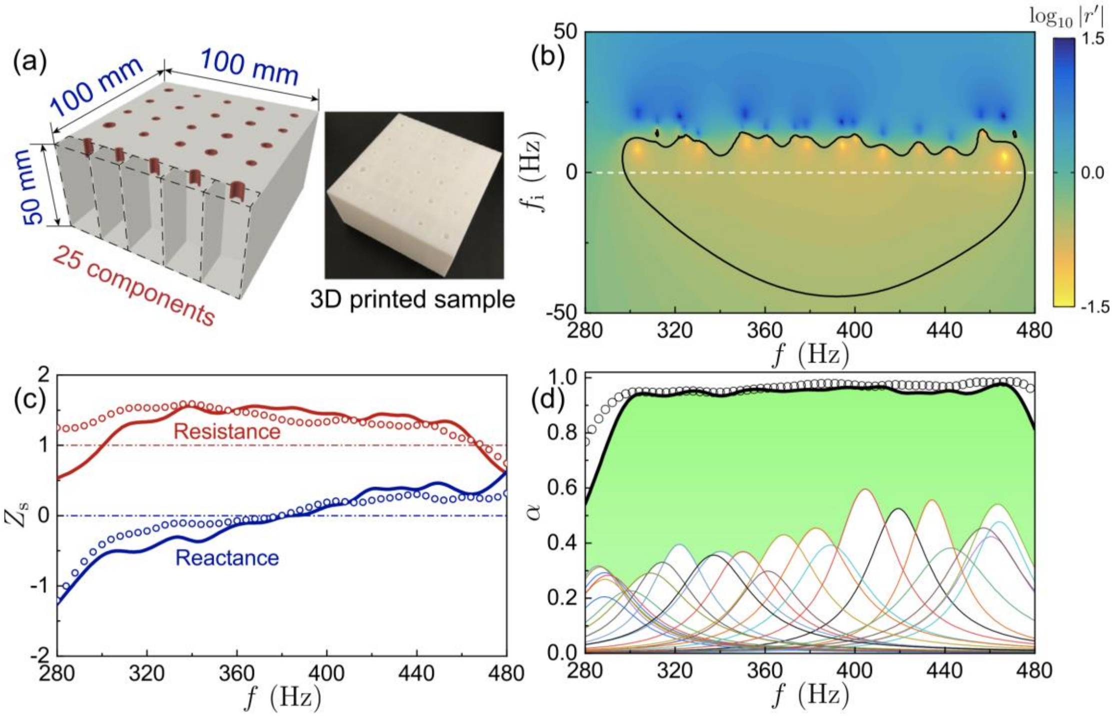

Figure 3.6 The parallelly coupled metasurfaces based on imperfect components.

(a) Coupled metasurface composed of 25 imperfect component NEHRs. (b) The reflection performance of the coupled metasurface illustrated by a complex frequency plane. (c) The lines and circles indicate the calculated and measured acoustic impedance of the coupled metasurfaces, respectively. (d) The black line and the black circles represent the theoretical and experimental results of absorption coefficients of the coupled metasurfaces, respectively. The colored lines are the theoretical results of absorption coefficients of the NEHRs [25].

Based on the complex plane analysis, it is found that the broadest section of the quasi-perfection domain locates rightly at the axis indicating the real frequency (denoted by the white line at f_i = 0), indicating an optimized condition of sound absorption [Fig. 3.6(b)]. Consequently, this optimized metasurface offers sound absorption coefficients above 0.9 from 297 to 475 Hz, where the good impedance matching also validates the broadband quasi-perfect absorption [Fig. 3.6(c)]. As demonstrated in Fig. 3.6(d), compared with the inferior absorption curves of the components individually behaved (colored lines), the coupled metasurface’ absorption curve is considerably enhanced, showing a sound absorption coefficient of 0.95 in average within the band of 297–475 Hz and proving that the coherent coupling is able to effectively improve the overall absorption performance. Besides, the thickness of the coupled metasurface is at a deep-subwavelength level of 1/23th to wavelength of sound waves at 297 Hz.

By far the coupled metasurfaces proposed just utilized the parallel coupling by employing coplanar NEHRs. In fact, involving other types of coherent coupling can further improve the working bandwidth as well as absorption performance. As a proof-of-concept design, a metasurface involving the parallel coupling as well as the cascade coupling is presented, which is composed of 20 NEHRs showing imperfect absorption and an additional micro-perforated panel (MPP) [Fig. 3.7(a)]. The additional MPP is able to offer cascade coupling to the NEHRs. To investigate the effect of the MPP, a transformation matrix is applied, which reads

$$\begin{bmatrix} p_{\mathrm{t}} \\ u_{\mathrm{t}} \end{bmatrix} = \begin{bmatrix} \cos(k_{\mathrm{c}}D) & \mathrm{j}\dfrac{\omega\rho_{\mathrm{c}}}{k_{\mathrm{c}}}\sin(k_{\mathrm{c}}D) \\ \mathrm{j}\dfrac{k_{\mathrm{c}}}{\omega\rho_{\mathrm{c}}}\sin(k_{\mathrm{c}}D) & \cos(k_{\mathrm{c}}D) \end{bmatrix} \begin{bmatrix} p_{\mathrm{b}} \\ u_{\mathrm{b}} \end{bmatrix}, \tag{3.16}$$

where D is the length of the air interlayer, ρ_{c} and k_{c} represent the effective air density and wave number of the air interlayer, $p_{\mathrm{t(b)}}$ and $u_{\mathrm{t(b)}}$ indicate the sound pressure and air particle velocity at the top (bottom) of the air gap. The surface acoustic impedance of the coupled metasurface (NEHR assembly) under the interlayer is $Z_{\mathrm{b}} = p_{\mathrm{b}}/u_{\mathrm{b}}$, and the acoustic impedance at the upper surface of the air gap could be calculated through a transfer matrix, which reads,

$$Z_\mathrm{t} = p_\mathrm{t} / u_\mathrm{t} = \frac{\rho_\mathrm{c} c_\mathrm{c} (Z_\mathrm{b} + \mathrm{j}\rho_\mathrm{c} c_\mathrm{c} \tan(k_\mathrm{c} D))}{\rho_\mathrm{c} c_\mathrm{c} + \mathrm{j} Z_\mathrm{b} \tan(k_\mathrm{c} D)}, \tag{3.17}$$

where c_c is the complex sound speed within the air gap. Then, the MPP (impedance Z_m) is treated as a lumped element, and therefore the impedance of the whole metasurface reads $Z = Z_\mathrm{t} + Z_\mathrm{m}$, with

$$Z_\mathrm{m} = -\mathrm{j}\frac{\rho_0 \omega (t_\mathrm{m} + 0.85 d_\mathrm{m})}{\sigma} \frac{J_0(\kappa d_\mathrm{m} / 2)}{J_2(\kappa d_\mathrm{m} / 2)}, \tag{3.18}$$

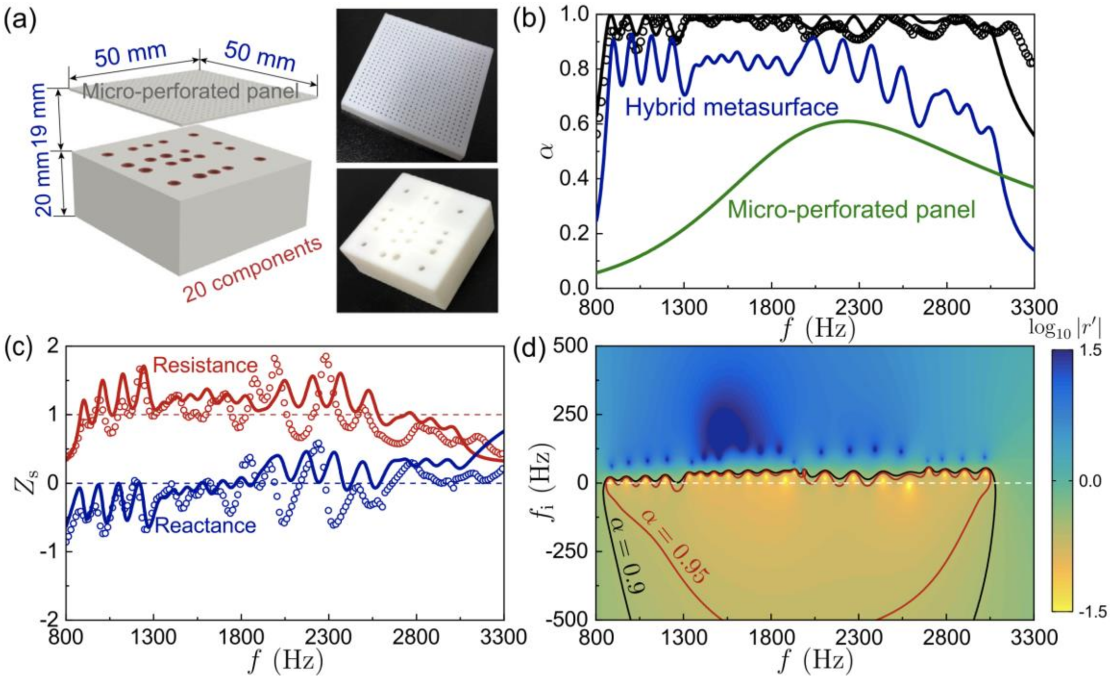

Figure 3.7 The coupled metasurface with cascade and parallel couplings.

(a) The coupled metasurface composed of 20 imperfect component NEHRs and a MPP gaped with an air interlayer of 18.3 mm. The NEHRs have a unanimous thickness of 20 mm. The MPP has an aperture diameter of 0.5 mm, a perforated ratio of 4.7%, and a panel thickness of 0.7 mm. (b) The black line and the black circles represent the theoretical and experimental results of sound absorption coefficients of the coupled metasurface. In the quasi-perfection frequency range starting from 870 Hz to 3224 Hz, the averaged absorption coefficient achieves 0.957. (c) The lines and the circles indicate the theoretical and experimental results, respectively. Acoustic resistance and acoustic reactance of the whole coupled metasurfaces are marked by red and blue, respectively. (d) The black contour and the red contour indicate α = 0.9 and $\alpha = 0.95$ [25].

Owing to that the coherent coupling effect can be theoretically calculated by Eqs. (3.17)-(3.18), it is feasible to run a numerical optimization with the goal of the highest averaged acoustic absorption coefficient in a designed frequency band. The objective of the optimization process is to modulate the coherent coupling among the components, attaining a broadband high-efficiency absorption via a most compressed structure. On the whole, the design scheme of the coupled metasurfaces can be summarized into two steps:

1) Theoretical modeling: use Eqs. (3.17)-(3.18) to theoretically calculate the coherent coupling effect;

2) Global optimization: run a numerical optimization setting the goal as the highest averaged absorption coefficient in a designed frequency band.

With the optimization process, the presented coupled metasurface exhibits a broadband quasi-perfect absorption ranging from 870 Hz to 3224 Hz via a deep subwavelength structure of 3.9 cm in thickness [Fig. 3.7(b)]. Here, the individual NEHRs, the assembly of NEHRs, and the MPP backing by an air cavity with a depth of 18.3 mm in depth, all show imperfect sound absorption, whereas the well-tuned coherent coupling enhances the overall absorption to a high level. The structure presented in Fig. 3.7 gains freer modulation on the coherent coupling so that empowers impedance tuning in a broader band. The experimentally measured averaged absorption coefficient realizes 0.957 within the quasi-perfection absorption band, where the matched acoustic impedance witnesses the excellent sound absorption performance [Fig. 3.7(c)]. In addition, if the definition of quasi-perfect absorption is raised to above 0.95, the line indicating the real frequency crosses the quasi-perfection domain (red contour) with numerous intersections [Fig. 3.7(d)]. This result shows that the metasurface is not able to preserve this high level of sound absorption efficiency (0.95) in wide frequency range. Nevertheless, from Fig. 3.7(d), it is found that a more efficient sound absorber having a nearly unchanged sound-absorbing frequency band could be realized by slightly moving the imaginary frequency axis in the positive direction. This slight shift requires the increase of the metasurface's intrinsic losses. For this presented metasurface, the increase of the intrinsic losses could be achieved by attaching two layers of foams (4 mm) below the MPP and above the NEHRs assembly [Fig. 3.8(a)].

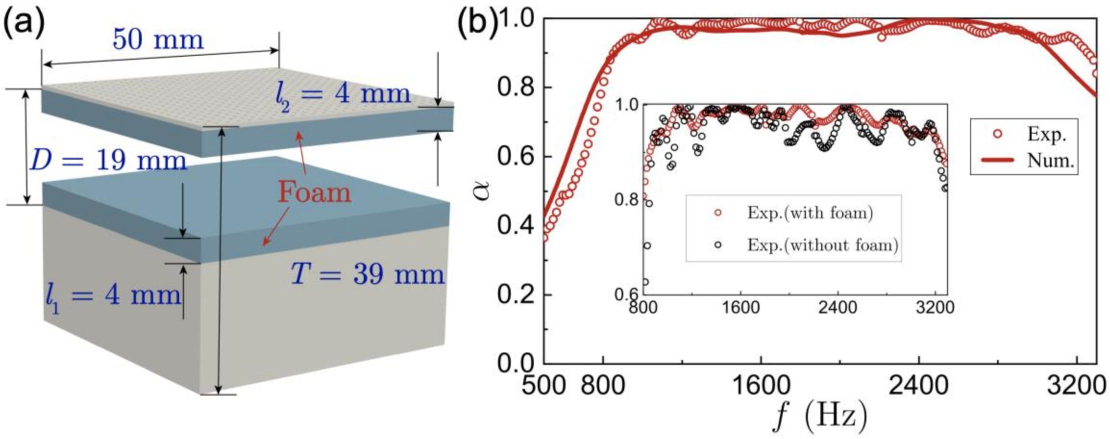

Figure 3.8 The coupled metasurfaces with foam.

(a) Schematic of the coupled metasurface with adding two layers of sponges. (b) Experimental and numerical results. The red line and red circles indicate the absorption coefficients of the coupled metasurfaces with additional foam from the simulation and the experiment respectively. The black circles in the inset indicate the absorption of the structure without the additional foam (consistent with the absorption coefficients illustrated in Fig. 3.7(b)) [25].

The adopted sponges are made of melamine having the parameters as follows: foam porosity of 0.995, foam tortuosity of 1.0059, thermal characteristic length of 470 μm, viscous characteristic length of 240 μm, and flow resistivity of 9000 [Pa·s/m^2]. Moreover, to find a suitable foam thickness, this thesis conducted acoustic simulations with COMSOL Multiphysics. Then, in the setting of the poroacoustics section, Johnson-Champoux-Allard model is chosen for calculating the effect of the melamine sponge. As a consequence, after adding two layers of melamine sponges with a thickness of 4 mm [Fig. 3.8(b)], the metasurface realized an improved sound absorption performance having an ultra-high absorption coefficient (averaged value of 0.975) in the working range of 920-3190 Hz [Fig. 3.8(b)].

3.4 Broadband sound absorption with acoustic metasurfaces approximating the causality constraint of the minimal thicknesses

As demonstrated above, it is ideal for achieving a high-efficiency sound absorber to exert powerfully the coherent coupling among the components, which essentially requires that the coupled metasurfaces should have high degrees of freedom of impedance modulation. An effective approach to achieve this target is to employ a large number of components that support multiple resonances and excellent adjustability. In the following, the thesis will present a coupled metasurface consisting of 36 cascade neck-embedded Helmholtz-resonator (CNEHRs), which not only offers better modulation of coupling but also provide the over-damped condition as well as the decreased excessive response to enable the coupled metasurface to approach the causality-governed minimal thickness [53].

The concept of the complex frequency plane had been demonstrated in the former section, and in this section, the properties of the locations of the zeros and poles are further discussed. Usually when considering the thermal and viscous losses of a system, the effects are introduced into the sound speed and the wave number, but mathematically, it is also possible to introduce the losses into the frequency. The complex frequency plane artificially introduces an imaginary part of the frequency, and in this case, the imaginary part of the frequency indicates the gain or loss of the system.

If the function analyzed on the complex frequency plane is the reflection coefficient, ln(r'), the under-damped structure will produce the zeros and poles in the upper-half plane and lower-half plane, respectively. On the other hand, for an over-damped structure, the zeros will shift to the lower-half plane but the poles will be still in the lower-half plane. Therefore, to avoid the singularity of integration caused by the poles on a complex frequency plane, the upper-half plane can be chosen to make the integration. According to the relation between frequency and wavelength, the locations of poles and zeros are opposite compared to the complex frequency plane, and thus the integration can be perforated in lower-half plane to avoid the singularity caused by the poles (see Fig. 3.9(a)).

The logarithm form of the reflection coefficient (ln($\widetilde{r'}$)) is employed as a response function in the complex wavelength plane (see Fig. 3.9(a)). To obtain a conservation relationship, the integration route is set to be a half round with an infinite radius in the lower-half plane. Then, according to the Cauchy 's theorem, the result of the loop integral of the analytical function is 0. Based on this and through some derivations on the basis of the causality feature of the system, the relation between the thickness of the sound absorber and the acoustic response in the full frequency range can be expressed as [56]

$$L \geq \frac{1}{4\pi^2\phi}\left|\int_0^{\infty} \ln\left|1 - A(\lambda')\right| \mathrm{d}\lambda'\right| = L_{\min}, \tag{3.19}$$

where $\phi = V_{\mathrm{air}}/V_0$ represents the volume fraction of the sound absorber, λ' is the wavelength, $L_{\min}$ is the minimal thickness governed by the causality constraint. $A(\lambda')$ indicates the absorption coefficients, which can be expressed by the defined acoustic response (ln($\widetilde{r'}$)). Equation (3.19) shows that the absorber's minimal thickness is relevant to $A(\lambda')$. For a certain $A(\lambda')$, there exists the minimal thickness when $L = L_{\min}$.

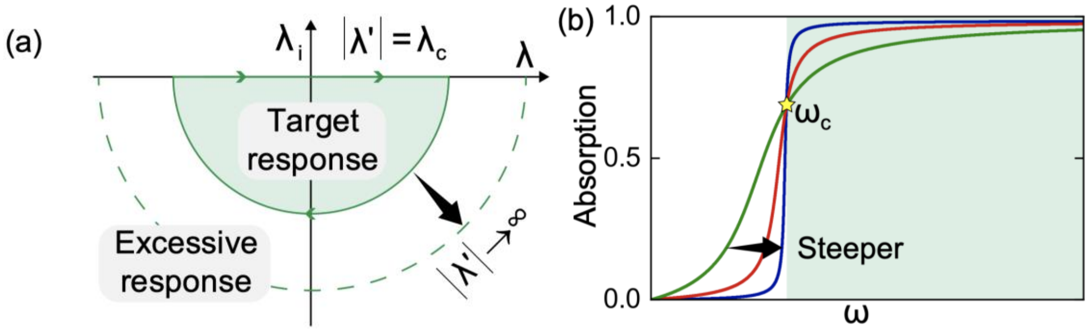

Figure 3.9 Illustration of the causality constraint.

(a) Illustration based on a complex wavelength plane of the materials' acoustic response. Here the acoustic response is set to $\ln(\widetilde{r'})$, where r' indicate the reflection coefficient. The target response and the excessive response are corresponding to the marked domains illustrated in (b). The semicircle with a radius of $|\lambda'|$ indicates the contour of integral for the derived causality constraint. The causality constraint is derived at the static limit ($|\lambda'| \to \infty$) involving the excessive response. (b) Absorption curves for three different response functions. The green, red and blue curves demonstrate that a sound-absorbing material with a unanimous $L_{\min}$ of 100 mm but with the increasingly slope curves of acoustic responses (represented from [53]).

Furthermore, the investigation found that the minimal thickness does not mean the most desired sound absorption performance. Generally, sound absorbers are expected to have the best possible sound absorption in a target frequency band, but the minimal thickness actually contributed by the acoustic responses over the full frequency range. For instance, the three sound absorbers are all achieve the same minimal thickness of 100 millimeters but show different absorption curves (see Fig. 3.9(b)). Suggest that in practical application, it is anticipated to obtain good absorption performance within the target frequency range marked in the green shadow, but it can be observed that the absorption efficiency within the target frequency range will decrease with the increase of absorption outside the target frequency range. Based on this result, the acoustic response outside the target band is defined as a redundant acoustic response, which should be suppressed in many practical designs.

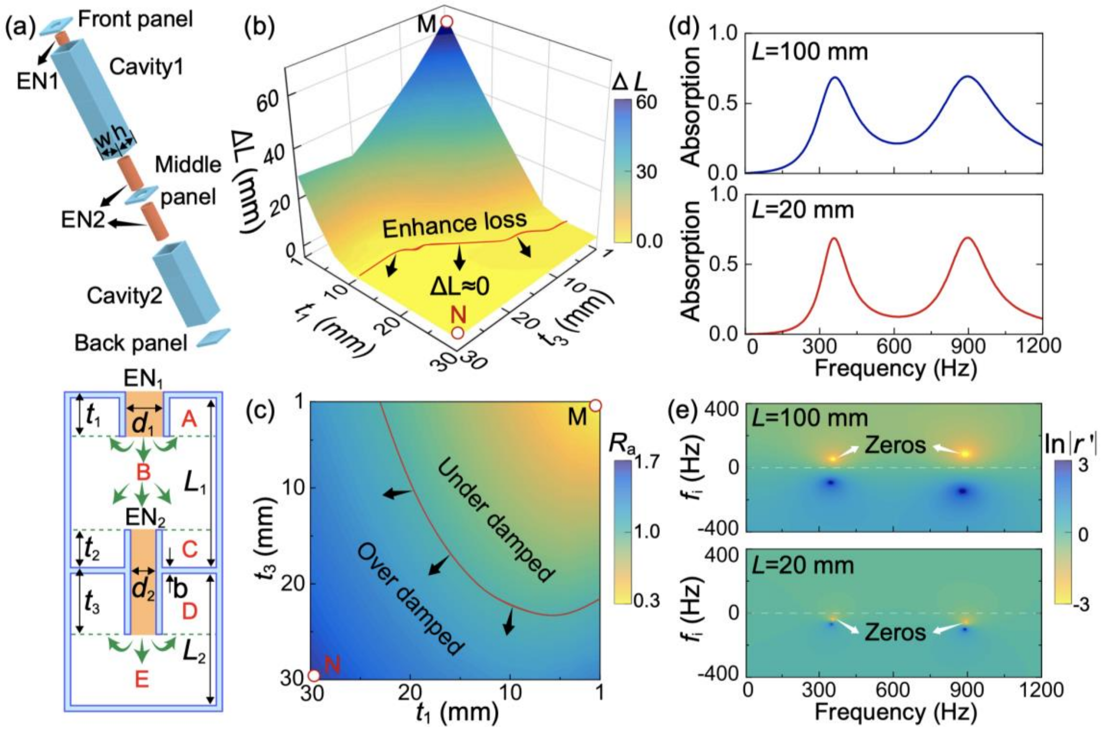

Figure 3.10 Demonstration of the over-damped condition for the achievement of the optimal thickness.

(a) Cascade neck-embedded Helmholtz-resonator (CNEHR). (b) Variation of the Redundant structural thickness ($\Delta L = |L - L_{\min}|$). The red curve indicates $\Delta L = 0$. (c) R_a at fundamental resonant frequency. The red curve indicates $R_a = 1$. (d) Absorption curves of two CNEHRs having thicknesses of 100 mm and 20 mm, respectively. (e) Reflection property of the two structure in (d) based on a complex frequency plane [53].

Further, cascade neck-embedded Helmholtz-resonators (CNEHRs) are presented as the components of the coupled sound-absorbing metasurface [Fig. 3.10(a)]. Compared with the NEHRs, the CNEHRs can obtain more resonance modes. To demonstrate the physics behind Eq. (3.19), redundant thickness is defined as $\Delta L = |L - L_{\min}|$. For instance, by using *Zn* of a CNEHR (deduced later) and substituting them into Eq. (3.19), the variation of ΔL along with the tuning of t_1 and t_3 can be illustrated [Fig. 3.10(b)]. When $\Delta L > 0$ at point M ($t_1 = t_2 = 1$ mm), the system is non-optimal. As t_1 and t_3 increase, ΔL reduces and eventually goes to point N inside the region with $\Delta L \approx 0$. At the same time, the CNEHR changed from an under-damped condition (R_a =0.3) to an over-damped condition (R_a =1.7) [Fig. 3.10(c)]. To better demonstrate the importance of the over-damped condition in realizing the minimal thickness, a CNEHR with the thicknesses of 100 mm (under-damped) and another CNEHR with the thicknesses of 20 mm (over-damped) are investigated. Their absorption coefficients are illustrated in Fig. 3.10(d). It is found that the two CNEHRs exhibit nearly similar absorption curves but the latter design has a significantly thinner structure. In fact, their acoustic responses are distinct on the complex frequency plane [Fig. 3.10(e)], where the under-damped condition leads to a deduction of

$$L = L_{\min} - \frac{1}{2\pi\phi}\sum_{n}\mathrm{Im}(\lambda_n), \tag{3.20}$$

where λ_n indicates the locations of zeros of $\ln|r'|$ on the lower-half complex wavelength plane. Equations (3.19)-(3.20) demonstrate that there is a minimum thickness for sound absorbers, which intrinsically depends on the reflection coefficient, and the over-damped condition is revealed to be the requirement to achieve the minimal thickness.

From the results above, it is found that for realizing broadband near-perfect absorption with the optimal thickness, two essential guidelines can be deduced: he reduced excessive response and the over-damped condition. In what follows, this thesis will demonstrate that by coupling a large number of components for an intensive mode density, the excessive response can be effectively suppressed. Furthermore, the employment of a large number of component metasurfaces can also provide intensive non-local coupling, which is important for the suppression of the absorption dips caused by antiresonances.

As a proof-of-concept design 36 CNEHRs are used to construct the sound-absorbing metasurfaces [Fig. 3.11(a)]. The employment of such a large number of double-layer resonators is to support high density of resonances, which is proved to be an effective pathway to suppress the redundant acoustic responses as well as the absorption dips induced by antiresonances. Here the size of the metasurface's cross-section is at a subwavelength level in the investigated frequency range, so that the metasurface's surface acoustic impedance can be calculated according to Eq. (3.14). The surface acoustic impedance of the individual CNEHRs will be shown later.

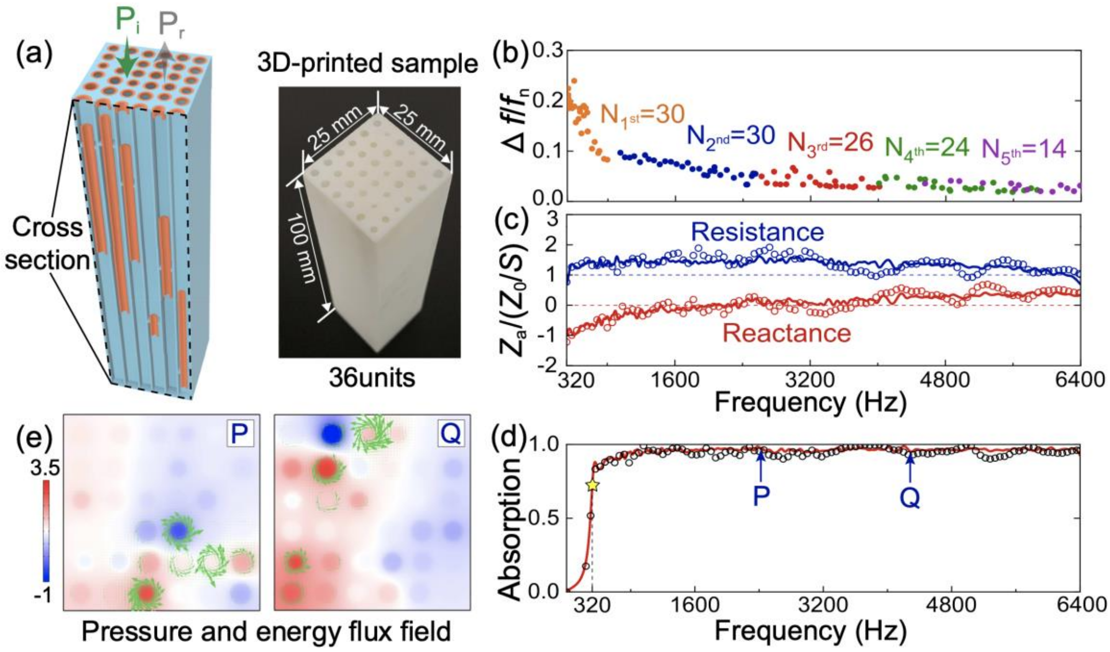

Figure 3.11 Broadband sound absorber approaching the optimal thickness.

(a) Coupled sound-absorbing metasurface composed of 36 CNEHRs. (b) Theoretical bandwidth of the resonant modes. The sequence of numbers from 1st to 5th denotes the orders of resonance modes. (c) Lines and circles represent the analytical and experimental results of acoustic resistance and acoustic reactance of the coupled metasurface-based sound absorber. (d) Lines and circles indicate the theoretical and experimental results of absorption coefficients of the sound absorber. (e) Pressure fields(indicated by color) and energy fluxes (green arrows) above the metasurfaces of 0.1 mm, corresponding to the two frequencies (P-2430 Hz and Q-4300 Hz) in (e) [53].

Figure 3.11(b) clearly shows that intensive mode density is realized within the range of 320-6400 Hz. Based on the significantly suppressed antiresonances owing to the intensive mode density, the acoustic impedance of the coupled metasurface shows improved performance in terms of the greatly attenuated dispersion than the previous work [30, 56] (see Fig. 3.11(c)). Consequently, broadband high-efficiency sound absorption is realized both theoretically and experimentally approximately achieving the minimal thickness of 100 mm, which meanwhile exhibits an average absorption coefficient of 0.93 within 320-6400 Hz [Fig. 3.11(d)]. The flat absorption curve validates the suppression of antiresonance-induced absorption dips. Besides, to intuitively illustrate the strong non-local effect of coupled metasurface, the near sound field of the metasurface is shown by the simulation with COMSOL Multiphysics. Figure 3.11(e) illustrates the sound pressure and energy flux fields at the resonance and antiresonance (marked as P and Q in Fig. 3.11(d)).

At last, the theoretical model for the surface acoustic impedance of the CNEHRs is presented. For the CNEHRs, the lumped-parameter impedance models are not valid in the relatively higher frequency ranges. Hence, the transfer matrix method (TMM) is employed for the analysis of the CNEHRs' surface acoustic impedance. Then, according to the acoustic continuity requirement, the transfer matrix at different positions inside the CNEHR can be expressed as

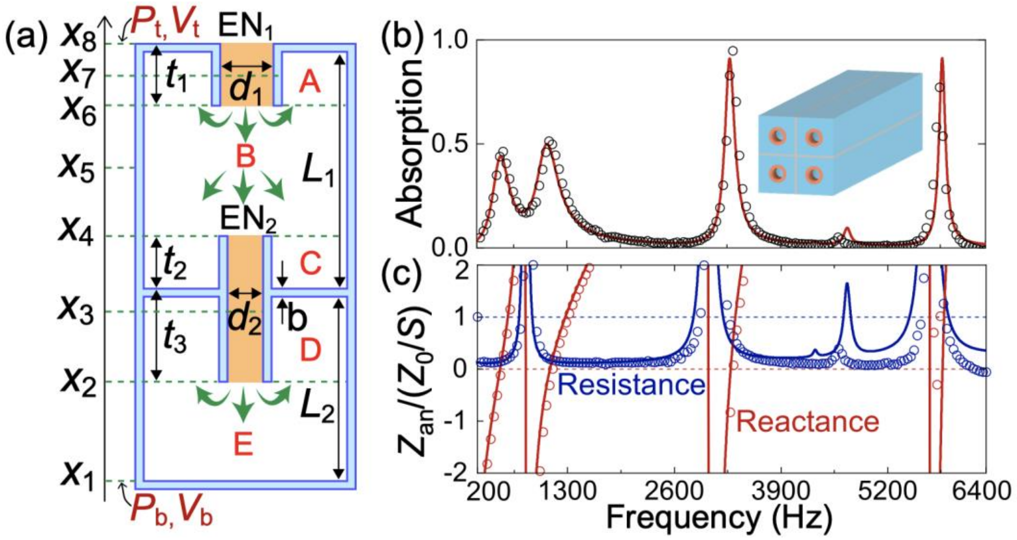

Figure 3.12 Impedance model of a CNEHR.

(a) Schematic. (b) Experimentally measured (circles) and theoretically calculated (lines) and absorption curves for the CNEHR component. (c) Theoretically calculated (lines) and experimentally measured (circles) results for the CNEHR component [53].

$$\begin{pmatrix} P_{\mathrm{x}_i} \\ V_{\mathrm{x}_i} \end{pmatrix} = \mathrm{M}_{\mathrm{x}_i} \begin{pmatrix} P_{\mathrm{x}_{i\text{-}1}} \\ V_{\mathrm{x}_{i\text{-}1}} \end{pmatrix}, \qquad \textbf{(3.21)}$$

where the different number of *i* (8, 7, 6, 5, 4, 3, 2) denots $\mathrm{M}_{\mathrm{x}_\mathrm{i}}$, $P_{\mathrm{x}_\mathrm{i}}$, $V_{\mathrm{x}_\mathrm{i}}$, and $V_{\mathrm{x}_{\mathrm{i}\text{-}1}}$ at *x*8-*x*1. At the upper opening of EN1 (*x*8), the transfer matrix representing the end correction from high-order evanescent waves and surface resistance can be expressed as

$$\mathrm{M}_{\mathrm{EN}_1,\mathrm{UP}} = \begin{pmatrix} 1 & \mathrm{j}k_0 \ \ \delta_1\text{-}\mathrm{j}\sqrt{2\eta/(\omega\rho_0)} \ \ Z_0 \ /S_{\mathrm{EN}_1} \\ 0 & 1 \end{pmatrix}, \qquad \textbf{(3.22)}$$

where S_{EN_1} is the cross-section of EN1. Inside the channel of EN1 (*x*7), the transfer matrix is

$$\mathrm{M}_{\mathrm{EN}_1} = \begin{pmatrix} \cos(k_{\mathrm{EN}_1} t_1) & \mathrm{j}\sin(k_{\mathrm{EN}_1} t_1) Z_{\mathrm{EN}_1} \ / \ S_{\mathrm{EN}_1} \\ \mathrm{j}\sin(k_{\mathrm{EN}_1} t_1) S_{\mathrm{EN}_1} \ / Z_{\mathrm{EN}_1} & \cos(k_{\mathrm{EN}_1} t_1) \end{pmatrix}, \qquad \textbf{(3.23)}$$

where k_{EN_1} and $Z_{\mathrm{EN}_1} = \rho_{\mathrm{EN}_1} c_{\mathrm{EN}_1}$ represent the effective wavenumber and the effective characteristic acoustic impedance of air inside EN1. At the lower port of EN1 (*x*6), the region A around EN1 splits the wave into two flows, where the boundary conditions can be expressed as $P_{x_7} = P_{x_6} = P_{\mathrm{A}}, V_{x_7} = V_{x_6} + V_{\mathrm{A}}$ and $P_{\mathrm{A}} / V_{\mathrm{A}} = -\mathrm{j}\cot[k_{\mathrm{A}}(t_1 - b)] Z_{\mathrm{A}} / S_{\mathrm{A}}$. Considering the end correction of acoustic impedance and the boundary conditions, it can be deduced that

$$\begin{pmatrix} P_{x_7} \\ V_{x_7} \end{pmatrix} = \mathrm{M}_{\mathrm{EN_1,DW}} \begin{pmatrix} P_{x_6} \\ V_{x_6} \end{pmatrix}, \tag{3.24}$$

where

$$\begin{aligned} \mathrm{M}_{\mathrm{EN_1,DW}} = & \begin{pmatrix} 1 & \mathrm{j}k\ \delta_2\text{-}\mathrm{j}\sqrt{2\eta / (\omega\rho_0)}\ Z_0 / S_{\mathrm{EN_1}} \\ 0 & 1 \end{pmatrix} \\ & \times \begin{pmatrix} 1 & 0 \\ \mathrm{j}\tan[k_{\mathrm{A}}(t_1 - b)] S_{\mathrm{A}} / Z_{\mathrm{A}} & 1 \end{pmatrix}, \end{aligned} \tag{3.25}$$

where k_{A} and $Z_{\mathrm{A}} = \rho_{\mathrm{A}} c_{\mathrm{A}}$ represent the effective wavenumber and the effective characteristic acoustic impedance of air in region A. Then, the transfer matrix in the region B (x_5) is

$$\begin{aligned} & \mathrm{M_B} = \\ & \begin{pmatrix} \cos[k_{\mathrm{B}}(L_1 - t_1 - t_2 + b)] & \mathrm{j}\sin[k_{\mathrm{B}}(L_1 - t_1 - t_2 + b)] Z_{\mathrm{B}} / S_{\mathrm{B}} \\ \mathrm{j}\sin[k_{\mathrm{B}}(L_1 - t_1 - t_2 + b)] S_{\mathrm{B}} / Z_{\mathrm{B}} & \cos[k_{\mathrm{B}}(L_1 - t_1 - t_2 + b)] \end{pmatrix}, \end{aligned} \tag{3.26}$$

where k_B and $Z_{\mathrm{B}} = \rho_{\mathrm{B}} c_{\mathrm{B}}$ represent the effective wavenumber and the effective characteristic acoustic impedance of air inside region B, and $S_{\mathrm{B}} = wh$ is the cross-section of region B. Similarly, the transfer matrix at x_4, inside EN2 (x_3), at x_2, and inside region E (x_1) are:

$$\mathrm{M}_{\mathrm{EN_2,UP}} = \begin{pmatrix} 1 & 0 \\ \mathrm{j}\tan(k_{\mathrm{C}} t_2) S_{\mathrm{C}}\ / Z_{\mathrm{C}} & 1 \end{pmatrix} \begin{pmatrix} 1 & \mathrm{j}k\ \delta_3\text{-}\mathrm{j}\sqrt{2\eta / (\omega\rho_0)}\ Z_0 / S_{\mathrm{EN_2}} \\ 0 & 1 \end{pmatrix}, \tag{3.27}$$

where k_{C} and $Z_{\mathrm{C}} = \rho_{\mathrm{C}} c_{\mathrm{C}}$ represent the effective wavenumber and the effective characteristic acoustic impedance of air in region C, δ_3 is the end correction of EN2 relative to the cavity, $S_{\mathrm{C}} = wh - \pi(d_2 / 2 + b)^2$ and $S_{\mathrm{EN_2}}$ are the cross-sections of regions C and EN2;

$$\mathrm{M}_{\mathrm{EN}_2}=\begin{pmatrix} \cos[k_{\mathrm{EN}_2}(t_2+t_3)] & \mathrm{j}\sin[k_{\mathrm{EN}_2}(t_2+t_3)]Z_{\mathrm{EN}_2}/S_{\mathrm{EN}_2} \\ \mathrm{j}\sin[k_{\mathrm{EN}_2}(t_2+t_3)]S_{\mathrm{EN}_2}\ /\ Z_{\mathrm{EN}_2} & \cos[k_{\mathrm{EN}_2}(t_2+t_3)] \end{pmatrix}, \tag{3.28}$$

where k_{EN_2} and $Z_{\mathrm{EN}_2}=\rho_{\mathrm{EN}_2}c_{\mathrm{EN}_2}$ represent the effective wavenumber and the effective characteristic acoustic impedance of air inside EN2, and S_{EN_2} is the cross-sectional area of EN2;

$$\begin{aligned}\mathrm{M}_{\mathrm{EN}_2,\mathrm{DW}}=&\begin{pmatrix} 1 & \mathrm{j}k\ \ \delta_3\text{-}\mathrm{j}\sqrt{2\eta\ /\ (\omega\rho_0)}\ \ Z_0\ /\ S_{\mathrm{EN}_2} \\ 0 & 1 \end{pmatrix} \\ &\times\begin{pmatrix} 1 & 0 \\ \mathrm{j}\tan[k_{\mathrm{D}}(t_3-b)]S_{\mathrm{D}}\ /\ Z_{\mathrm{D}} & 1 \end{pmatrix},\end{aligned} \tag{3.29}$$

where k_{D} and $Z_{\mathrm{D}}=\rho_{\mathrm{D}}c_{\mathrm{D}}$ represent the effective wavenumber and the effective characteristic acoustic impedance of air in region D, and $S_{\mathrm{D}}=S_{\mathrm{C}}$ is the cross-section of region D;

$$\mathrm{M}_{\mathrm{E}}=\begin{pmatrix} \cos[k_{\mathrm{E}}(L_2-t_3+b)] & \mathrm{j}\sin[k_{\mathrm{E}}(L_2-t_3+b)]Z_{\mathrm{E}}\ /\ S_{\mathrm{E}} \\ \mathrm{j}\sin[k_{\mathrm{E}}(L_2-t_3+b)]S_{\mathrm{E}}/Z_{\mathrm{E}} & \cos[k_{\mathrm{E}}(L_2-t_3+b)] \end{pmatrix}, \tag{3.30}$$

where k_{E} and $Z_{\mathrm{E}}=\rho_{\mathrm{E}}c_{\mathrm{E}}$ are the complex wave number and complex characteristic impedance of air in region E, and $S_{\mathrm{E}}=S_{\mathrm{B}}$ is the cross-sectional area of region E. Then the total transfer matrix T can be expressed as:

$$\begin{aligned}\mathrm{T}=\begin{pmatrix} \mathrm{T}_1 & \mathrm{T}_2 \\ \mathrm{T}_3 & \mathrm{T}_4 \end{pmatrix}=&\ \mathrm{M}_{\mathrm{EN}_1,\mathrm{UP}}\times\mathrm{M}_{\mathrm{EN}_1}\times\mathrm{M}_{\mathrm{EN}_1,\mathrm{DW}}\times\mathrm{M}_{\mathrm{B}} \\ &\times\mathrm{M}_{\mathrm{EN}_2,\mathrm{UP}}\times\mathrm{M}_{\mathrm{EN}_2}\times\mathrm{M}_{\mathrm{EN}_2,\mathrm{DW}}\times\mathrm{M}_{\mathrm{E}}.\end{aligned} \tag{3.31}$$

Then it gives

$$\begin{pmatrix} P_{\mathrm{t}} \\ V_{\mathrm{t}} \end{pmatrix}=\mathrm{T}\begin{pmatrix} P_{\mathrm{b}} \\ V_{\mathrm{b}} \end{pmatrix}, \tag{3.32}$$

where the surface acoustic impedance is $Z_n = P_t/V_t$. By combining the boundary condition $V_b = 0$ (hard boundary) in Eqs. (3.31)-(3.32), the surface impedance of the CNEHR is expressed as $Z_n=P_{\mathrm{t}}/V_{\mathrm{t}}=\mathrm{T}_1/\mathrm{T}_3$.

A CNEHR is fabricated with the geometric parameters t_1 = 5 mm, t_2 = 20 mm, t_3 = 15 mm, d_1 = 3.9 mm, d_2 = 4.8 mm, h = 10 mm, w = 10 mm, L_1 = 60 mm, L_2 = 40 mm, and b = 1.5 mm. The inset figure in Fig. 3.12(b) shows the assembly of four identical CNEHRs. It can be observed from Figs. 3.12(b)-(c) that the measured results exhibit good accordance with the theoretical results.

To summarize, aiming for broadband sound absorption via ultrathin structures, this section provides the concepts of coupling imperfect components, satisfying the over-damped condition and reducing excessive responses by theoretically and experimentally investigating the coherent coupling among multiple component metasurfaces and the nature of acoustic responses of acoustic systems. As proof-of-concept demonstrations, several coupled metasurfaces are presented (detailed geometric parameters in references [25] and [53]), which successfully achieve high-efficiency broadband absorption and exhibit ultra-thin structure approaching the minimal thickness governed by the called causality constraint. In fact, these concepts essentially provide an efficient pathway for the modulation of the surface acoustic impedance in a broad frequency band, not just for air-matched impedance demanded by high-efficiency acoustic absorption. Inspired by the results in Chapters 2-3, many interesting and high-performance acoustic devices relevant to noise control engineering and impedance engineering can be developed, which will be demonstrated in the following chapter.

4. Chapter 4: Acoustic Devices Inspired by the Sound-absorbing Metasurfaces

The sound absorption based on acoustic metasurfaces investigated above fundamentally provides effective techniques to modulate the acoustic impedance of the structures. Therefore, these results and findings facilitate the development of high-performance acoustic devices in noise control engineering and impedance engineering. Based on the findings demonstrated above, this thesis further investigates the broadband metaliner under grazing flow, the extreme asymmetric sound absorber, the extreme narrow-band perfect sound trapper/absorber, and the sound-emission amplifier.

4.1 Broadband sound attenuation with metasurface-based acoustic liner in flow ducts

Acoustic liners are the extensively used passive acoustic devices for reducing duct-noise, which can find wide implementations in propulsion systems of airplanes and other engineering systems with noise in ducts. However, conventional acoustic liners usually exhibit sound-attenuation in narrow frequency band and relatively large structural sizes when it comes to low frequency noise [5, 49, 68-72]. In pursuit of broadband sound attenuation via an ultra-thin structure, this section presents an acoustic metaliner that takes advantage of the exceptional impedance adjustability of broadband sound-absorbing metasurfaces.

As shown in Fig. 4.1(a), the metaliner is composed of two elements, a metasurface composed of the NEHRs [40] and a perforated plate having an air gap from the NEHRs. The metasurface enables the target acoustic impedance within a broad frequency band as well as the deep subwavelength size. Besides, the perforated plate helps to make the flow near the metaliner smoother. With grazing flows, the metaliner’s acoustic impedance will be dependent on the speeds of the flows, which gives rise to a major challenge in tuning metaliner' impedance to fulfill the goal impedance, especially for the circumstances of modulations in broadband frequency ranges. To obtain the metaliners' acoustic impedance, the perforated plate is firstly analyzed. According to Guess's model [73], the semi-empirical equation of a perforated plate's acoustic impedance (Z_{P}) with the consideration of grazing flows reads

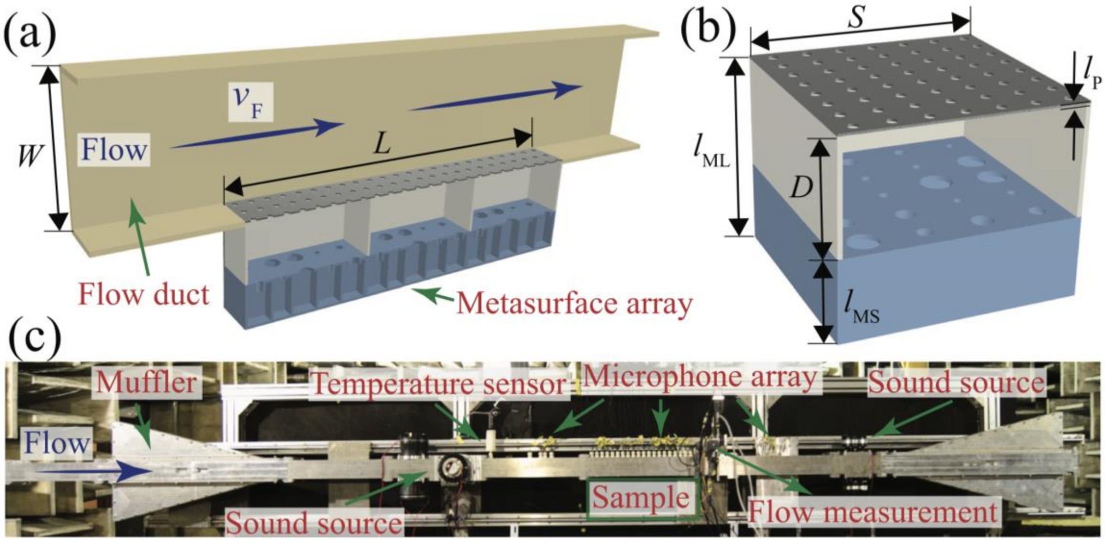

Figure 4.1 Illustration of the acoustic metaliner.
(a) A metaliner side-branched on one side of a flow duct (cut-open view). (b) The cell of the metaliner. The structure in blue is a NEHR array and the structure in gray is a perforated plate. There is an interlayer in the middle of the NEHR array and the perforated plate. (c) The aero-acoustic experimental setup [52].

$$Z_{\mathrm{P}} = Z_{\mathrm{P0}} + \frac{1-\sigma^2}{\sigma}\left(k\frac{v_{\mathrm{F}}}{c_0} + \frac{v_{\mathrm{S}}}{c_0}\right)z_0, \tag{4.1}$$

where v_{F} is the grazing flow' speed, and k = 0.3. v_{S} is the amplitude of the particle velocity of air within the holes of the perforated plate, which results from the nonlinear effect caused by high level of sound pressure. Z_{P0} is expressed as

$$Z_{\mathrm{P0}} = -\mathrm{j}\frac{\rho_0\omega(l_{\mathrm{P}} + \delta_{\mathrm{FS}})}{\sigma}\frac{J_0(\kappa d_{\mathrm{P}} / 2)}{J_2(\kappa d_{\mathrm{P}} / 2)}, \tag{4.2}$$

$$\delta_{\mathrm{FS}} = 0.85 d_{\mathrm{P}} \frac{(1-0.6\sqrt{\sigma})[1+5\times10^3(v_{\mathrm{S}} / c_0)^2]}{[1+305(v_{\mathrm{F}} / c_0)^3][1+10^4(v_{\mathrm{S}} / c_0)^2]}. \tag{4.3}$$

Here, it is noted that on the condition of $v_S/v_F < 0.15$, the high-pressure acoustic waves' effect could be neglected, and v_S should be changed to zero in Eq. (4.1). Besides, the NEHR array's acoustic impedance and the interlayer's effect can be calculated based on Eqs. (3.15)-(3.17).

To validate the theoretical results, experiments are performed [Fig. 4.1(c)]. The flow duct is with waveguide having a square cross-sectional area (side length 51 mm) [52]. For better demonstrating the metaliners' sound-attenuation performances and obtaining better examination of the experimental results of transmission losses, simulations are performed with COMSOL Multiphysics using the "Linearized Potential Flow" module.

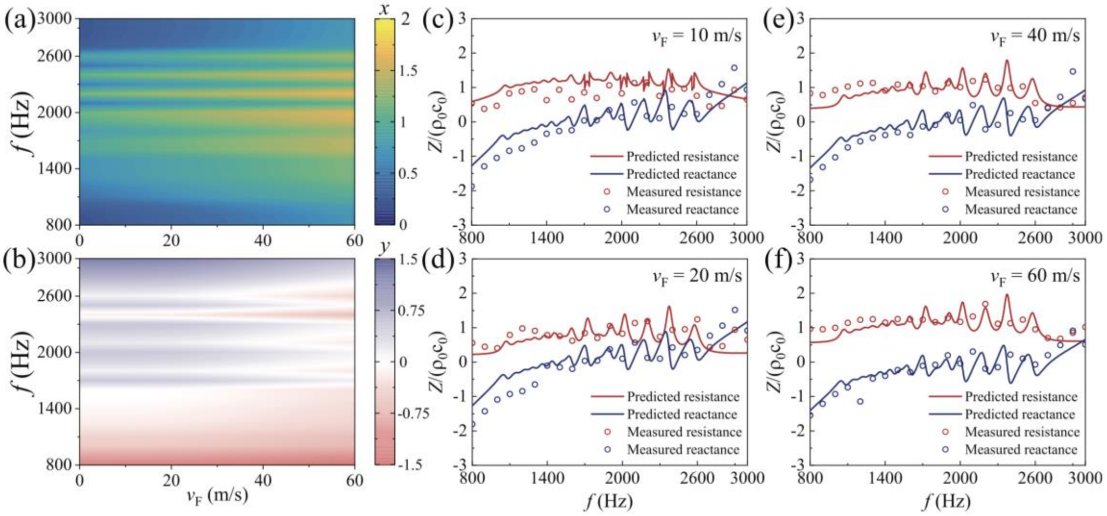

Figure 4.2 Impedance analysis of the presented metaliner.

The acoustic resistance (a) and acoustic reactance (b) of the presented metaliner with the variation of the speed of flows and the frequency. When having grazing flows at the speeds of 10 m/s (c), 20 m/s (d), 40 m/s (e), and 60 m/s (f), the metaliner's theoretical (lines) and experimental (circles) results of acoustic resistance (red) and acoustic reactance (blue). [52].

From Fig. 4.2, the calculated and measured results illustrate that the metaliner's acoustic resistance as well as acoustic reactance both show excellent insensitivity although v_F has changed from 0 m/s to 60 m/s. This result shows the remarkable tolerance of the changeable environments in practice. In addition, the acoustic impedance of the metaliner supports enhanced sound attenuation within the relatively higher frequency regime with the increase of flow speeds (shown later). This impedance condition is desired for extensive practical situations of exhaust mufflers as well as aero-engines where the spectrum of noise changes to higher frequencies when the in flow speed increases.

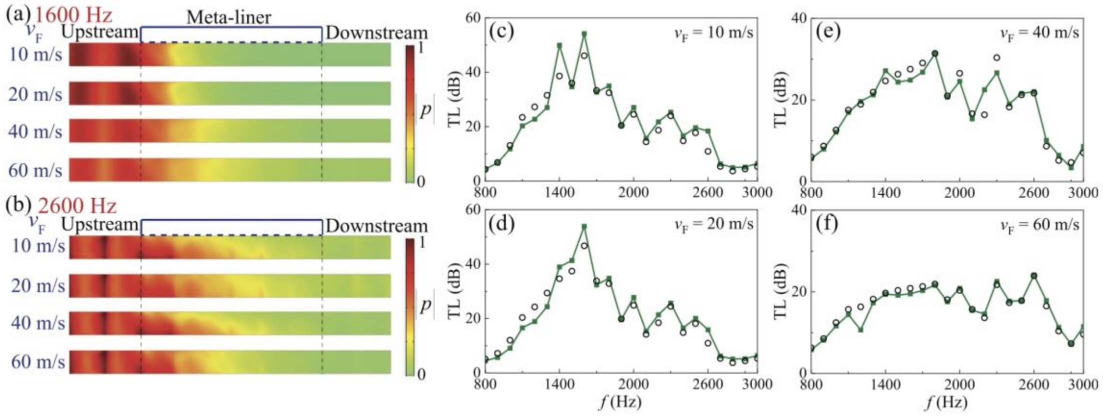

Figure 4.3 Attenuation performance of the presented metaliner.

(a)-(b) Distributions of sound pressure amplitudes $|p|$ of the metaliner facing different grazing flow speeds at 1600 and 2600 Hz. The simulation (green line) and experimental (black circles) results of transmission losses. The metaliner faces grazing flow at speeds of 10 m/s (c), 20m/s (d), 40 m/s (e), and 60m/s (f) [52].

Owing to the well-tuned acoustic impedance, the metaliner can achieve highly efficient as well as broadband sound attenuation. Figures 4.3(a)-(b) illustrate the distributions of simulation pressure amplitudes of the metaliner at 1600 and 2600 Hz. The simulations clearly show that the acoustic energy is dissipated intensively in the process of wave transmission near the metaliner. And the working performance at 2600Hz (the relatively high frequency) manifests an increasing trend with the increasing of flow speeds. At 1600 Hz (the relatively low frequency), the s working performance decreases but still maintains high efficiency as the flow speed increases. Figures 4.3(c)-(f) illustrate the results of transmission losses under the different speeds of grazing flow. Overall, the metaliner shows efficient sound-attenuation performances in a broad frequency band and sustains remarkably with the variation of flow speeds.

4.2 Compact asymmetric sound absorber with neck-embedded tubes

Asymmetric sound absorbers have aroused outstanding attention for its extensive potential applications and meaningful scientific values [22, 74-76]. Nevertheless, few previous investigations have bridged the physical mechanism of asymmetric acoustic absorption with the exceptional point [24, 77-81], and therefore an in-depth study on this would be interesting and valuable.

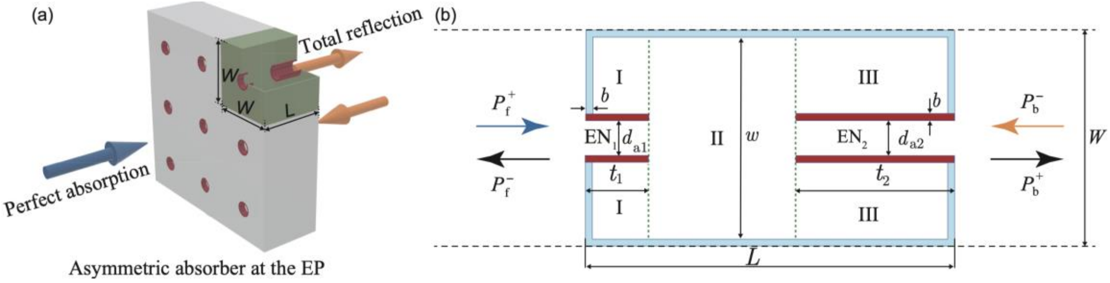

Figure 4.4 Illustration of the asymmetric sound absorber.
(a) A compact parallelly arranged coupled structure composed of a number of neck-embedded tubes (NETs). The cell structure of the array is marked by green color. (b) A 2D analytical model of a NET（split view). The NET can be theoretically portioned as three subsections (I, II, III) by two analyzing boundaries [82].

The presented asymmetric sound absorber is illustrated in Fig. 4.4(a), and unit neck-embedded tubes (NETs) is shown in Fig. 4.4(b). In Chapters 2-3, the embedded necks have been proved to be an excellent candidate to construct tunable and broadband absorbers with a compact structure, owing to the advantages in impedance manipulation as well as thickness reduction. Here, the NETs are proposed in a dual-port system for achieving extreme asymmetric sound absorption with a thin structure. When acoustic waves are of left incidence for the NET, highly efficient sound absorption occurs; In contrast, near-complete sound reflection occurs when the sound is incident from the right side of the NET, resulting in an extreme asymmetric absorption.

As illustrated in Fig. 4.4(b), a scattering matrix S_m can be used to describe the dual-port system [83]. Here, the forward (left) and backward (right) incident sound waves are indicated by P_f^+ and P_b^-, respectively. Besides, the corresponding output acoustic waves are indicated by P_f^- and P_b^+. Thus, scattering matrix S_m reads

$$\begin{Bmatrix} P_f^- \\ P_b^+ \end{Bmatrix} = \mathrm{S_m} \begin{Bmatrix} P_b^- \\ P_f^+ \end{Bmatrix}, \mathrm{S_m} = \begin{pmatrix} t & r_\mathrm{L} \\ r_\mathrm{R} & t \end{pmatrix}, \tag{4.4}$$

where t represents the sound transmission coefficient, and r_L and r_R are the sound reflection coefficients for the left incidence the right incidentce, respectively. The parameters in S_m can be calculated based on the TMM [82]. The eigenvalues of S_m can be expressed as $\lambda_\pm = t \pm \sqrt{r_L r_R}$.

The compact asymmetric sound absorber is illustrated in Fig. 4.5(a), where its cylindrical shape is for fitting the circular test tube. The experimental sample is produced by 3D-printing technology. The complex transmission and reflection coefficients are measured by employing a Bruel & Kjær type-4206T impedance tube and the accompanied equipment. In the experiments, sound waves are from the loudspeaker at the one of the ends of the tube, and the transmission coefficient as well as reflection coefficient are measured by the transfer-matrix approach [84]. As demonstrated in Figs. 4.5(b)-(c), the real as well as the imaginary parts of the scattering matrix's eigenvalues simultaneously turns into degenerate at 247.5 Hz, proving the presence of an EP. Such an EP-supporting system is highly sensitive to manufacturing errors, where the difference between simulation (calculation) and experimental results may due to the errors in manufacturing and the imperfect sealing during the measurements.

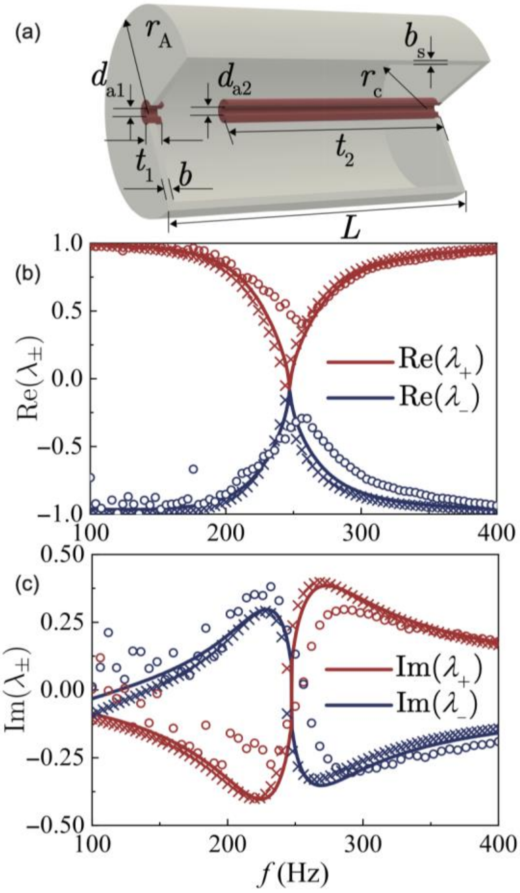

Figure 4.5 Eigenvalues analysis of the presented NET.
(a) Schematic of the experimental structure. Real part (b) and imaginary part (c) of $\lambda_\pm$. Experimental (circles), simulated (lines), and calculated (forks) results of the presented NET. The eigenvalues merge at 247.5 Hz (simulation), indicating the existence of an EP [82].

At the EP, extreme asymmetric absorption is witnessed. In the cases that sound is from the left incidence, the NET exhibits a trivial reflection ($|r_L|$ is 0.015, 0.095, and 0.122 for the simulation, the calculation, and the experiment, respectively) as well as a low transmission at the EP [Fig. 4.6(a)]. At the same time, for sound waves from the right incidence, nearly total reflection occurs [Fig. 4.6(b)]. Thus, the NET shows high-efficiency sound absorption for the left incidence (α_L achieves 0.994, 0.978, and 0.981

for the simulation, the calculation, and the experiment, respectively), and nearly complete reflection for sound waves from the right incidence, verifying the extreme asymmetric sound absorption at the EP [Fig. 4.6(c)]. To better demonstrate the occurrence of the asymmetric sound absorption, the distributions of sound pressures' amplitudes (|*p*|) from the simulations are shown in Figs. 4.6(d)-(e). When sound is incident from the left port, inside the NET, the acoustic intensity is largely enhanced, resulting in strong dissipation thanks to the high thermal and viscous losses inside the NET. In contrast, when sound is from the right incidence, most of the acoustic waves are reflected, rather than coming into the NET.

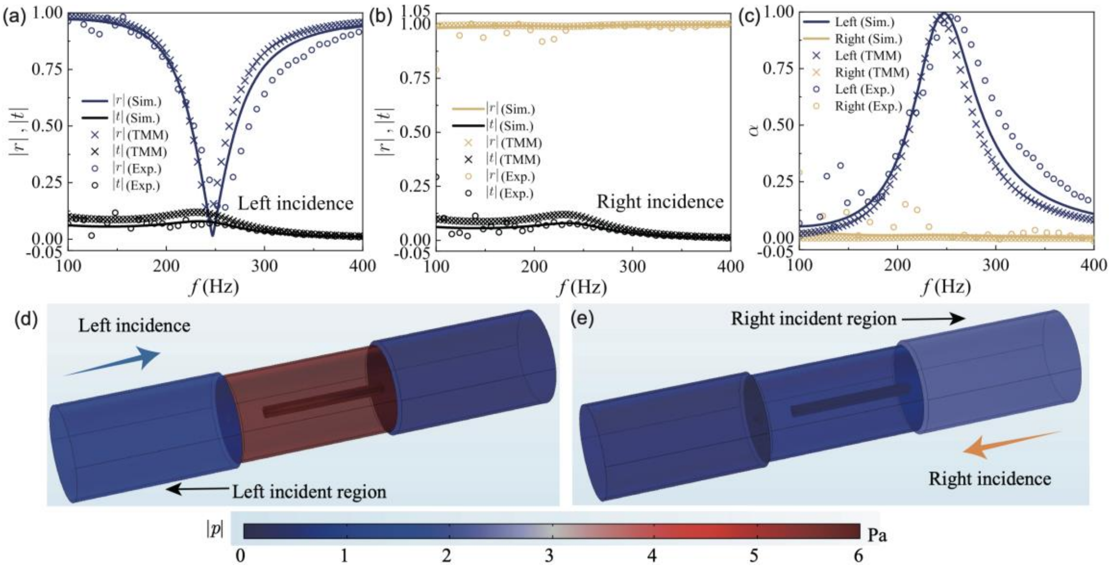

Figure 4.6 Performance of the presented NET.

Reflection coefficient and transmission coefficient of presented NET for (a) left sound-wave incidence and (b) right sound-wave incidence. Experimental, simulated, and calculated results are denoted by the circles, the lines, and the forks, respectively. (c) Absorption coefficients. Absolute sound pressure distribution for left sound-wave incidence (d) and right sound-wave incidence (e) at 247.5 Hz [82].

To summarize, this section presents an ultra-thin asymmetric absorber. Unlike the traditional side-branch asymmetric acoustic absorbers, the asymmetric absorber proposed here is designed with a structure coaxial with the waveguide. And more importantly, it is revealed that the extreme asymmetric absorption fundamentally occurs at the exceptional point, which may provide a pathway for developing acoustic devices with high sensitivity and demanded directivity.

4.3 Extreme sound confinement/absorption from a bound state in the continuum.

Confinement of incident sound is rather challenging since it requires reflection elimination to trap the sound waves and weak dissipation to store the trapped waves. In the perspective of sound absorption, extreme confinement can be considered to be perfect absorption achieved via a system with ultra-low thermal-viscous losses. These two requirements are quite counterintuitive and even conflicting for conventional sound absorbers, whereas this section will present a coupled system that supports a quasibound state in the continuum to overcome this conflict.

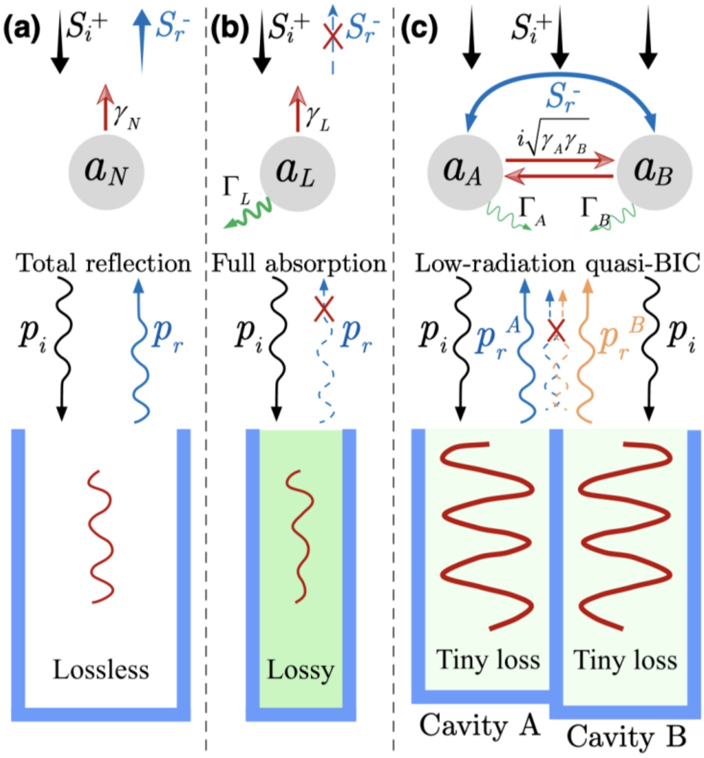

Figure 4.7 Sound confinement based on a quasiBIC.

(a) Total reflection for a cavity without thermal-viscous losses. p_i and p_r indicate the sound waves of incidence and reflection. (b) Zero reflection for a high-loss cavity, which is equal to normal sound absorber capable of perfect absorption. (c) extreme sound wave confinement induced by a Friedrich-Wintgen quasi-BIC-supporting system constructed by two coupled cavities with small thermal-viscous losses. The upper figures illustrate the corresponding analytical systems below. S_i^+ and S_r^- indicate the incident and the reflected sound waves. $\alpha_{N(L)}$ and $\gamma_{N(L)}$ indicate the amplitude of mode and the radiative decay rate of the system without (with) thermal-viscous losses. Γ_L represents the dissipative decay rate [85].

Bound states in the continuum (BICs) are totally confined having zero radiation but locate inside a continuous spectrum of radiating waves [86-91]. Acoustic BICs and quasiBICs, first explored in the 1960s [92-94], possess high Q factors [95-99] and meanwhile allow access to external radiation (for quasiBICs) [85, 100], which provides an efficient pathway for the construction of extreme sound confinement.

Two detuned cavities are presented to demonstrate the concept. First, for a lossless cavity facing incident acoustic waves, sound confinement cannot be achieved for the inevitable complete reflection [Fig. 4.7(a)]. The reflection can be reduced by adding thermal-viscous losses to the cavity [Fig. 4.7(b)]. However, it requires considerably large losses of the cavity to achieve total reflection elimination. As a result, the incident acoustic waves would be quickly dissipated instead of being confined inside the cavity. Therefore, extreme confinement of incident waves requires both eliminated reflection and tiny dissipation. For acoustic systems, it is challenging to achieve eliminated reflection via a structure possessing low dissipation.

This section solves this dilemma through presenting a two-cavity system having trivial thermal-viscous losses that supports a Friedrich-Wintgen quasi-BIC [Fig. 4.7(c)]. The quasi-BIC provides low radiation and allows the incident sound at a target frequency to be totally trapped inside the two-cavity system and survive the tiny thermal-viscous losses for a long time. Distinct from the previous understanding that massive thermal-viscous losses are necessary for realizing the zero reflection, here it is demonstrated that a quasi-BIC offers the possibility for arbitrarily low thermal-viscous losses to realize a reflectionless condition.

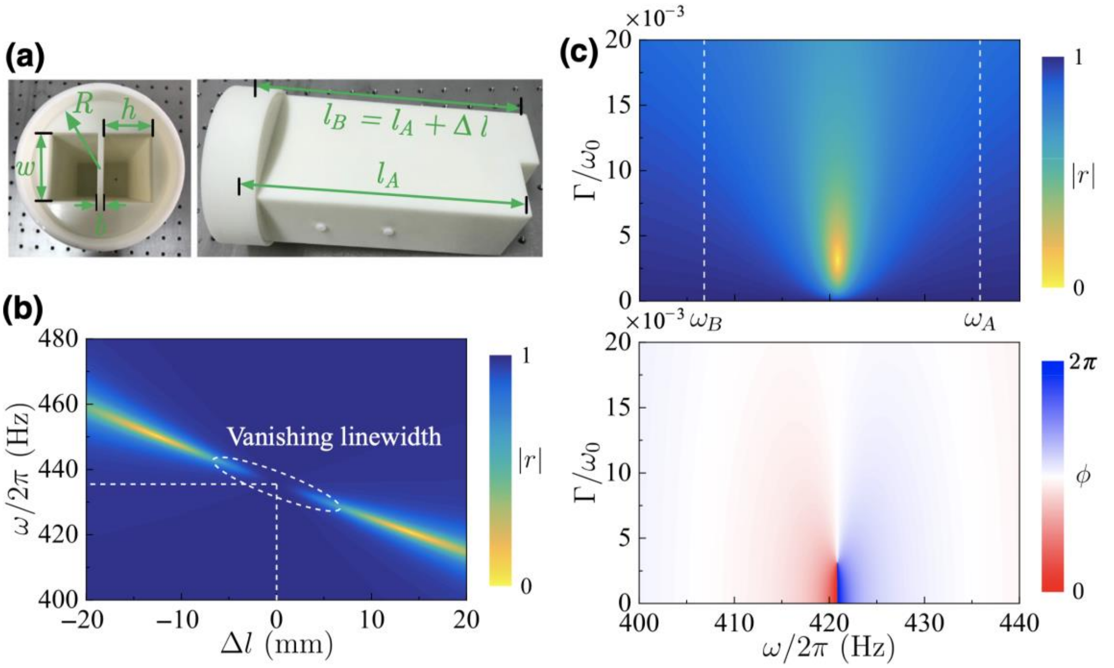

Figure 4.8 Acoustic quasi-BIC supported by a two-cavity system.
(a) Experimental structure with w = 38.5 mm, h = 54 mm, l_A = 180 mm. The wall thickness (b) is 4.5 mm. (b) Theoretical results of the reflection amplitude with the variations of the length difference between the two cavities, Δl, and the frequency, $\omega/(2\pi)$. (c) Theoretical results of the reflection amplitude (top figure) and phase (bottom figure) with the variations of the $\omega/2\pi$ and Γ/ω_0. The cavity B's length is 194 mm [85].

The practical design of the quasiBIC-supporting system is composed of two rectangular cavities with the same cross-sectional area but different lengths [Fig. 4.8(a)]. By employing the temporal coupled-mode equations for the lowest mode, the modes of cavities A and B ($\tilde{a}_{A(B)} = a_{A(B)}e^{i\omega t}$) read [74, 101, 102]

$$\frac{d}{dt}\tilde{a}_{\mathrm{A(B)}} = (i\omega_{\mathrm{A(B)}} - \gamma_{\mathrm{A(B)}} - \Gamma)\tilde{a}_{\mathrm{A(B)}} + i\sqrt{\gamma_{\mathrm{A(B)}}}(\tilde{S}_i^+ + i\sqrt{\gamma_{\mathrm{B(A)}}}\tilde{a}_{\mathrm{B(A)}}), \tag{4.5}$$

where S_i^+ and S_r^- represent the incident sound waves and the reflected sound waves, respectively. $\gamma_{\mathrm{A(B)}}$ denotes the radiative decay rate of cavity A(B). Γ indicates the dissipative decay rate of the two cavities. The sound reflection coefficient of the coupled two cavities, *r*, reads [74]

$$r = 1 + 2i\sqrt{\gamma_{\mathrm{A}}}\frac{a_{\mathrm{A}}}{S_i^+} + 2i\sqrt{\gamma_{\mathrm{B}}}\frac{a_{\mathrm{B}}}{S_i^+}. \tag{4.6}$$

Figure 4.8(b) illustrates the reflection amplitude based on Eqs. (4.6)-(4.7), with the length variation of cavity B (l_A = 180 mm). At Δl = 0 and 435.8 Hz, a vanishing linewidth occurs, indicating that the *Q* factor in in the vicinity of an infinite value [90, 99]. In this situation but without considering Γ, one of the system's eigenfrequencies will turn in to a purely real value corresponding to a BIC. Nevertheless, an ideal BIC is completely isolated and cannot access the outside fields. For achieving extreme confinement of incoming sound, a nonzero Δl is introduced and the BIC changes to a quasi-BIC. On this condition, the purely real eigenfrequency becomes complex with a small imaginary value represented by the radiative decay rate of the system, γ_s. When the dissipative decay rate (Γ_s) of the system is modulated to the identical value with γ_s, critical coupling [103] is achieved and the incident sound waves are completely trapped without any reflection. Distinct from critical coupling achieved for normal perfect absorbers, here the critical coupling is satisfied allowing a low radiative rate as well as a low dissipative decay rate. The reflectionless trapping is illustrated by Fig. 4.8(c), where a zero point appears.

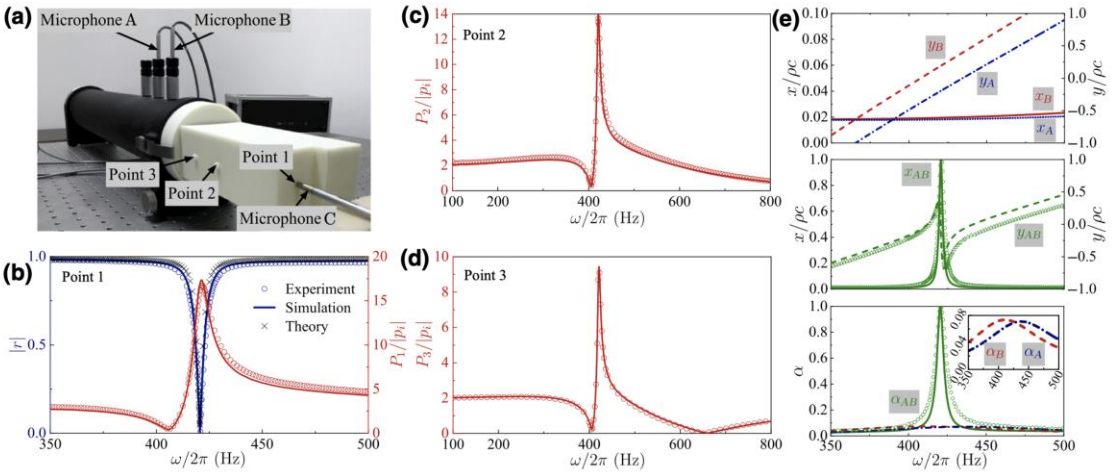

Figure 4.9 Experimental demonstration of the extreme confinement.

(a) Experimental setup. Point 1, point 2, and point3 are located at the positions 20 mm, 85 mm, and 130 mm above the inner bottom boundary of cavity A. (b) Reflection coefficient (blue) and pressure absolute amplification (red) at point 1. Circles, lines, and forks indicate the experimental, simulated, and calculated results, respectively. Pressure amplifications at point 2 (c) and point 3 (d). (e) Top picture: acoustic impedances. $x_{A(B)}$ and $y_{A(B)}$ indicate the acoustic resistance and acoustic resistance of cavity A(B). Middle picture: acoustic impedance of the two-cavity coupled system. Bottom picture: absorption coefficients of the two-cavity coupled system (in green), individual cavity A (in blue) and individual cavity B (in red) [85].

As shown in Fig. 4.9(a), experiments are conducted using a cylindrical Brüel and Kjær impedance tube having a diameter of 100 mm. By suitably tuning the length difference of the two cavities to form a quasi-BIC, total reflection elimination is allowed to be realized under a weak-dissipation condition. Figure 4.9(b) illustrates that a non-reflection ($|r| = 0$) point presents at 420.8 Hz. Besides, the reflection curve features a narrow frequency bandwidth, which indicates the high Q factor. Meanwhile, at the frequency witnessing the zero reflection, great sound pressure amplification of 24.5 dB is observed.

To validate the enhancement of sound field within the whole system, measurements are conducted at two other positions for obtaining the acoustic pressure amplitudes. The two testing positions are set to near the middle (point 2) and the top (point 3) of cavity A [Fig. 4.9(a)]. As illustrated in Figs. 4.9(c)-(d), the pressure amplitudes at the two positions realize 22.7 and 19.4 dB of enhancement. Besides, due to the fact that the quasi-BIC-induced zero reflection is can be also interpreted as a perfect absorption, the system's acoustic impedance is investigated to examine the sound scattering performances. For the individual cavities having tiny acoustic resistances, they can only provide very low absorption peaks. However, with the coherent coupling between the two detuned cavities, impedance matching can be realized, leading to a perfect absorption [Fig. 4.9(e)].

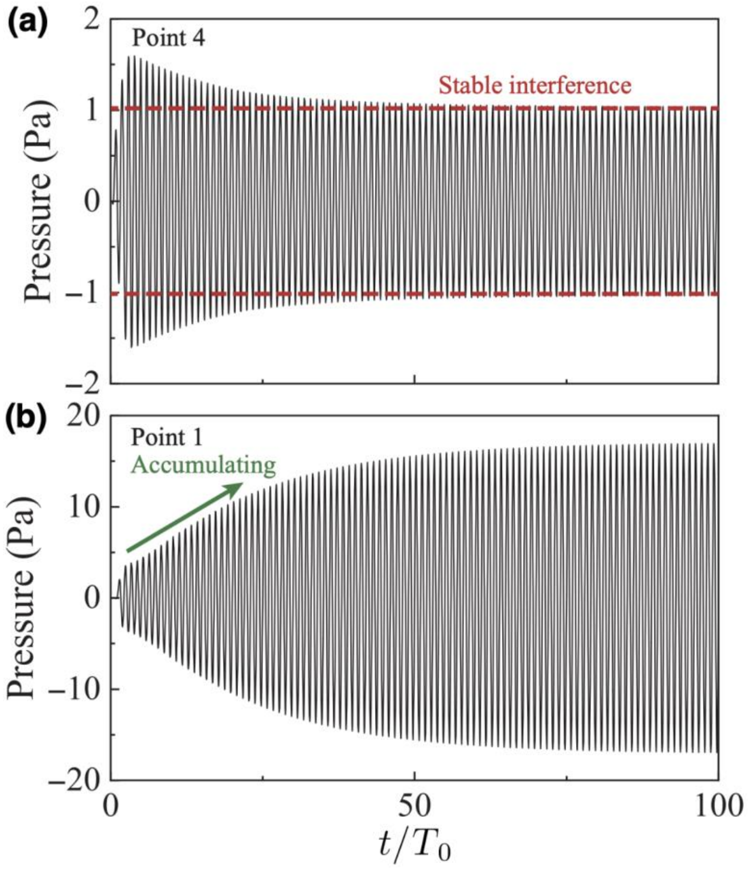

Figure 4.10 Time-domain simulation.

Fluctuations of acoustic waves' pressure at point 4 (a) and point 1 (b). Point 4 is set at 200 mm above the cavities' opening (see the supplementary materials in [85]). T_0 indicate the time period of the incoming sound [85].

Transient simulation is performed to demonstrate the wave properties in the process of developing the confined acoustic field. The simulation sets continuous incident plane waves of 1 Pa. The sound pressure variations of point 1 and point 4 (200 mm above the opening [85]) are obtained to evaluate wave properties the inside and outside the two coupled cavities. Figure 4.10(a) illustrates the instantaneous pressure variation at point 4, which experiences several periods of unstable fluctuations to realize a stable amplitude (1 Pa). Meanwhile, the sound pressure at point 1 gradually gains [Fig. 4.10(b)], indicating the sound confinement. For the coupled system, the thermal-viscous losses govern the maximum amplitude value of pressure at point 1. Theoretically, as the temporal coupled-mode theory and the impedance analysis predict, the presented two-cavity system can be constructed under arbitrarily low thermal-viscous losses, which has the potential to bring about arbitrarily long confinement lifetime.

4.4 Strong emission enhancement induced by quasibound states in the continuum.

The last section investigates the extreme sound confinement/absorption based on a two-cavity system that supports a Friedrich-Wintgen quasiBIC. With the continuous incident sound waves, the large sound-field enhancement can be achieved inside the two cavities. This section will demonstrate that based on this Friedrich-Wintgen quasiBIC-supporting system, strong acoustic Purcell effect (emission enhancement of sound sources) can be realized when the leakage and dissipation qualities of the system are well tuned.

The Purcell effect indicates that spontaneous radiation is not an inherent property of matter, whereas it is determined by the interaction of matter with its surrounding environment [78, 104-107]. Although this notion was first explored in quantum systems [108-110], it fundamentally reveals that the emission of sources can be modulated actively by engineering the surrounding environments, which has aroused broad interests in electromagnetic, elastic and acoustic wave systems. The acoustical counterpart of the Purcell effect in quantum emission has been proposed via Mie-like resonances [111] and Helmholtz resonances [112], and shown to be important for improving the low-frequency emission of loudspeakers and generating strong acoustic collimated waves. A major challenge in achieving strong acoustic Purcell effect is that realistic acoustic systems usually suffer from non-trivial dissipative (thermal-viscous) losses and exhibit considerably low quality factors (Q), which severely restricts the highest Purcell factor one may access.

In this study, a theoretical framework is established with the effects of radiative and dissipative losses being considered. The framework reveals that the acoustic Purcell factor is governed by the system's radiative and dissipative factors (Q_{leak}^{-1} and Q_{loss}^{-1}), and a critical condition that signifies the combinations of Q_{leak}^{-1} and Q_{loss}^{-1} can achieve the optimum Purcell factor values. To realize a large Purcell factor, the values of Q_{leak}^{-1} and Q_{loss}^{-1} should be simultaneously decreased. However, it is rather challenging and even conflicting in realistic acoustic resonant structures. This section subsequently demonstrates that this conflict can be well solved if the concept of quasiBIC-induced Purcell effect is introduced.

Firstly, a two-state system supporting a Friedrich-Wintgen quasiBIC together with its cavity-based practical implementation is presented. This system can offer tunable and low Q_{leak}^{-1} to approach the critical emission condition and therefore promote strong acoustic Purcell effect.

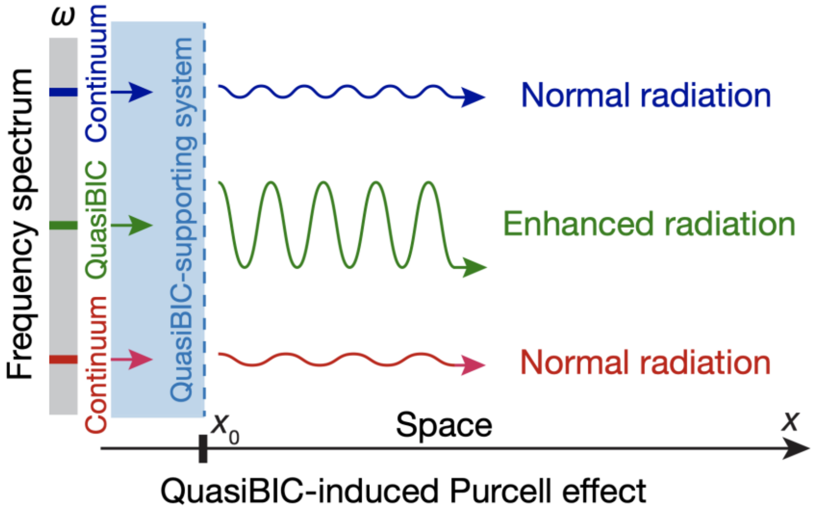

Figure 4.11 Concept of qusiBIC-induced acoustic Purcell effect.
In a quasiBIC-supporting system (light-blue domain) with a sound source inside, the emitted waves at the quasiBIC (green) will be greatly confined and lead to strong enhancement. The emitted waves in the continuum frequency spectrum (grey-shade, blue, red) will receive insignificant influence. x_0 marks the front surface of the system.

This section starts by introducing the concept of quasiBIC-induced acoustic Purcell effect [Fig. 4.11]. For quasiBIC-supporting systems with acoustic sources placed inside, the emitted waves in the continuum frequency spectrum will only receive trivial or negligible influence due to the systems' normal radiation rate, while the emitted waves at the quasiBIC will be greatly enhanced thanks to the strongly confined fields within the systems. Generally, a resonant mode of an open system can be characterized by the system's radiative and dissipative factors (Q_{leak}^{-1} and Q_{loss}^{-1}). Q_{leak}^{-1} and Q_{loss}^{-1} can describe the relations of the energy stored to the energy leaked and dissipated, respectively. Thus, it is ideal to construct a theoretical framework to interpret the mode-induced acoustic Purcell effect based on Q_{leak}^{-1} and Q_{loss}^{-1}.

As illustrated in Fig. 4.12(a), an acoustic resonant system constructed with an effective medium is firstly investigated. From the decomposed sound field and the connections to Q_{leak}^{-1} and Q_{loss}^{-1}, the link between the quality factors of a resonant mode and the peak acoustic Purcell factor can be obtained as

$$F_{\text{peak}}=1+\frac{2}{\pi Q_{\text{leak}}^{-1}}+2\sqrt{\frac{1}{\pi Q_{\text{leak}}^{-1}}+\frac{1}{(\pi Q_{\text{leak}}^{-1})^{2}}}, \tag{4.7}$$

$$\begin{aligned}F_{\text{peak}}=&\frac{Q_{\text{leak}}^{-1}}{Q_{\text{leak}}^{-1}+Q_{\text{loss}}^{-1}}+\frac{2Q_{\text{leak}}^{-1}}{\pi(Q_{\text{leak}}^{-1}+Q_{\text{loss}}^{-1})^{2}}\\&+2Q_{\text{leak}}^{-1}\sqrt{\frac{1}{\pi(Q_{\text{leak}}^{-1}+Q_{\text{loss}}^{-1})^{3}}+\frac{1}{\pi^{2}(Q_{\text{leak}}^{-1}+Q_{\text{loss}}^{-1})^{4}}}\end{aligned} \tag{4.8}$$

where F_{peak} is the Purcell factor at the dominating mode of the system, which indicates the highest value of Purcell factors (F) in the frequency spectrum. Equations (4.7) and (4.8) correspond to the conditions in the absence of and in the presence of dissipative losses, respectively. Equation (4.8) manifests that F_{peak} is determined by the mutual effect of Q_{leak}^{-1} and Q_{loss}^{-1} and the optimum value can be realized under the critical emission condition that reads,

$$Q_{\text{leak}}^{-1}=Q_{\text{loss}}^{-1}(1+\pi Q_{\text{loss}}^{-1}). \tag{4.9}$$

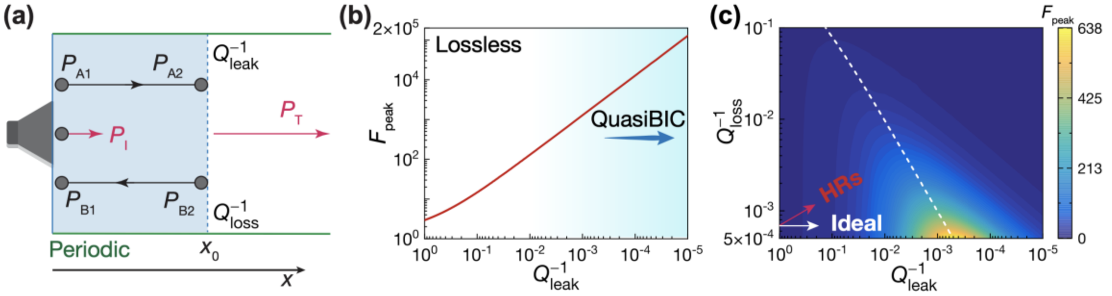

Figure 4.12 Theoretical framework of acoustic Purcell effect.

(a) Wave analysis of a resonant system theoretically treated as an effective medium and characterized by Q_{leak}^{-1} and Q_{loss}^{-1} of the dominating resonance. The sound source is at the bottom of the system. P_{I} and P_{T} represent the pressure amplitudes of waves generated by the source and emitted to the outside, respectively. P_{A1}, P_{A2}, P_{B1} and P_{B2} are the pressure amplitudes of decomposed waves at the bottom and front boundaries of the system. (b) Calculated F_{peak} with the variation of Q_{leak}^{-1} in the absence of Q_{loss}^{-1}. (c) Calculated F_{peak} as functions of Q_{leak}^{-1} and Q_{loss}^{-1}. The white dashed line indicates the critical emission condition.

The developed framework reveals important insights of the Purcell effect for an acoustic system. On the one hand, in a hypothetical lossless scenario ($Q_{\mathrm{loss}}^{-1} = 0$), F_{peak} increases with the decrease of Q_{leak}^{-1}, where an infinitely small Q_{leak}^{-1} leads to an infinite emission enhancement [Fig. 4.12(b)]. This suggests the great potential of quasiBIC systems, featured with extremely low Q_{leak}^{-1}, in stimulating strong acoustic Purcell effect. However, in practical acoustic systems with non-trivial thermal-viscous losses, the effect of Q_{loss}^{-1} becomes crucial, and optimum emission enhancement takes place under the critical emission condition (white dashed line in Fig. 4.12(c)). Evidently, to achieve a larger Purcell factor, it will be ideal that the Q_{leak}^{-1} of the system can be freely modulated to a lower value avoiding increasing the Q_{loss}^{-1}.

Nevertheless, the above requirements for strong Purcell effect are rather challenging in acoustic resonant systems due to the contradictory between low Q_{leak}^{-1} and low Q_{loss}^{-1}. For commonly-seen acoustic resonators such as Helmholtz resonators (HRs), a lower Q_{leak}^{-1} means less energy leaking from the openings, which subsequently demands narrower openings (necks) of the HRs. A narrower opening, in turn, leads to stronger thermal-viscous boundary layer effect, and brings about higher dissipative losses (larger Q_{loss}^{-1}) [19, 47], thereby preventing from realizing a large acoustic Purcell factor (exemplified by the red arrow in Fig. 4.12(c)).

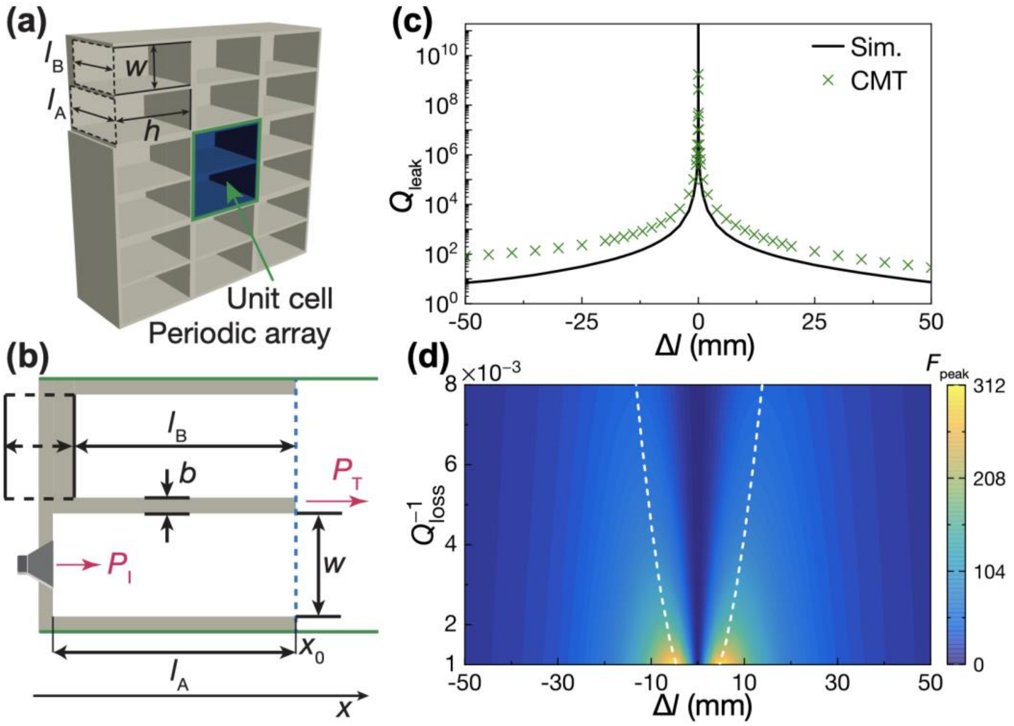

Figure 4.13 Friedrich-Wintgen quasiBIC-supporting system.

(a) Schematic of the system consisting of periodic unit cells. (b) The modulation of the unit cells with acoustic sources. The length of Cavity A (l_A) is fixed. The length of Cavity B (l_B) is tunable. (c) Calculated (CMT) and simulated Q_{leak} with the variation of Δl. The infinite Q_{leak} at $\Delta l = 0$ demonstrates the existence of a BIC. (d) F_{peak} with the modulation of Δl and the hypothetical free variation of Q_{loss}^{-1}. The analyzed system's geometric parameters are w = 46 mm, h = 100 mm, b = 8 mm and l_A = 120 mm. The white dashed line indicates the critical emission condition.

However, the contradiction can be solved by constructing a Friedrich-Wintgen quasiBIC-supporting system [Figs. 4.13(a)-(b)], which can enable the Purcell factors to theoretically reach infinite without essential restrictions. Based on the presented system, Q_{leak}^{-1} can be modulated from zero (a pure BIC) to a target value via tuning the length difference between the two cavities. As a proof-of-concept demonstration, a structure with w = 46 mm, h = 100 mm, b = 8 mm and l_A = 120 mm is presented. And with the tuning of l_B, the system is in the vicinity of a BIC when the length difference of the two cavities ($\Delta l = l_B - l_A$) approaches zero [Fig. 4.13(c)]. To examine intuitively how the

Purcell effect of the system is governed by the dissipative losses and the quasi-BIC, the structure in Fig. 4.13(c) is analyzed assuming an arbitrarily tunable Q_{loss}^{-1} . From the diagram of F_{peak} shown in Fig. 4.13(d), it is found that the presented quasiBIC-supporting system has the potential to achieve optimum F_{peak} under arbitrary Q_{loss}^{-1} via changing Δl.

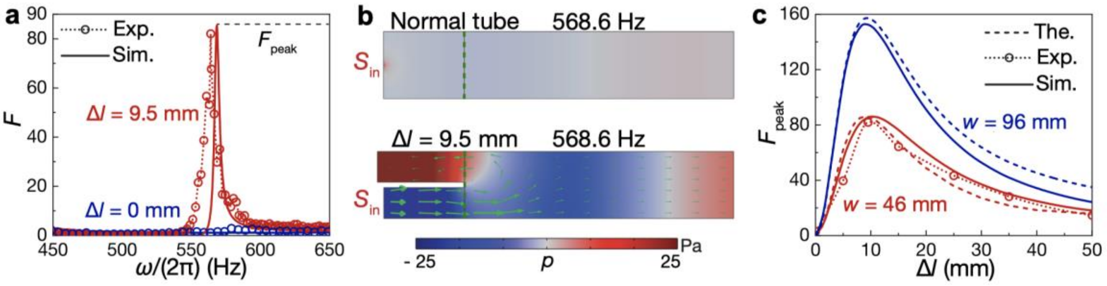

Figure 4.14 Experimental demonstration of the quasiBIC-induced acoustic Purcell effect.

(a) Measured and simulated results of acoustic Purcell factors (F) for Δl = 9.5 mm (red) and Δl = 0 mm (blue). (b) Simulated distributions of acoustic pressure (colors) and acoustic intensity (denoted by green arrows) of a normal tube and the presented two-state system. S_{in} denotes the sound source. (c) Calculated, Measured and simulated F_{peak} as a function of Δl.

To validate the theoretical analysis, experiments are performed in a steel waveguide (tube) having a length of 1460 mm and a wall thickness of 8 mm. The cross-section of the waveguide is a square with a side length of 100 mm. The unit cell of the presented structure [Fig. 4.13(b)] is produced by 3D printing. When the two cavities have the length difference of 9.5 mm (Δl = 9.5 mm, Q_{loss}^{-1} = 0.0037, Q_{leak}^{-1} = 0.0043), large emission enhancement with a Purcell factor of 82 is experimentally achieved at 564 Hz [Fig. 4.14(a)]. In addition, in the case that Δl = 0 mm, the inferior coupling condition of Q_{leak}^{-1} and Q_{loss}^{-1} suppresses the acoustic Purcell effect and the emitted waves are unable to be enhanced. To further validate the results and better illustrate the acoustic Purcell effect, simulations are conducted with COMSOL Multiphysics. The simulation results show great accordance with the experimental results, where F_{peak} reaches 84.7 at 568.6 Hz. The simulated pressure fields shown in Fig. 4.14(b) confirm that the quasi-BIC contributes to the intensive sound field inside the system and finally gives rise to the largely enhanced emitted waves. In fact, the Purcell factors of the presented quasiBIC-supporting system can be consistently enhanced by further increasing the cross-sectional area of the two cavities (smaller Q_{loss}^{-1}). For instance, when the structure size is changed to w = 96 mm and h = 200 mm, the simultaneously decreased Q_{loss}^{-1} (0.002) and Q_{leak}^{-1} (0.0022) lead to an increased F_{peak} above 150 at Δl = 9.5 mm [Fig. 4.14(c)].

To summarize, the concept of quasiBIC-induced acoustic Purcell effect is presented, which provides a feasible and efficient pathway to achieve extreme emission enhancement. The acoustic Friedrich-Wintgen quasiBIC-supporting system overcomes the contradiction that exists in conventional acoustic structures and lifts the major upper limit of acoustic Purcell effect. a theoretical framework is developed based on two fundamental factors (Q_{leak}^{-1} and Q_{loss}^{-1}), which uncovers the comprehensive physical picture of acoustic Purcell effect and reveals the critical emission condition. The good agreement between the experimental, simulation, and theoretical results proves the reliability of the framework. This work opens up avenues for the study of quasiBIC-induced acoustic Purcell effect for extreme emission enhancement, which would inspire the studies in acoustic Purcell effect and BICs, and may find applications in high-intensity and nonlinear acoustics.

5. Chapter 5: Conclusions and Future Work

5.1 Conclusions

This thesis has studied metasurface-based ultra-thin structures for tunable perfect sound absorption and high-efficiency broadband sound absorption. Furthermore, inspired by the design concepts and impedance-modulation techniques presented in constructing the metasurface-based sound absorbers, several efficient acoustic devices relevant to noise control engineering and impedance engineering are developed.

In Chapter 2, two tunable metasurface-based perfect absorbers are systematically investigated. The firstly presented spiral metasurface with an embedded neck is capable of tunable perfect absorption under a constant length of the curled channel, which shows remarkably improved adjustability of impedance modulation compared with the designs in previous studies. Then, with the aim of the further improved capability of impedance modulation and less complicated configuration of structures, the neck-embedded Helmholtz resonators (NEHRs) are presented. NEHRs can achieve largely tunable perfect absorption performance via an unchanged and deep subwavelength shape, which provides an excellent candidate for broadband sound absorbers based on coupled metasurfaces.

In Chapter 3, this thesis firstly establishes a theoretical model of the coupled acoustic components by analyzing the coherent coupling among the component resonators. Then, highly efficient and broadband sound absorbers are presented based on coupling multiple imperfect component metasurfaces. This design concept, utilizing imperfect components to construct broadband sound absorbers, exhibits significant advantages in terms of thinner structure, better absorption efficiency and broader working frequency band. Subsequently, the general acoustic responses of sound-absorbing materials are investigated, which reveals two guidelines, the over-damped condition and the reduced excessive response, for constructing highly efficient broadband sound absorbers approaching the optimal thickness restricted by the causality constraint. As a proof-of-concept design, a coupled sound-absorbing metasurface having higher degrees of freedom of impedance modulation and supporting more resonance modes is presented. This sound-absorbing metasurface realizes broadband quasi-perfect absorption from 320 to 6400 Hz (average absorption coefficient of 0.93) with a thickness of 100 mm, which successfully approaches the minimal thickness.

In Chapter 4, inspired by the design concepts and impedance-modulation techniques in Chapters 2-3, several high-performance acoustic devices are investigated, for achieving broadband sound attenuation in flow ducts, extreme asymmetric absorption in waveguides, extreme sound confinement in coupled cavities and strong emission enhancement of sound speakers. The investigations on these acoustic devices broaden the impact of the proposed sound-absorbing metasurfaces, and also pave a pathway towards the development of functional metasurface-based acoustic devices in noise-control engineering and impedance engineering.

5.2 Future work

On the basis of the above work, there are many directions for further research as follows:

(1) The acoustic impedance modulation capability of the neck-embedded Helmholtz resonator could be further enhanced by increasing the complexity of the structure to increase the number of tunable geometrical parameters that can lead to a higher degree of freedom of impedance modulation.

(2) The working frequency band of the sound-absorbing metasurfaces could be further broadened by further enhancing the modulation efficiency of the coupling effect among

components, aiming for the full frequency band in the audible range (20 Hz to 20000 Hz).

(3) The sound attenuation performance of the meta-liner has been studied at a relatively low flow speed (maximum speed of 60 m/s), and subsequent work could investigate high-performance meta-liner structures at higher flow speeds.

(4) The current study of the emission enhancement of sound sources has been carried out in a waveguide system, and subsequent work could be carried out in a free field.

(5) Based on the sound confinement phenomenon demonstrated in Section 4.3, future work could focus on how the transform the trapped sound energy into the utilizable energy.

(6) The absorption performance of the sound absorbers under severe environments could be investigated, for instance, in the environments with higher-Mach flows, higher-intensity sound and various fatigue situations.

(7) The sound absorbers' mechanical and material properties could be investigated for practical applications.

6. Appendix A: Geometric Parameters of the Investigated Samples

The specific structural parameters for the theoretically analyzed and experimentally tested samples in this thesis are listed in the following tables, where the geometrical parameters of the structures based on the optimization algorithm are given here as approximations to 0.1 mm or 0.01 mm.

Table A1 Geometrical parameters of the structures in Figs. 3.4-3.5 for the perfect components.

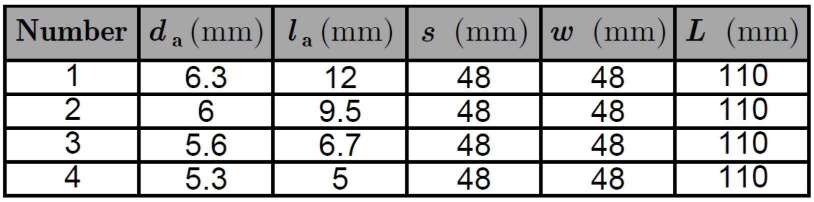

Number	d_a (mm)	l_a (mm)	s (mm)	w (mm)	L (mm)
1	6.3	12	48	48	110
2	6	9.5	48	48	110
3	5.6	6.7	48	48	110
4	5.3	5	48	48	110

Table A2 Geometrical parameters of the structures in Figs. 3.4-3.5 for the imperfect components.

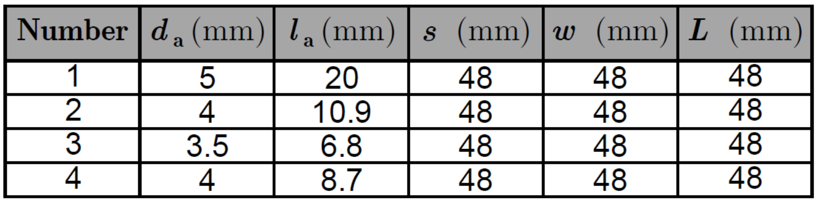

Number	d_a (mm)	l_a (mm)	s (mm)	w (mm)	L (mm)
1	5	20	48	48	48
2	4	10.9	48	48	48
3	3.5	6.8	48	48	48
4	4	8.7	48	48	48

Table A3 Geometrical parameters of the experimental structures in Fig. 3.6.

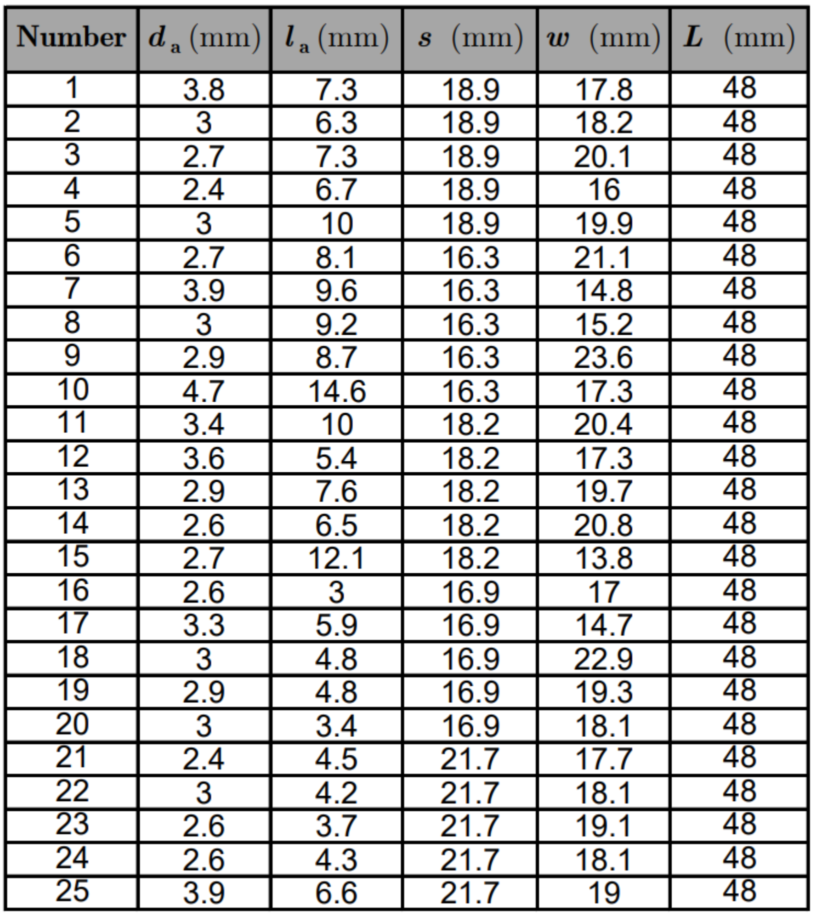

Number	d_a (mm)	l_a (mm)	s (mm)	w (mm)	L (mm)
1	3.8	7.3	18.9	17.8	48
2	3	6.3	18.9	18.2	48
3	2.7	7.3	18.9	20.1	48
4	2.4	6.7	18.9	16	48
5	3	10	18.9	19.9	48
6	2.7	8.1	16.3	21.1	48
7	3.9	9.6	16.3	14.8	48
8	3	9.2	16.3	15.2	48
9	2.9	8.7	16.3	23.6	48
10	4.7	14.6	16.3	17.3	48
11	3.4	10	18.2	20.4	48
12	3.6	5.4	18.2	17.3	48
13	2.9	7.6	18.2	19.7	48
14	2.6	6.5	18.2	20.8	48
15	2.7	12.1	18.2	13.8	48
16	2.6	3	16.9	17	48
17	3.3	5.9	16.9	14.7	48
18	3	4.8	16.9	22.9	48
19	2.9	4.8	16.9	19.3	48
20	3	3.4	16.9	18.1	48
21	2.4	4.5	21.7	17.7	48
22	3	4.2	21.7	18.1	48
23	2.6	3.7	21.7	19.1	48
24	2.6	4.3	21.7	18.1	48
25	3.9	6.6	21.7	19	48

Table A4 Geometrical parameters of the experimental structures in Fig. 3.7.

Number	d_a (mm)	l_a (mm)	s (mm)	w (mm)	L (mm)
1	2.6	2.1	4.8	4.5	18
2	2.8	10.6	4.8	5	18
3	2.1	3.1	4.8	7.1	18
4	2.8	1.3	4.8	9.3	18
5	2.2	2.5	4.8	17.3	18
6	2.4	2.7	5.1	4.1	18
7	2.6	2.5	5.1	4.5	18
8	2.5	1.7	5.1	4	18
9	3	1.3	5.1	12	18
10	2.2	1.2	5.1	18.6	18
11	2.2	2.6	15.6	4.8	18
12	2.2	1.4	15.6	4.5	18
13	2.2	2.8	15.6	5.4	18
14	2.5	1.4	15.6	11.2	18
15	2.5	1.4	15.6	17.4	18
16	3	1.3	18.6	4.2	18
17	2.7	1.3	18.6	4.2	18
18	2.3	1.6	18.6	4.2	18
19	2.6	1.5	18.6	11.4	18
20	2.6	1.2	18.6	19.3	18

Table A5 Geometrical parameters of the experimental structures in Figs. 4.2-4.3.

Number	d_a (mm)	l_a (mm)	s_{NEHR} (mm)	w_{NEHR} (mm)	l_{NEHR} (mm)
1	1.93	2.37	11.20	9.42	15.01
2	6.29	1.01	11.20	8.39	15.01
3	6.21	1.01	11.20	8.29	15.01
4	2.34	3.64	11.20	7.87	15.01
5	3.48	1.03	11.20	9.23	15.01
6	2.81	3.63	10.84	8.84	15.01
7	2.16	1.17	10.84	6.86	15.01
8	6.94	1.01	10.84	9.27	15.01
9	2.04	2.46	10.84	9.19	15.01
10	4.58	2.29	10.84	9.04	15.01
11	3.65	2.26	12.01	11.33	15.01
12	2.35	2.87	12.01	6.30	15.01
13	2.36	4.04	12.01	10.26	15.01
14	4.12	3.77	12.01	7.63	15.01
15	3.30	2.41	12.01	7.68	15.01
16	6.39	1.04	10.15	8.53	15.01
17	3.27	4.24	10.15	9.07	15.01
18	2.44	2.59	10.15	10.26	15.01
19	3.60	1.51	10.15	6.80	15.01
20	6.40	1.02	10.15	8.54	15.01

References

[1] M. Yang, P. Sheng, Sound Absorption Structures: From Porous Media to Acoustic Metamaterials, Annual Review of Materials Research, 47 (2017) 83-114.

[2] J.P. Arenas, M.J. Crocker, Recent Trends in Porous Sound-Absorbing Materials, Sound and Vibration, 44 (2010) 12-17.

[3] L. Cao, Q. Fu, Y. Si, B. Ding, J. Yu, Porous materials for sound absorption, Composites Communications, 10 (2018) 25-35.

[4] D.-Y. Maa, Potential of microperforated panel absorber, The Journal of the Acoustical Society of America, 104 (1998) 2861-2866.

[5] X. Zhang, L. Cheng, Acoustic impedance of micro-perforated panels in a grazing flow, The Journal of the Acoustical Society of America, 145 (2019) 2461.

[6] C. Wang, L. Cheng, J. Pan, G. Yu, Sound absorption of a micro-perforated panel backed by an irregular-shaped cavity, The Journal of the Acoustical Society of America, 127 (2010) 238-246.

[7] M. Toyoda, K. Sakagami, D. Takahashi, M. Morimoto, Effect of a honeycomb on the sound absorption characteristics of panel-type absorbers, Applied Acoustics, 72 (2011) 943-948.

[8] M. Toyoda, D. Takahashi, Sound transmission through a microperforated-panel structure with subdivided air cavities, The Journal of the Acoustical Society of America, 124 (2008) 3594-3603.

[9] S. Huang, S. Li, X. Wang, D. Mao, Micro-perforated absorbers with incompletely partitioned cavities, Applied Acoustics, 126 (2017) 114-119.

[10] B. Assouar, B. Liang, Y. Wu, Y. Li, J.-C. Cheng, Y. Jing, Acoustic metasurfaces, Nature Reviews Materials, 3 (2018) 460-472.

[11] S.A. Cummer, J. Christensen, A. Alù, Controlling sound with acoustic metamaterials, Nature Reviews Materials, 1 (2016).

[12] J. Zhu, J. Christensen, J. Jung, L. Martin-Moreno, X. Yin, L. Fok, X. Zhang, F.J. Garcia-Vidal, A holey-structured metamaterial for acoustic deep-subwavelength imaging, Nature Physics, 7 (2010) 52-55.

[13] S.W. Fan, S.D. Zhao, A.L. Chen, Y.F. Wang, B. Assouar, Y.S. Wang, Tunable Broadband Reflective Acoustic Metasurface, Physical Review Applied, 11 (2019).

[14] Z. Liang, J. Li, Extreme acoustic metamaterial by coiling up space, Physical Review Letters, 108 (2012) 114301.

[15] Y. Xie, W. Wang, H. Chen, A. Konneker, B.I. Popa, S.A. Cummer, Wavefront modulation and subwavelength diffractive acoustics with an acoustic metasurface, Nature Communications, 5 (2014) 5553.

[16] N. Kaina, F. Lemoult, M. Fink, G. Lerosey, Negative refractive index and acoustic superlens from multiple scattering in single negative metamaterials, Nature, 525 (2015) 77.

[17] Y. Li, B. Liang, Z.M. Gu, X.Y. Zou, J.C. Cheng, Reflected wavefront manipulation based on ultrathin planar acoustic metasurfaces, Scientific Reports, 3 (2013) 2546.

[18] Y. Li, X. Jiang, B. Liang, J.-c. Cheng, L. Zhang, Metascreen-Based Acoustic Passive Phased Array, Physical Review Applied, 4 (2015).

[19] B. Liang, B. Yuan, J.C. Cheng, Acoustic diode: rectification of acoustic energy flux in one-dimensional systems, Physical Review Letters, 103 (2009) 104301.

[20] B.I. Popa, S.A. Cummer, Non-reciprocal and highly nonlinear active acoustic metamaterials, Nature Communications, 5 (2014) 3398.

[21] Y. Li, C. Shen, Y. Xie, J. Li, W. Wang, S.A. Cummer, Y. Jing, Tunable Asymmetric Transmission via Lossy Acoustic Metasurfaces, Physical Review Letters, 119 (2017) 035501.
[22] H. Long, Y. Cheng, X. Liu, Asymmetric absorber with multiband and broadband for low-frequency sound, Applied Physics Letters, 111 (2017).
[23] W.-K. Cao, L.-T. Wu, C. Zhang, J.-C. Ke, Q. Cheng, T.-J. Cui, Y. Jing, Asymmetric transmission of acoustic waves in a waveguide via gradient index metamaterials, Science Bulletin, 64 (2019) 808-813.
[24] X. Wang, X. Fang, D. Mao, Y. Jing, Y. Li, Extremely Asymmetrical Acoustic Metasurface Mirror at the Exceptional Point, Physical Review Letters, 123 (2019) 214302.
[25] S. Huang, Z. Zhou, D. Li, T. Liu, X. Wang, J. Zhu, Y. Li, Compact broadband acoustic sink with coherently coupled weak resonances, Science Bulletin, 65 (2020) 373-379.
[26] J. Mei, G. Ma, M. Yang, Z. Yang, W. Wen, P. Sheng, Dark acoustic metamaterials as super absorbers for low-frequency sound, Nature Communications, 3 (2012) 756.
[27] G. Ma, M. Yang, S. Xiao, Z. Yang, P. Sheng, Acoustic metasurface with hybrid resonances, Nature Materials, 13 (2014) 873-878.
[28] Y. Li, B.M. Assouar, Acoustic metasurface-based perfect absorber with deep subwavelength thickness, Applied Physics Letters, 108 (2016).
[29] X. Cai, Q. Guo, G. Hu, J. Yang, Ultrathin low-frequency sound absorbing panels based on coplanar spiral tubes or coplanar Helmholtz resonators, Applied Physics Letters, 105 (2014).
[30] C. Zhang, X. Hu, Three-Dimensional Single-Port Labyrinthine Acoustic Metamaterial: Perfect Absorption with Large Bandwidth and Tunability, Physical Review Applied, 6 (2016).
[31] Y. Xie, B.I. Popa, L. Zigoneanu, S.A. Cummer, Measurement of a broadband negative index with space-coiling acoustic metamaterials, Physical Review Letters, 110 (2013) 175501.
[32] T. Frenzel, J. David Brehm, T. Bückmann, R. Schittny, M. Kadic, M. Wegener, Three-dimensional labyrinthine acoustic metamaterials, Applied Physics Letters, 103 (2013).
[33] L. Liu, H. Chang, C. Zhang, X. Hu, Single-channel labyrinthine metasurfaces as perfect sound absorbers with tunable bandwidth, Applied Physics Letters, 111 (2017).
[34] D.T. Li, S.B. Huang, F.S. Mo, X. Wang, Y. Li, Low-frequency broadband absorbers based on coupling micro-perforated panel and space-curling chamber, Chinese Science Bulletin-Chinese, 65 (2020) 1420-1427.
[35] S.H. Xie, X.S. Fang, P.Q. Li, S.B. Huang, Y.G. Peng, Y.X. Shen, Y. Li, X.F. Zhu, Tunable Double-Band Perfect Absorbers via Acoustic Metasurfaces with Nesting Helical Tracks*, Chinese Physics Letters, 37 (2020).
[36] M.R. Stinson, The propagation of plane sound waves in narrow and wide circular tubes, and generalization to uniform tubes of arbitrary cross-sectional shape, The Journal of the Acoustical Society of America, 89 (1991) 550-558.
[37] H. Tijdeman, On the propagation of sound waves in cylindrical tubes, Journal of Sound and Vibration, 39 (1975) 1-33.
[38] S. Huang, X. Fang, X. Wang, B. Assouar, Q. Cheng, Y. Li, Acoustic perfect absorbers via spiral metasurfaces with embedded apertures, Applied Physics Letters, 113 (2018).
[39] M.R. Stinson, E.A.G. Shaw, Acoustic impedance of small, circular orifices in thin plates, The Journal of the Acoustical Society of America, 77 (1985) 2039-2042.

[40] S. Huang, X. Fang, X. Wang, B. Assouar, Q. Cheng, Y. Li, Acoustic perfect absorbers via Helmholtz resonators with embedded apertures, The Journal of the Acoustical Society of America, 145 (2019) 254.
[41] U. Ingard, On the Theory and Design of Acoustic Resonators, The Journal of the Acoustical Society of America, 25 (1953) 1037-1061.
[42] K. Donda, Y. Zhu, S.-W. Fan, L. Cao, Y. Li, B. Assouar, Extreme low-frequency ultrathin acoustic absorbing metasurface, Applied Physics Letters, 115 (2019).
[43] C.Z. Cai, C.M. Mak, X.F. Shi, An extended neck versus a spiral neck of the Helmholtz resonator, Applied Acoustics, 115 (2017) 74-80.
[44] A. Selamet, Z.L. Ji, Acoustic Attenuation Performance of Circular Expansion Chambers with Extended Inlet/Outlet, Journal of Sound and Vibration, 223 (1999) 197-212.
[45] T. Yasuda, C. Wu, N. Nakagawa, K. Nagamura, Studies on an automobile muffler with the acoustic characteristic of low-pass filter and Helmholtz resonator, Applied Acoustics, 74 (2013) 49-57.
[46] Z.X. Kang, Z.L. Ji, Acoustic length correction of duct extension into a cylindrical chamber, Journal of Sound and Vibration, 310 (2008) 782-791.
[47] A. Selamet, I. Lee, Helmholtz resonator with extended neck, The Journal of the Acoustical Society of America, 113 (2003) 1975-1985.
[48] D. Li, D. Chang, B. Liu, Enhancing the low frequency sound absorption of a perforated panel by parallel-arranged extended tubes, Applied Acoustics, 102 (2016) 126-132.
[49] F. Simon, Long Elastic Open Neck Acoustic Resonator for low frequency absorption, Journal of Sound and Vibration, 421 (2018) 1-16.
[50] J.W. Guo, X. Zhang, Y. Fang, R. Fattah, Manipulating reflected acoustic wave via Helmholtz resonators with varying-length extended necks, Journal of Applied Physics, 124 (2018).
[51] D. Kong, S. Huang, D. Li, C. Cai, Z. Zhou, B. Liu, G. Cao, X. Chen, Y. Li, S. Liu, Low-frequency multi-order acoustic absorber based on spiral metasurface, The Journal of the Acoustical Society of America, 150 (2021) 12.
[52] S. Huang, E. Zhou, Z. Huang, P. Lei, Z. Zhou, Y. Li, Broadband sound attenuation by metaliner under grazing flow, Applied Physics Letters, 118 (2021).
[53] Z. Zhou, S. Huang, D. Li, J. Zhu, Y. Li, Broadband impedance modulation via non-local acoustic metamaterials, National Science Review, DOI 10.1093/nsr/nwab171(2021).
[54] J. Guo, T. Zhou, Y. Fang, X. Zhang, Experimental study on a compact lined circular duct for small-scale propeller noise reduction, Applied Acoustics, 179 (2021).
[55] J.W. Guo, X. Zhang, Y. Fang, Z.Y. Jiang, Wideband low-frequency sound absorption by inhomogeneous multi-layer resonators with extended necks, Composite Structures, 260 (2021).
[56] M. Yang, S. Chen, C. Fu, P. Sheng, Optimal sound-absorbing structures, Materials Horizons, 4 (2017) 673-680.
[57] H.T. Chang, L. Liu, C. Zhang, X.H. Hu, Broadband high sound absorption from labyrinthine metasurfaces, Aip Advances, 8 (2018).
[58] T. Wu, T.J. Cox, Y.W. Lam, A profiled structure with improved low frequency absorption, Journal of the Acoustical Society of America, 110 (2001) 3064-3070.
[59] T. Wu, T.J. Cox, Y.W. Lam, From a profiled diffuser to an optimized absorber, The Journal of the Acoustical Society of America, 108 (2000) 643-650.

[60] N. Jimenez, V. Romero-Garcia, V. Pagneux, J.P. Groby, Rainbow-trapping absorbers: Broadband, perfect and asymmetric sound absorption by subwavelength panels for transmission problems, Scientific Reports, 7 (2017) 13595.
[61] Y. Wang, H.G. Zhao, H.B. Yang, J. Zhong, D. Zhao, Z.L. Lu, J.H. Wen, A tunable sound-absorbing metamaterial based on coiled-up space, Journal of Applied Physics, 123 (2018).
[62] X. Peng, J. Ji, Y. Jing, Composite honeycomb metasurface panel for broadband sound absorption, The Journal of the Acoustical Society of America, 144 (2018) EL255.
[63] C.R. Liu, J.H. Wu, F.Y. Ma, X. Chen, Z.R. Yang, A thin multi-order Helmholtz metamaterial with perfect broadband acoustic absorption, Applied Physics Express, 12 (2019).
[64] H. Long, C. Shao, C. Liu, Y. Cheng, X. Liu, Broadband near-perfect absorption of low-frequency sound by subwavelength metasurface, Applied Physics Letters, 115 (2019).
[65] T. Wu, T.J. Cox, Y.W. Lam, From a profiled diffuser to an optimized absorber, J Acoust Soc Am, 108 (2000) 643-650.
[66] H. Long, Y. Cheng, J. Tao, X. Liu, Perfect absorption of low-frequency sound waves by critically coupled subwavelength resonant system, Applied Physics Letters, 110 (2017).
[67] V. Romero-Garcia, G. Theocharis, O. Richoux, V. Pagneux, Use of complex frequency plane to design broadband and sub-wavelength absorbers, The Journal of the Acoustical Society of America, 139 (2016) 3395.
[68] X. Ma, Z. Su, Development of acoustic liner in aero engine: a review, Science China Technological Sciences, 63 (2020) 2491-2504.
[69] H. Jiang, X. Huang, Efficient Impedance Eductions for Liner Tests in Grazing Flow Incidence Tube, Journal of Vibration and Acoustics, 139 (2017).
[70] C. Lahiri, F. Bake, A review of bias flow liners for acoustic damping in gas turbine combustors, Journal of Sound and Vibration, 400 (2017) 564-605.
[71] X. Qiu, B. Xin, L. Wu, Y. Meng, X. Jing, Investigation of straightforward impedance eduction method on single-degree-of-freedom acoustic liners, Chinese Journal of Aeronautics, 31 (2018) 2221-2233.
[72] R. Troian, D. Dragna, C. Bailly, M.-A. Galland, Broadband liner impedance eduction for multimodal acoustic propagation in the presence of a mean flow, Journal of Sound and Vibration, 392 (2017) 200-216.
[73] A.W. Guess, Calculation of perforated plate liner parameters from specified acoustic resistance and reactance, Journal of Sound and Vibration, 40 (1975) 119-137.
[74] W. Zhu, X. Fang, D. Li, Y. Sun, Y. Li, Y. Jing, H. Chen, Simultaneous Observation of a Topological Edge State and Exceptional Point in an Open and Non-Hermitian Acoustic System, Physical Review Letters, 121 (2018) 124501.
[75] C. Fu, X. Zhang, M. Yang, S. Xiao, Z. Yang, Hybrid membrane resonators for multiple frequency asymmetric absorption and reflection in large waveguide, Applied Physics Letters, 110 (2017).
[76] H. Long, Y. Cheng, X. Liu, Reconfigurable sound anomalous absorptions in transparent waveguide with modularized multi-order Helmholtz resonator, Scientific Reports, 8 (2018) 15678.
[77] M.A. Miri, A. Alu, Exceptional points in optics and photonics, Science, 363 (2019).
[78] H.Z. Chen, T. Liu, H.Y. Luan, R.J. Liu, X.Y. Wang, X.F. Zhu, Y.B. Li, Z.M. Gu, S.J. Liang, H. Gao, L. Lu, L. Ge, S. Zhang, J. Zhu, R.M. Ma, Revealing the missing dimension at an exceptional point, Nature Physics, 16 (2020) 571-+.

[79] B. Peng, Ş.K. Özdemir, F. Lei, F. Monifi, M. Gianfreda, G.L. Long, S. Fan, F. Nori, C.M. Bender, L. Yang, Parity–time-symmetric whispering-gallery microcavities, Nature Physics, 10 (2014) 394-398.
[80] H. Hodaei, M.A. Miri, M. Heinrich, D.N. Christodoulides, M. Khajavikhan, Parity-time-symmetric microring lasers, Science, 346 (2014) 975-978.
[81] R. El-Ganainy, K.G. Makris, M. Khajavikhan, Z.H. Musslimani, S. Rotter, D.N. Christodoulides, Non-Hermitian physics and PT symmetry, Nature Physics, 14 (2018) 11-19.
[82] D. Li, S. Huang, Y. Cheng, Y. Li, Compact asymmetric sound absorber at the exceptional point, Science China Physics, Mechanics & Astronomy, 64 (2021) 244303.
[83] X. Zhu, H. Ramezani, C. Shi, J. Zhu, X. Zhang, PT-Symmetric Acoustics, Physical Review X, 4 (2014).
[84] B.H. Song, J.S. Bolton, A transfer-matrix approach for estimating the characteristic impedance and wave numbers of limp and rigid porous materials, The Journal of the Acoustical Society of America, 107 (2000) 1131-1152.
[85] S. Huang, T. Liu, Z. Zhou, X. Wang, J. Zhu, Y. Li, Extreme Sound Confinement From Quasibound States in the Continuum, Physical Review Applied, 14 (2020).
[86] C.W. Hsu, B. Zhen, A.D. Stone, J.D. Joannopoulos, M. Soljačić, Bound states in the continuum, Nature Reviews Materials, 1 (2016).
[87] A.F. Sadreev, Interference traps waves in an open system: bound states in the continuum, Reports on Progress in Physics, 84 (2021).
[88] P. Vincent, M. Nevière, Corrugated dielectric waveguides: A numerical study of the second-order stop bands, Applied Physics, 20 (1979) 345-351.
[89] H. Friedrich, D. Wintgen, Interfering resonances and bound states in the continuum, Physical Review A, 32 (1985) 3231-3242.
[90] A. Kodigala, T. Lepetit, Q. Gu, B. Bahari, Y. Fainman, B. Kante, Lasing action from photonic bound states in continuum, Nature, 541 (2017) 196-199.
[91] C. Huang, C. Zhang, S. Xiao, Y. Wang, Y. Fan, Y. Liu, N. Zhang, G. Qu, H. Ji, J. Han, L. Ge, Y. Kivshar, Q. Song, Ultrafast control of vortex microlasers, Science, 367 (2020) 1018-1021.
[92] R. Parker, Resonance effects in wake shedding from parallel plates: Some experimental observations, Journal of Sound and Vibration, 4 (1966) 62-72.
[93] R. Parker, W.M. Griffiths, Low frequency resonance effects in wake shedding from parallel plates, Journal of Sound and Vibration, 7 (1968) 371-379.
[94] R. Parker, Resonance effects in wake shedding from parallel plates: Calculation of resonant frequencies, Journal of Sound and Vibration, 5 (1967) 330-343.
[95] D.V. Evans, C.M. Linton, F. Ursell, Trapped Mode Frequencies Embedded in the Continuous Spectrum, The Quarterly Journal of Mechanics and Applied Mathematics, 46 (1993) 253-274.
[96] E. Davies, Trapped modes in acoustic waveguides, The Quarterly Journal of Mechanics and Applied Mathematics, 51 (1998) 477-492.
[97] S. Hein, W. Koch, L. Nannen, Trapped modes and Fano resonances in two-dimensional acoustical duct–cavity systems, Journal of Fluid Mechanics, 692 (2012) 257-287.
[98] C.M. Linton, M. McIver, P. McIver, K. Ratcliffe, J. Zhang, Trapped modes for off-centre structures in guides, Wave Motion, 36 (2002) 67-85.
[99] L. Huang, Y.K. Chiang, S. Huang, C. Shen, F. Deng, Y. Cheng, B. Jia, Y. Li, D.A. Powell, A.E. Miroshnichenko, Sound trapping in an open resonator, Nature Communications, 12 (2021) 4819.

[100] L. Cao, Y. Zhu, S. Wan, Y. Zeng, Y. Li, B. Assouar, Perfect absorption of flexural waves induced by bound state in the continuum, Extreme Mechanics Letters, 47 (2021).
[101] S. Fan, W. Suh, J.D. Joannopoulos, Temporal coupled-mode theory for the Fano resonance in optical resonators, Journal of the Optical Society of America A, 20 (2003) 569-572.
[102] W. Tan, Y. Sun, Z.-G. Wang, H. Chen, Manipulating electromagnetic responses of metal wires at the deep subwavelength scale via both near- and far-field couplings, Applied Physics Letters, 104 (2014).
[103] K.Y. Bliokh, Y.P. Bliokh, V. Freilikher, S. Savel'ev, F. Nori, Colloquium: Unusual resonators: Plasmonics, metamaterials, and random media, Reviews of Modern Physics, 80 (2008) 1201-1213.
[104] E.M. Purcell, H.C. Torrey, R.V. Pound, Resonance Absorption by Nuclear Magnetic Moments in a Solid, Physical Review, 69 (1946) 37-38.
[105] C. Sauvan, J.P. Hugonin, I.S. Maksymov, P. Lalanne, Theory of the spontaneous optical emission of nanosize photonic and plasmon resonators, Physical Review Letters, 110 (2013) 237401.
[106] A.L. Holsteen, S. Raza, P. Fan, P.G. Kik, M.L. Brongersma, Purcell effect for active tuning of light scattering from semiconductor optical antennas, Science, 358 (2017) 1407-1410.
[107] J. Gallego, W. Alt, T. Macha, M. Martinez-Dorantes, D. Pandey, D. Meschede, Strong Purcell Effect on a Neutral Atom Trapped in an Open Fiber Cavity, Physical Review Letters, 121 (2018) 173603.
[108] E. Yablonovitch, Inhibited spontaneous emission in solid-state physics and electronics, Physical Review Letters, 58 (1987) 2059-2062.
[109] J. Gérard, B. Sermage, B. Gayral, B. Legrand, E. Costard, V. Thierry-Mieg, Enhanced Spontaneous Emission by Quantum Boxes in a Monolithic Optical Microcavity, Physical Review Letters, 81 (1998) 1110-1113.
[110] H.N. Krishnamoorthy, Z. Jacob, E. Narimanov, I. Kretzschmar, V.M. Menon, Topological transitions in metamaterials, Science, 336 (2012) 205-209.
[111] M. Landi, J. Zhao, W.E. Prather, Y. Wu, L. Zhang, Acoustic Purcell Effect for Enhanced Emission, Physical Review Letters, 120 (2018) 114301.
[112] Y. Song, J. Du, N. Jiang, X. Zhao, X. Sun, Y. Cui, X. Hu, Strong Collimated Emission Enhancement by Acoustic Metasurfaces, Physical Review Applied, 12 (2019).